BREAST CANCER IMAGING BY MICROWAVE TOMOGRAPHY

THESIS

BREAST CANCER IMAGING BY MICROWAVE TOMOGRAPHY

LATIFAH BINTI MOHAMED

Graduate School of

Science and Technology, Educational Division

Department of Information Science and Technology

Shizuoka University

June 2016

TABLE OF CONTENT

LIST OF FIGURES

LIST OF TABLES

ACKNOWLEDGEMENTS

I am grateful for the guidance and continuous support from my supervisor, Professor Yoshihiko Kuwahara. His inspiring advice and commitment during the period of this work are invaluable. He has been supported me by providing a research assistantship almost over three years through the rough road to finish this research.

I owe sincere and earnest thankfulness to the Mammography teammates, Mr. Ozawa Naoyuki, Mr. Ono Yuki and Mr. Kamiya Toshihiro for their support, advice and multiple opportunities to show and discuss my research results.

I sincerely thank all my laboratory members belong to Kuwalab, Shizuoka University, for their kindness, respect, selfless help and support both academically and personally since the day I joined the laboratory.

My thanks go to all my friends who have shared with me these past years enriching my professional and private life by their support, collaboration, encouragement, and friendship.

Last but not least, I would like to express my deepest gratitude to my family especially my parents and my siblings without whom all this would not happen at all.

ABSTRACT

Breast cancer is one of the most widespread types of cancer in the world. The key factor in treatment is to reliably diagnose the cancer in the early stages. Moreover, currently used clinical diagnostic modalities, such as X-ray mammography, MRI, and ultra-sound are limited by cost and reliability issues. These limitations have motivated researchers to develop a more effective, low-cost diagnostic method and involving lower ionization for cancer detection. Recently, studies on the early detection of breast cancer by microwave imaging have attracted significant interest among researchers over the last decade, due to the high dielectric properties contrast between the cancerous and the normal tissue. In this thesis, tomography based microwave imaging is proposed as a method for early breast cancer detection. This imaging system has advantages such as low cost, being non-invasive and easy to use, with quantitative images which provides information directly correlated to the composition of the examined object, thus has a good potential in early cancer detection.

Microwave tomography is an inverse scattering problem which is formalized by determine the position and complex permittivity distribution of the unknown object from the measured scattered field. The image reconstruction process in microwave tomography involves forward problem and inverse problem. For the forward problem, Method of Moment (MoM) is used to obtain the measurement scattering data. For the inverse problem, two approaches were proposed to solve the non-linear inverse scattering method, i.e., Newton-Kantorovich and Distorted Born Iterative Method (DBIM). In addition, three types of solving techniques to reduce the ill-posedness and perform more stable solution were also introduced. The ill-posed of non-linear problem can be avoided by choosing appropriate solving techniques, considerable number of unknowns used in the analysis region, and the use of a *priori* information.

In microwave tomography, it is necessary to increase the amount of diverse observation data to obtain accurate image reconstruction of the complex permittivity distribution of the imaging area. Several methods were considered, such as increase the number of antennas, use multi-frequency method and implement the multi-polarization method. In this thesis, the multi-polarization approach has been proposed as a suitable technique for the acquisition of a variety of observation data. A compact-sized imaging sensor using multi-polarization approach for accurate image reconstruction is presented. While the effectiveness of employing multi-polarization has been confirmed, the physical considerations related to image reconstruction have not been investigated. An analysis of the correlation coefficient of the received data of adjacent antennas was performed to interpret the imaging results. Numerical simulation results demonstrated that multi-polarization can reconstruct images better compared to single polarizations owing to its low correlation coefficient. For this reason, the correlation coefficient may represent a viable parameter for image reconstruction in microwave tomography aimed at breast cancer detection.

CHAPTER 1

INTRODUCTION

1.1 Research Background

According to the World Health Organization (WHO), breast cancer is the most common cancer among women worldwide with over 1 million cases [1]. In Japan, the breast cancer incidence and associated mortality rates of women are lower compared to Western countries. However, it is one of the leading causes of cancer deaths among women, and the incidence rate has increased since 1975, regardless of age group [2][3].

Figure 1.1 shows the trends in age-adjusted incidence rate of breast cancer in Japan for year 1985 – 2010. The incidence rate of breast cancer is observed to increase gradually towards year. It has been reported that the projection of breast cancer incidence in year 2015 accounts for 21.2% of all new cancers in Japan with an age-standardized rate of 89.4 per 100 000 women [3]. Therefore, an early detection of breast cancer is important because it helps decrease the mortality

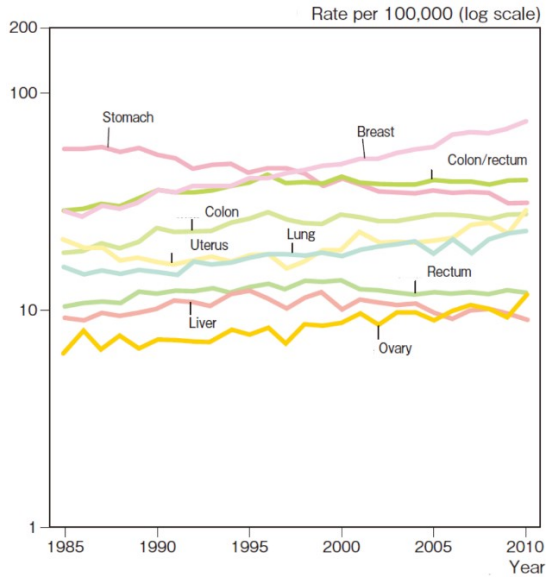

Figure 1.1 Trends in age-adjusted incidence rate of breast cancer [3]

rate of breast cancer. Meanwhile, Figure 1.2 shows the trends in age-specific incidence rate for breast cancer between year 1980 and 2011. There is a rapid increase in incidence rate among middle and old age groups, especially 45 – 64 years old. In 2011, a clear peak was observed in this age group. Correspondingly, the Japan national breast screening program was launched in 2000 pursuant to the Ministry of Health, Labor and Welfare of Japan (MHLW) notification (Notification Roken No 65). Another notification (Notification Rorohatsu No. 0427001) was introduced for Japanese women aged 40–49 years to undergo breast cancer screening from 2004 [4].

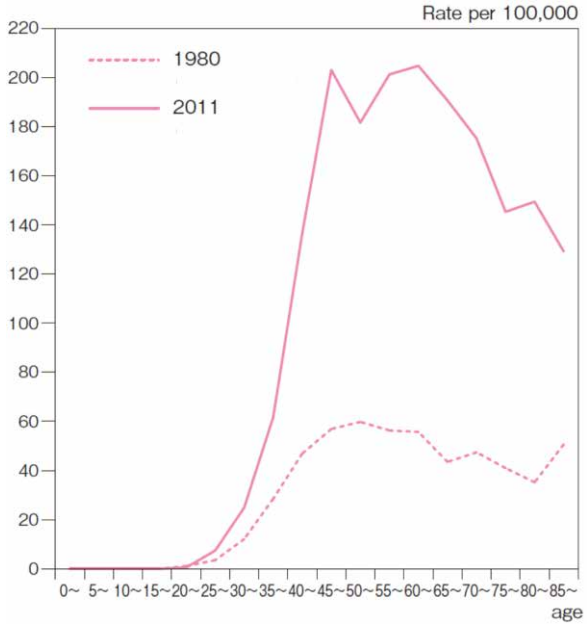

Figure 1.2 Trends in age-specific incidence rate of breast cancer (1980, 2010) [3]

The most widely used breast cancer screening are Clinical Breast Examination (CBE), X-ray Mammography, Magnetic Resonance Imaging (MRI) and Ultra-sound Imaging. Today, in most developed countries, mammography is widely used and in general an accepted method for breast cancer screening. However, mammography modalities suffer from several limitations, such as ionizing X-rays, and painful breast compression. It also reported that mammography provides false rate in detection, especially for younger women due to dense breast [4]. The burden of breast

cancer for Japanese women aged 40 – 49 years cannot be ignored despite the absence of studies evaluating mortality reduction using mammography, particularly from the perspective of the balance of benefits and harms [5].

A non-ionizing imaging methods exists today are MRI and Ultrasound Imaging. MRI has been shown to have a high sensitivity, but its high cost and the time consuming diagnosis are major shortcomings. Whereas the diagnosis of cancer using ultrasound is dependent on the skills of physician, although it is a cheaper way. Moreover, these techniques are used as a complementary for mammography to verify the malignant tissues, thus not suitable for large screening programs. From this discussion, it is clearly that there is a high need of alternative imaging modalities in order to decrease the global mortality related to breast cancers.

Recently, studies on the early detection of breast cancer by microwave imaging (MWI) have attracted considerable interest among researchers [6]. This imaging system has advantages such as low cost, being non- invasive and easy-use, provides high image resolution and thus with potential for early cancer detection.

Microwaves and millimeter waves have been used extensively to image dielectric bodies. The relatively long wavelengths (from a millimeter to a meter) allow for penetration into many optically opaque mediums such as living tissues, wood, plastics, concrete, soil, etc [6]. When the human body or a biological system is illuminated by an electromagnetic wave, an electromagnetic field is induced inside the body and an electromagnetic wave is scattered externally by the body. Since the human body or a biological system is an irregularly shaped heterogeneous conducting medium with frequency-dependent permittivity and conductivity, the distribution of the internal electromagnetic field and the scattered electromagnetic wave will depend on the body's physiological parameters and geometry, as well as the frequency and polarization of the incident wave [7].

A clinical study on behavior of electromagnetic field using normal breast were done by researchers from Dartmouth College, Hanover USA. These results illustrate that clinical microwave tomographic imaging of the breast is feasible and that the images appear to produce clinically relevant information on breast tissue composition [8]. Furthermore, researchers from University of Wisconsin proved that microwave imaging has a strong potential to detect cancer, due to the high dielectric contrast is observed between malignant breast tumor tissues and fibrous and glandular breast tissues [9][10]. These findings are very interesting knowledge as a platform to establish new imaging modalities using microwaves applied toward breast cancer detection.

1.2 Problem Statement

The application of microwaves in biomedical imaging and diagnostics, however, remains a field with many uncharted territories. The motivation for major screening programs is the strong correlation between the outcome of a breast cancer and its size at the time of detection. The two major approaches of microwave imaging today are tomographic methods, where cross-sectional slices of the dielectric properties is generated. Whereas the second approach is radar-based imaging where strong scatterers is found inside an object. The radar approach is not issued in this thesis, but a recent view of the techniques is published by Hagness et. al [10][11][12] and Kuwahara et. al. [13]–[18].

They have verified their radar approach in an experimental setup using an ultra-wideband antenna with impressive results. However, the screening method using ultra-wideband (UWB) radar require further improvements. Furthermore, in a realistic situation it will be very hard to diagnostic a cancer because the method just obtains qualitative images. A quantitative method must be used for a cancer detection. The difference between a qualitative and a quantitative image is that the quantitative image gives information directly correlated to the dielectric properties.

The microwave tomography (MWT) is proposed as an alternative imaging to UWB radar. Microwave tomography is based on the non-linear inverse scattering problem. As an example of inverse problem, let G and F be Hilbert spaces, and L is a continuous linear operator between them. Let $g \in G$ and $f \in F$, where $g = Lf$. The forward problem is to compute g with given f. Whereas the inverse problem is to compute f with given g. Figure 1.3 illustrates the microwave inverse scattering problem. The object with unknown dielectric properties is surrounded by an array of antenna. The objective of microwave inverse scattering problem is to determine for the unknown dielectric profile of the object based on the measured return signals from the antennas.

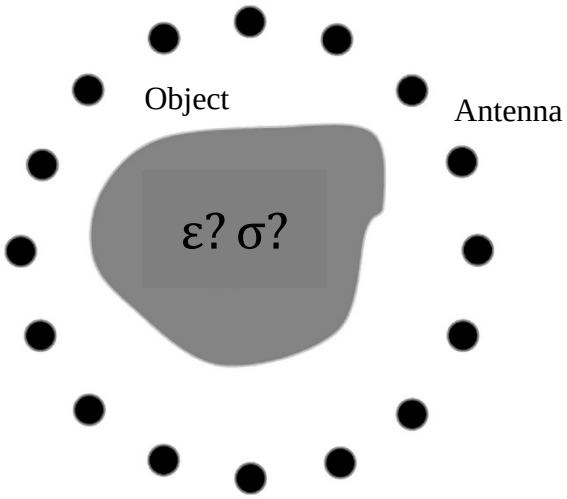

Figure 1.3 The microwave inverse scattering problem [19]

The image reconstruction in microwave tomography is an example of an inverse scattering problem that is typically ill-posed and nonlinear. This can dramatically degrade the accuracy of a computation and the final results. In order to achieve accurate image reconstruction, it is necessary to obtain diverse measurements data. Several methods must be considered, such as increase the number of antennas, use multi-frequency method and implement the multi-

polarization method. The image reconstruction algorithm is then developed to determine the dielectric profile of unknown object. The electrical properties of the various tissues in the human body vary widely, thus strongly heterogeneous. The tissue heterogeneity is one of the problems for the algorithms, but is not issued in this thesis.

1.3 Objective of Study

In this thesis, tomography-based microwave imaging is proposed as an early breast cancer detection method. In order to achieve this, the main objectives in this thesis are as follows:

1. To study nonlinear inverse scattering problems,
2. To develop a reconstruction algorithm to solve the nonlinear inverse scattering problems,
3. To design a compact-sized antenna array configurations for the microwave imaging system,
4. To model an imaging object that mimicking human breast tissue for breast cancer detection,
5. To investigate the impact of polarizations for accurate image reconstructions,
6. To investigate the correlation of coefficient of adjacent antennas as a viable parameter in design considerations.

1.4 Novelty

The novel aspects of the present work are as follows:

1. Tomography-based microwave imaging has the potential to detect breast cancer because it provides quantitative results, which is directly correlate to the location and dielectric properties of imaged objects.

2. Microwave tomography is an example of nonlinear inverse scattering problem, which is typically ill-posedness. This can be reduced by including a *priori* information, appropriate regularization parameter, and considerable number of unknowns used in the analysis region. The suitable implementation of inverse problem approach is also the key factor in inverse scattering problem.

3. The multi-polarization method has been proposed as a suitable technique for the acquisition of a variety of observation data. A compact-sized imaging sensor utilizing multi-polarization approach in microwave tomography imaging is presented for breast cancer detection.

4. While the effectiveness of employing multi-polarization to reconstruct images has been confirmed, the physical considerations related to image reconstruction have not been investigated. An analysis of the correlation coefficient of the received data of adjacent antennas was performed to interpret the imaging results. The correlation of coefficient of adjacent antennas may represent a viable design parameter for image reconstruction in microwave tomography.

1.5 Thesis Outline

This thesis consists of 6 chapters stated as follows:

In Chapter 2, a brief overview of issues related to breast cancer is presented. These include the physiology of the cancerous breast, currently available breast cancer screening modalities, and microwave imaging for breast cancer detection.

In Chapter 3, microwave tomography for early detection is introduced. The principles and important parameters in forward problem and nonlinear inverse scattering problems is discussed. The challenges in microwave tomography are also outlined.

In Chapter 4, the microwave tomography system is explained. Two antenna array configurations, with a single polarization and multi-polarization is introduced. A hemisphere breast models that mimicking human breast tissue are also proposed.

In Chapter 5, the results of numerical simulations are presented. These results are divided according to corresponding inverse problem approach and configuration model from Chapter 4.

In Chapter 6, the conclusions of the study and suggestions for future work are discussed.

CHAPTER 2

LITERATURE REVIEW

2.1 Overview

This chapter discusses the background of breast cancer in regard to the physiology of breast, and current breast cancer detection modalities. This chapter provides essential and important background information for the following chapters. Furthermore, the final section focuses on the introduction of microwave imaging for breast cancer detection.

2.2 Physiology of Breast

2.2.1 Anatomy

The anatomy of the normal breast and its surrounding tissues are illustrated in Figure 2.1 [20]. In general, the breast lies over a pectoral muscle and composed of skin, adipose (fat), connective tissue and glandular tissue. The proportions of fat, connective and glandular tissue vary between people, age and according to physiological periods such as menstrual cycle and pregnancy.

A tumor or neoplasm is formed by a lump of tissue which is composed of abnormally growing cells called cancerous cells. The cancerous cell continues to grow and divide without restraint, eventually spreading throughout the body, and progressively leading to death. Tumors can be mainly classified as benign and malignant. A benign tumor grows with a controllable speed, and remains localized to its original location. Therefore it neither invades surrounding normal tissue nor spreads to other body sites. In contrast, a malignant tumor invades and destroys healthy cells and may grow at a high rate or spread to other adjacent tissues and organs. Only malignant tumors are properly considered cancers [21].

Breast cancer refers to a malignant tumor that has developed from cells in the breast. It is

a common cancer in women which usually originates from the lobules or ducts, and can spread through the lymph system [22]. Age, genetics, family history or environmental effects are the risk factors of breast cancer. Commonly, the surrounding tissues are pulled toward the cancerous region, thus resulting in distortion. Therefore, tissues usually become denser when diseased. Higher density is usually an indicator of malignancy. Breast cancer generally have a more irregular shape than benign tumors [23].

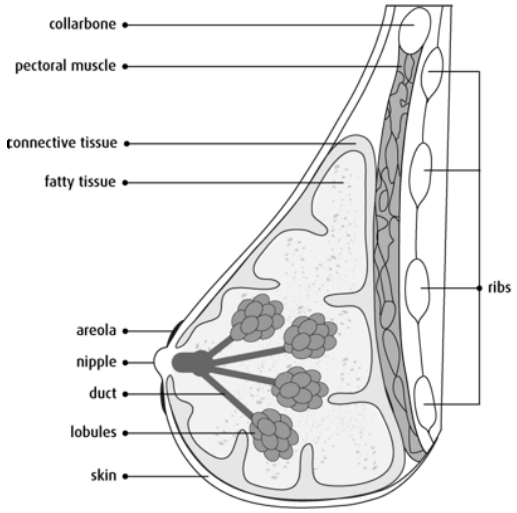

Figure 2.1 Anatomy of normal breast [20]

2.2.2 Dielectric Properties

Electromagnetic based microwave imaging for cancer detection is based on the dielectric properties of breast tissues. The electrical properties of the various tissues in the human body vary widely. Organs consist of a large variety of tissues and are thus strongly heterogeneous.

When radiofrequency (RF) energy is transmitted at boundaries separating regions of different biological materials, the electromagnetic properties of the electromagnetic wave interacting with a medium mainly depend on its penetration depth and transmission coefficient [24]. Tissues with high water content and tissues with low water content have different penetration

depth and transmission coefficient. For an example, the penetration depth of RF plane waves for low water content tissues is about 5 times greater than that for high water content tissues [24]. Typical values of the penetration depth for human tissue of different water content are given in Figure 2.2 [25]. The penetration depth also depends on the wavelength, and its dielectric properties.

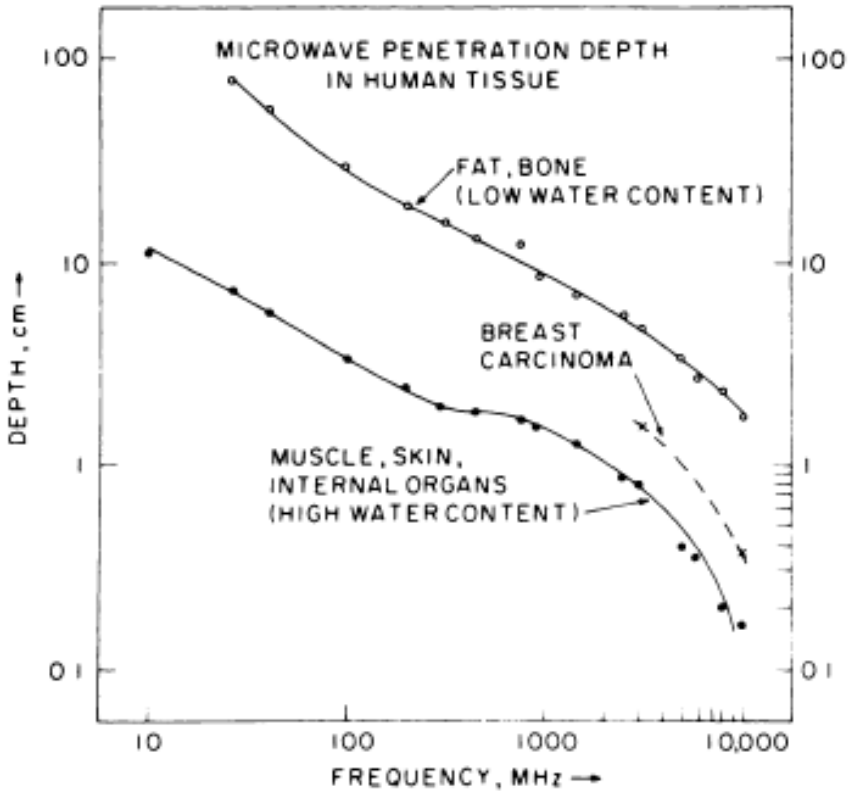

Figure 2.2 Typical values of depth of penetration versus frequency [25]

Many studies have revealed that the content of water in a tissue determines its relative permittivity [26][27][28]. From the studies, tissues with high water content tissues, such as cancer (or tumor), muscle and most organs, have higher relative permittivity than those with low water content tissues such as bone and fat. The relative permittivity of a tissue is related to the storability of electromagnetic energy in the tissue while the conductivity of the tissue indicates the attenuation of microwave energy when the microwave interacts with it.

To illustrate a typical tissue distribution in the human breast, a slice of a magnetic-resonance (MR) image is shown in Figure 2.3. White areas show mostly fatty tissue while darker regions correspond to mostly fibro glandular tissue. Together with the significant loss, this makes the propagation environment very complicated. Tissue heterogeneity is a major problem for the algorithms that process the microwave data to produce images [6].

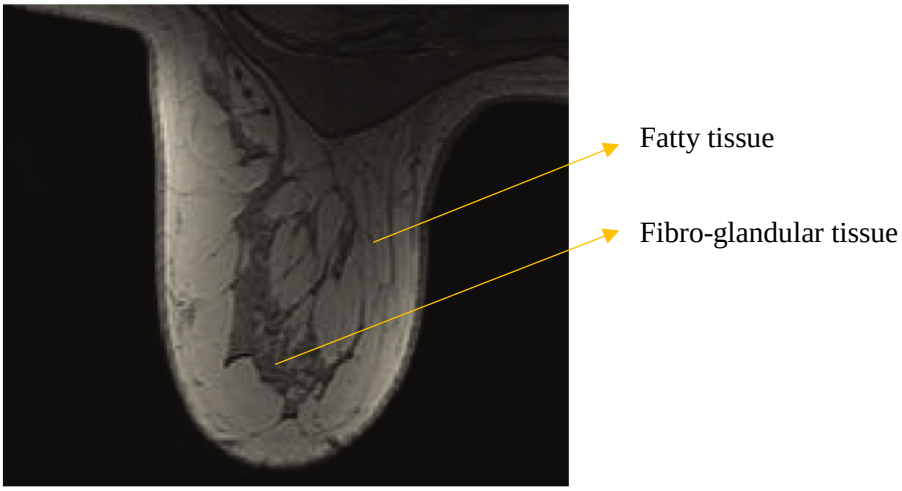

Figure 2.3 A slice of a MR breast image in the transverse plane [6]

The breast cancer detection based on microwave imaging relies on large differences in electromagnetic properties between normal and malignant tissues. A brief description of the definition and widely used models for the dispersion of the tissues is described. In quantitative microwave imaging, considering the biological tissues as dielectrics, the dielectric properties is reconstructed regarding the differences in the complex permittivity, defined by Equation (2.1).

$$\varepsilon^* = \varepsilon_r + j\frac{\sigma}{\omega\varepsilon_0} \tag{2.1}$$

Where ε_r is the relative permittivity and σ is the conductivity of examined object, ε_0 is the free-space permittivity, and ω is the angular frequency.

The electromagnetic properties of breast tissue in different frequency ranges have been

studied. Gabriel et al. made a major review of measured dielectric properties together on healthy human tissues for frequencies between 10 Hz – 100 GHz [26][27][29]. In the study, the basic and well known Debye model in Equation (2.2) is introduced. This equation is extended to Cole-Cole expression to model the structure and composition of biological tissues, defined in Equation (2.3).

$$\varepsilon^*(\omega) = \varepsilon_\infty + \frac{\varepsilon_s - \varepsilon_\infty}{1 + j\omega\tau} \tag{2.2}$$

$$\varepsilon^*(\omega) = \varepsilon_\infty + \frac{\Delta\varepsilon}{1 + j\omega\tau} + \frac{\sigma_s}{j\omega\varepsilon_0} \tag{2.3}$$

where, ε_∞ is static frequency permittivity constants, and σ_s.is static conductivity. The magnitude of the dispersion is $\Delta\varepsilon = \varepsilon_s - \varepsilon_\infty$. The relaxation time constant τ is assumed to be spatially invariant and usually taken between 15 – 17 ps. The approximate properties of human tissues determined by Equation (2.3) for frequency of 2.5 GHz are listed in Table 2.1 [26][27][29].

Table 2.1 Approximate properties of different human tissues at 2.5 GHz

Tissue	Blood	Bone	Adipose	Muscle	Skin (Dry)	Tendon
$\boldsymbol{\varepsilon_r}$	56 – 60	12	4 – 5	50 – 55	38	42
$\boldsymbol{\sigma}$ [$\boldsymbol{S/m}$]	2.5	0.4	0.07 – 0.1	1.8 – 2.2	1.5	1.8

Furthermore, with focus on the breast tumor detection, the female breast tissues have been studied. A clinical study on behavior of electromagnetic field using normal breast were done by Meaney et al. The study reveals that the heterogeneity in the microwave property distribution within the breast is significant, especially as breast density increases [8]. Meanwhile, *ex vivo* measurement of fresh human malignant and normal breast tissues has been performed by several groups. Lazebnik et al. reported the most comprehensive examination of the dielectric properties of normal, benign and malignant breast tissues. The samples were histological categorized in terms of the percentage of adipose (fat), glandular and fibro glandular tissue present in the sample. The

dielectric properties contrast between normal and malignant breast tissues across 0.5 MHz – 20 GHz range have been found to be 10:1 contrast [30]. They also concluded that the dielectric properties of breast tissue were primarily a function of the adipose content of the tissue [28].

The data ranges of values of dielectric properties for modelling adipose, normal tissues, benign tumor and malignant tumors at 3.2 GHz is suggested by Campbell et. al. and shown in Table 2.2. Normal breast tissue is referred as a mixture of glandular and connective tissue [31]. Above studies proving that significant differences in the dielectric properties of breast tissues are sufficient for the microwave image.

Table 2.2 Measured dielectric properties of ex vivo female breast at 3.2 GHz

Tissue type	Normal tissue	Adipose	Tumor (Benign)	Tumor (Malignant)
$\boldsymbol{\varepsilon_r}$	9.8 – 46	2.8 – 7.6	15 – 67	9 – 59
$\boldsymbol{\sigma}$ $[\boldsymbol{S/m}]$	3.7 – 34	0.5 – 2.9	7 – 49	2 – 43

2.3 Breast Cancer Screening

The goal of breast cancer screening is to detect occult breast cancer in a population of women [32]. The most commonly and widely used clinical diagnostic modalities for breast cancer are Clinical Breast Examination (CBE), X-ray Mammography, Magnetic Resonance Imaging (MRI) and Ultra-sound Imaging [33]. The principles of these modalities are summarized as follows.

2.3.1 Clinical Breast Examination (CBE)

CBE is an important part of early detection and it is recommended that CBE be part of a periodic health examinations [32]. In Japan, CBE alone for breast cancer screening have been

performed for many years. A CBE is performed by a healthcare professional who checks the entire breast, underarm, and collarbone area for any lumps or abnormalities. However, it is impossible to detect tumors that cannot be palpated with CBE, thus resulting in a low screening sensitivity. Moreover, no Randomized Controlled Clinical (RCT) trials of breast cancer screening have been carried out to validate the performance of this technique. There have been many reports demonstrating that CBE alone shows no efficacy in reducing mortality of breast cancer [4].

2.3.2 X-ray mammography

Currently X-ray mammography is the most effective method of detecting breast cancer. X-ray Mammography uses X-rays as the examination wave to pass through the breast which is compressed by two plates. Images of the breast are then recorded on film for diagnosis. This process is efficient in terms of time but is quite discomfort due to the breast compression. Moreover, the ionizing radiation involved are hazardous to patients [34]. For most diagnostic requirement, the resulting images are sufficient in terms of spatial resolution, but not promising for the dense breast tissue, which can decrease the sensitivity, and thus the accuracy of mammography [35]. Mammography screening for breast cancer is recommended for women aged 50 years or older due to their breasts tend to be fattier and are easier to evaluate. Mammography can be challenging to perform in young women because their breasts are full of milk glands and tend to be dense [36]. Since 2000, a combination of clinical breast examination (CBE) and mammography has been recommended to Japanese communities as population-based screening [4]-[5].

2.3.3 Magnetic Resonance Imaging (MRI)

Magnetic Resonance Imaging (MRI) utilizes magnets to generate a very strong magnetic fields for the creation of a detailed cross-sectional images of tissue structure [37]. The patient lies on an examination table with several small scanner devices placed around breast to be examined.

MRI has been shown to have a high sensitivity and able to detect cancers accurately that had been overlooked by the other methods [4]. However, its high cost and the time consuming diagnosis are major shortcomings. Although MRI are shown to be efficacious for screening, the tests are limited only to those women at increased risk and not beneficial for women at lower risk [32]. Recently, a revised guidelines for MRI breast cancer screening as an adjunct to mammography was issued by the American Cancer Society (ACS) [37].

2.3.4 Ultrasound Imaging

Ultrasound is an imaging test that sends high frequency sound waves (> 20,000 Hz), through the breast and converts them into images on a screen. The radiation in this frequency range is not harmful to patients. This method is cheaper than MRI and less invasive compared to mammography. Moreover, it is portable and the resulting images are in real-time screening [38]. Hence, the diagnosis of cancer is dependent on the skills of doctor or physician who interpreted the results. It may be difficult to detect and distinguish fluid-filled cyst and solid cancerous tissue. Ultrasound is used to complement other screening tests and recommended for patients in whom mammography and palpation have failed to detect abnormalities [39].

2.4 Microwave Imaging

Although the efficacy of aforementioned detection modalities have been demonstrated, an alternative to current breast cancer screening methods is required to overcome the limitations. One of the most promising emerging breast imaging technologies is Microwave Imaging (MWI). The major reason for this is the significant differences in dielectric properties between cancerous tissues and normal breast tissues, as explained in Section 2.2.2. Moreover, MWI for breast screening is non-mammographic imaging technologies, and has advantages which are nonionizing (safe), noninvasive (comfortable), less painful, and potentially low cost. The goal of MWI is to

image all the breast tissue with high contrast and high resolution with as little noise as possible to permit the detection and diagnosis of breast cancer at as small size and early stage as possible.

A microwave is heavily influenced by diffraction. Therefore, MWI obtaining images of a biological object's material properties by measuring the object's influence on an applied wave (either acoustic or electromagnetic), depicted in Figure 2.4. In microwave case, the contrast in dielectric properties is imaged.

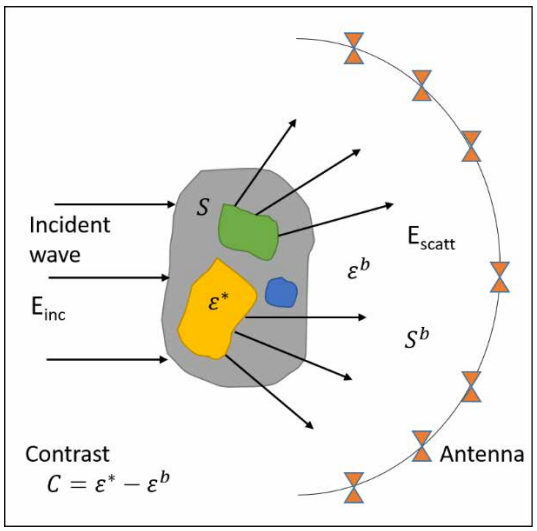

Figure 2.4 Formulation of the scattering properties in microwave imaging

Microwave imaging systems for breast cancer detection can be classified into passive and active microwave imaging, as shown in Figure 2.5. Passive microwave imaging is based on the thermography, which is high temperature difference between the cancerous and healthy tissues when the breast is illuminated by microwave radiation. The received microwave signals often used to map the temperature distribution for diagnosis. Meanwhile active microwave imaging refers to a system that irradiate electromagnetic waves to the imaging region and measure the resulting electromagnetic fields [25], [40], [41]. This approach relies on the large difference in dielectric properties between healthy and malignant breast tissues [13][14].

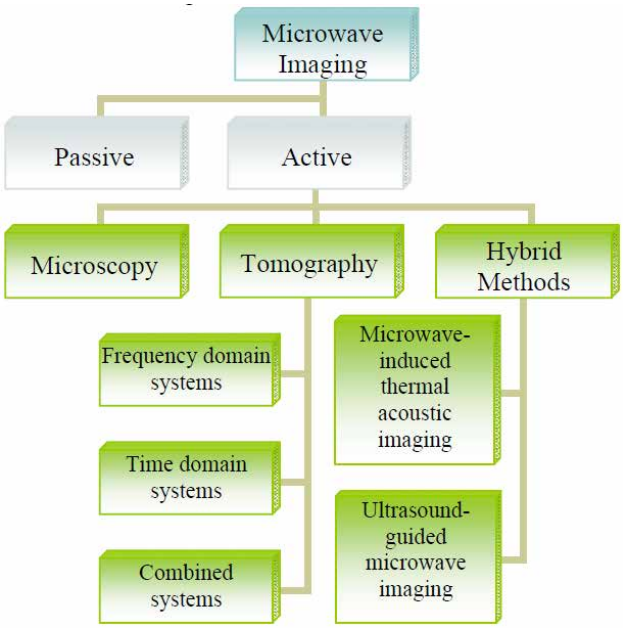

Figure 2.5 Microwave imaging systems for breast cancer diagnosis [41]

Two active microwave imaging methods have been proposed, namely ultra-wideband (UWB) radar based imaging and microwave tomography. In a radar-based approach, the goal is to generate an image of the relative scattering strength, thus only focuses on imaging the cancer rather than the whole breast. Whereas in microwave tomography approach, the goal is to quantitatively reconstruct the dielectric parameters in the imaging region, in other words, attempts to reconstruct a map of all of electrical properties of the breast.[42]. The difference between a qualitative and a quantitative image is that the quantitative image provides information directly correlated to the internal structure and composition of the examined object, which is necessity in biomedical and geo-surveying applications.

Recently, studies on the early detection of breast cancer by active MWI have been proposed over the years and have attracted considerable interest among researchers [6]. The initial and major contribution in active MWI for breast cancer screening has been done by Meaney et. al. using tomographic approach [43]–[45]. Meanwhile the review using a radar approach are published by Hagness et. al. [10]–[12].

2.4.1 Ultra-wideband (UWB) Radar

Time-domain UWB radar techniques are based on radar principles in which one seeks to determine the location-of-origin of the scattered time-domain signal [25]. UWB pulses are transmitted from antennas at different locations near the breast surface and the backscattered responses from the breast are recorded, from which the image of the backscattered energy distribution is reconstructed coherently [46].

Kuwahara et al. have developed a multi-static UWB radar measurement system for early detection of breast cancer among Japanese women and conducted clinical experiments [13]–[18]. Figure 2.6 shows the developed microwave mammography system. Three different sensors with different number of antennas were prepared to accommodate the breast size. The measurement was taken with limited bandwidth from 4 – 9 GHz. The influence of surrounding structures is avoided by immersing the antenna and imaged object into a lossy matching fluid.

From the clinical experiments, the image reconstruction results demonstrated that the system can detect cancer which has a clear boundary and isolated from fibro glandular tissue. However, if the boundary of the fibro-glandular tissue and the cancer is irregular, the system was unable to reconstruct the shape of the cancer correctly in some cases because of the complicated multipath propagation in the breast. Thus, the screening method using UWB radar proposed by Kuwahara et al. can be considered incomplete and require further improvements.

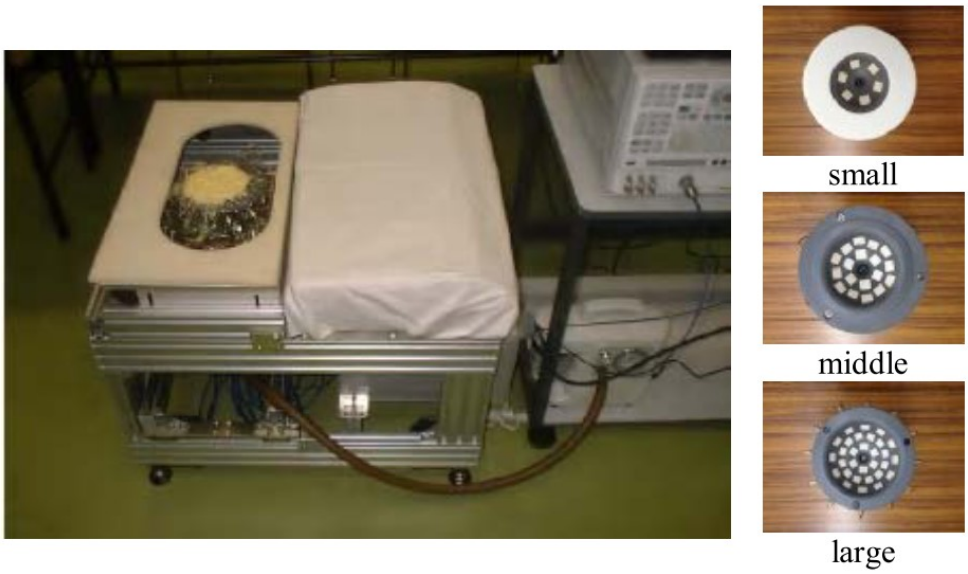

Figure 2.6 Microwave mammography with different sensors [13][14]

2.4.2 Microwave Tomography

The word tomography comes from the Greek words "to slice" (tomos) and "to write" (graphein). This term comes to microwave imaging from the image processing algorithms and is also known from magnetic resonance tomography (MRT) and X-ray computed tomography (CT), where the image of the internal structures of a body is represented slice by slice [41].

In microwave tomography (MWT), a number of antennas are located around the unknown object, as shown in Figure 2.7. The examined object is successively illuminated by transmitting antenna and the resulting electromagnetic field is measured by the receiving antennas. The measurement data are related to the scattered field resulting from the interaction between the known incident field and the scatterers inside the imaging region [47]. The measurement data is then used with an appropriate nonlinear inversion algorithm to reconstruct the dielectric properties distribution of the object, so as to generate quantitative images [24],[25][48].

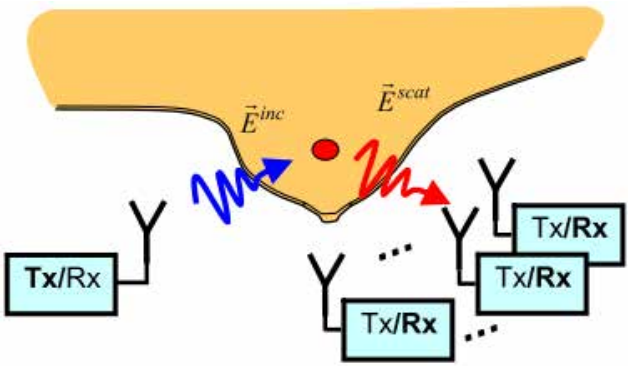

Figure 2.7 Breast screening by microwave tomography [41]

The imaging system with a clinical prototype to perform quantitative images of breast phantoms was developed by Meaney et. al. [49]. Furthermore, Kuwahara et al. currently developing a microwave tomography (MWT) system for pathology diagnosis to overcome the limitations in previous developed UWB radar imaging [50][51][52]. Microwave tomography is most interest in this thesis and will further discussed in Chapter 3.

CHAPTER 3

MICROWAVE TOMOGRAPHY

3.1 Overview

Tomography is a voxel-based problems, and is based on the inverse scattering problem. It is an iterative technique can be used to reconstruct complex dielectric properties of objects from measurements of the field (either acoustic or electromagnetic) scattered when the object is illuminated by known sources [53]. This chapter discusses the background of MWT in regard to the physical description, the numerical forward problem, and the iterative non-linear inverse scattering. Furthermore, the challenges in tomography as the motivation of research are also outlined.

3.2 Physical Description

Figure 3.1 shows the geometry for a two-dimensional (2-D) case, where the transmitter can be modeled by an incident plane wave or a source of cylindrical waves. The receiving points may be arranged along a line behind or along a circle around the object [54].

Consider an inhomogeneous dielectric objet S of arbitrary shape and unknown complex permittivity $\varepsilon^*(r)$, which consists of relative permittivity $\varepsilon_r(r)$ and conductivity $\sigma(r)$. The object is surrounded by a background medium S^b of complex permittivity $\varepsilon^b(r)$, and antenna array located outside of volume S. In Figure 3.1, $\varepsilon(x,y)$, ε_{ext} and e_l^i are defined with $\varepsilon^*(r)$, $\varepsilon^b(r)$, and e_v^i, respectively for 3-D application and further description. In sequence, each antenna transmits an electromagnetic signal into the imaging region, while the transmitter itself and other antennas in the array act as receivers. Then the scattered electric field is measured, which is the result of the interaction between the unknown object and incident field from the transmitting point.

General Gauss-Newton linearized solutions can be used to solve electromagnetic problems in 2-D and 3-D. The procedure are (1) forward problem (2) calculation of sensitivity matrix (Jacobian), and (3) solution of a large matrix in inverse problem [55].

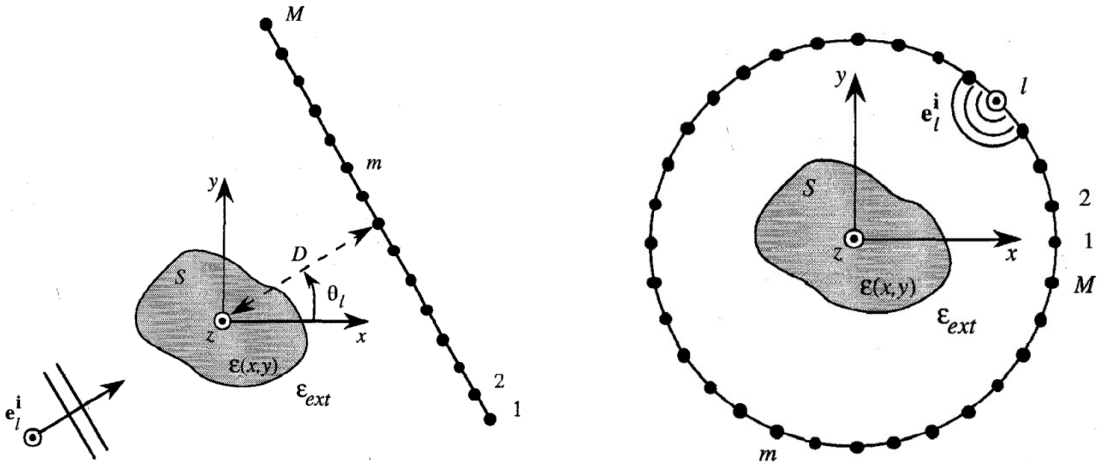

(a) Linear (planar) (b) Circular

Figure 3.1 Imaging system geometries [54]

3.1 Forward Problem

Solving the forward problem (or known as direct problem) gives the computed field at the receiving points. Several different methods can be used to implement the wave equation into the forward problem, including the Method of Moment (MoM) and Finite-Difference Time-Domain (FDTD). MoM is the conventional approach for solving volume integral equations in the frequency domain. Here, the integral Helmholtz formulation using MoM will be discussed.

I. Wave Equation

A common wave equation is the scalar Helmholtz's equation describing the time-harmonic electric field in a situation, where the incidence field is a vertically polarized and the object properties is homogenous along the vertical z-axis. The problem is then transformed into a 2-D problem, defined by Equation (3.1) [47][56].

$$\left(\nabla^2 + k^2(r)\right)e(r) = 0 \tag{3.1}$$

where k is the wavenumber of the electromagnetic (EM) wave containing the dielectric properties of the medium of propagation, and $e(r)$ is the total electric field.

II. Formulation of Integral Equation

The formulation used in this thesis is based on the integral formulation of the scalar Helmholtz's equation using MoM. The total field $e_v(r)$ in Equation (3.1) is assumed to be the sum of the incident field e_v^i (without an object) and the scattered field e_v^s (caused by the object), according to Equation (3.2).

$$e_v(r) = e_v^i(\mathrm{r}) + e_v^s(r) \tag{3.2}$$

where the notation v indexing the total number of views which is a multi-view process by rotating the receivers. The incident field e_v^i is assumed as the homogeneous solution of the Helmholtz's equation without object. Meanwhile, the scattered field e_v^s is the solution of the inhomogeneous Helmholtz's equation defined in Equation (3.3). In this case the object is described as a number of small source points generating the scattered field defined by the Dirac delta function in the right side of Equation (3.3).

$$(\nabla^2 + k_b)\, G(r, r') = -\delta(r - r') \tag{3.3}$$

Note, that the index r represent the observation points (i.e. the receiving antennas), meanwhile r' represents the source point inside the object region. The term $G(r, r')$ represent the three-dimensional (3-D) free-space Green's function, and k_b is the wavenumber of the background medium. The Dirac delta function can be defined as the equivalent currents J_v inside the object generated by the contrast of the complex permittivity $C(r')$ between the object and the total field $e_v(r')$ inside the object region as defined in Equation (3.4).

$$J_v = e_v(r')C(r') \tag{3.4}$$

Where
$$C(r') = {k^2}_{obj}(r') - k_b^2 \tag{3.5}$$

and $$k^2{}_{obj}(\mathrm{r}') = \omega^2\mu_0\varepsilon^*(r') \tag{3.6}$$

$$k_b^2 = \omega^2\mu_0\varepsilon^b \tag{3.7}$$

μ_0 is the permeability of free space, and the difference of the two wavenumbers in Equation (3.6) and (3.7) is the complex permittivity ε^* of the object and the background medium ε_b^* [57]. The contrast $C(r')$ over volume S with respect to the known ε_b^* may also defined as $\varepsilon^*(r') - \varepsilon_b^*$ if $r' \in S$. By inserting Equation (3.4) into (3.3) gives the solution of the scattered field e_v^s on the receivers in form of a convolution in the integral formulation as written Equation (3.8).

$$e_v^s(r) = \iint_S \; G(r,r')\, e_v(r')\, C(r') \;\; dr' \tag{3.8}$$

By inserting Equation (3.8) in (3.2) gives the following linear system for the total field.

$$e_v(r) = e_v^i(r) + \iint_S \; G(r,r')\, e_v(r')\, C(r') \;\; dr' \tag{3.9}$$

Equation (3.8) and (3.9) define a forward scattering problem when the object of contrast C is given besides the incident field e_v^i in S and the background medium complex permittivity ε_b^*, and if the scattered field e_v^s is unknown [54]. The inner product $G(r,r') \cdot e_v(r')$ in Equation (3.9) may represented as follows [7]:

$$G(r,r') \cdot e_v(r') = \begin{bmatrix} G_{xx}(r,r') & G_{xy}(r,r') & G_{xz}(r,r') \\ G_{yx}(r,r') & G_{yy}(r,r') & G_{yz}(r,r') \\ G_{zx}(r,r') & G_{zy}(r,r') & G_{zz}(r,r') \end{bmatrix} \begin{bmatrix} e_x(r') \\ e_y(r') \\ e_z(r') \end{bmatrix} \tag{3.10}$$

Let $\quad x_1 = x \quad x_2 = y \quad x_3 = z$

Then, $G_{x_p x_q}(r,r')$ is given by

$$G_{x_p x_q}(r,r') = -j\omega\mu_0 \left[\delta_{pq} + \frac{1}{k_0^2}\frac{\partial^2}{\partial x_q \partial x_p}\right]\psi(r,r'), \quad p,q = 1,2,3$$

$$\psi(r,r') = \frac{\exp(-jk_0|r-r'|)}{4\pi|r-r'|}$$

$$k_0 = \omega(\mu_0\varepsilon_0)^{1/2}$$

III. Transformation to Matrix Equation

The integral equation formulations in Equation (3.8) and (3.9) can be transformed into a matrix equations using MoM. By choosing pulse function basis and point matching, the object is divided into N subvolumes (or cells). The same pulse-basis functions are used for the contrast and the total field, meaning that $e_v(r')$ and $C(r')$ are constant in each subvolume [54][58]. The relation between the values of the scattered field at M points in N cells is given in Equation (3.11).

$$e_v^s(r_m) = \sum_{j=1}^{N} G(r_m, r_j)\, C(r_j)\, e_v(r_j), \qquad m = 1,2,\cdots,M \tag{3.11}$$

where m is the index of the observation point around the object (receivers), depicted in Figure 3.1, and j is the index of the source point in square cells of the object. The v-term indicates the total number of measurements [19]. Before calculating the scattered field, the total field inside the object must be calculated by solving linear system. The total field in N cells is solution of the following equation.

$$e_v^i(r_n) = \sum_{j=1}^{N} \left[\delta_{nj} - G(r_n, r_j)\, C(r_j)\right]\, e_v(r_j), \qquad n = 1,2,\cdots,N \tag{3.12}$$

where n is the index of the observation point inside the object and j is the index of the source point inside the object. From Equation (3.12) the object's influence of the field inside itself is included. Equation (3.11) and (3.12) may be rewritten in matrix form as Equation (3.13) and (3.14), respectively.

$$[E_v^s] = [G^s][C][E_v] \tag{3.13}$$

$$\left[E_v^i\right] = [I - G^r C][E_v] \tag{3.14}$$

Where $[E_v^s]$ is a vector with length M while $[E_v]$ and $\left[E_v^i\right]$ are vectors with length N. The $[C]$ matrix is an $N \times N$ diagonal matrix containing the permittivity contrast of the N cells, and I is the identity matrix of size $N \times N$. The $[G^s]$ and $[G^r]$ matrix contains the Green's operator and have the sizes of $M \times N$ and $N \times N$, respectively. Including a multi-view process with

receiver rotation, the matrix formulation got increasing sizes of the matrixes in Equation (3.13) and (3.14), obtaining Equation (3.15) and (3.16), respectively.

$$[E^s] = [G^s][C][E] \tag{3.15}$$

$$[E] = [I - G^r C]^{-1}\left[E^i\right] \tag{3.16}$$

We can determine the total electric field at each of the N cells by inverting $[I - G^r C]$ as shown in Equation (3.16). $[E]$ is the total field and $\left[E^i\right]$ is the incidence field inside the object region, and $[E^s]$ is the scattered field at the receiving points. The $[E]$ and $\left[E^i\right]$ vectors have the size TN, where T is the number of transmitters and N is the number of cells in the object region. The scattered field $[E^s]$ is a vector of size TM, where M is the number of measurement points. The details on the transformation to matrix equation, and evaluation of matrix diagonal and off-diagonal elements of Green's Function are further elaborated in Appendix A and [7].

3.2 Inverse Problem

In most situations of biomedical applications, where larger objects with a large contrast respect to the background medium, a non-linear method is needed [59]. Tomographic method is based on the non-linear inverse scattering to obtain quantitative images of larger high contrast objects. The inverse problem is formalized by finding the position and complex permittivity distribution of the unknown object from the measured scattered field (forward problem as described in Section 3.1).

First, a specific objective function m of the model need to be defined and then minimized. Generally, the objective function is tailored so that the solution from the inverse algorithm is "close" to the actual or reference model, and also that the reconstructed model has "minimum structure" in some sense. The model is parameterized as

$$m = \sum_{i=1}^{M} m_i \psi_i$$

Where ψ_i are the basis functions defined in the imaging region S, and m_i are constants. The basis functions are chosen to be rectangular prisms of unit amplitude, and hence m_i is the value of the model in the *i*-th cell. Because the goal is to find a model which minimizes a specific objective function, the inversion results should not depend upon the model parameterization. In order to accomplish this, the examined object is fine discretized into square cells (or voxels), hence the number of cells are large, especially in 3-D models [55]. In each voxel, the complex properties are estimated, which consist of the relative permittivity and conductivity distribution.

Optimization is a process of searching. For continuous problems with complicated object functions and large number of variables, such as the inverse problem, the indirect methods of optimization is practical. Indirect methods often referred as gradient-based optimization techniques, and approach the optimum solution in an iterative process. Newton's method, Gauss-Newton method, Levenberg-Marquardt method, conjugate gradient method and many other variants belong to this category [60]. The inverse problem involves three major steps in each iterations:

(1) Minimize the difference or error between the measured scattered field and the calculated scattered field (to find the global minimum).

(2) From (1), find the Jacobian matrix J, (the derivate-matrix of the computed scattered field with respect to the complex contrast in the object).

(3) Update the contrast distribution of the object under investigation.

This process continues until the error is sufficient small, thus the reconstructed image of the object is the complex permittivity map used in the direct problem, depicted in Figure 3.2. The electromagnetic inverse scattering problem may be solved utilizing Newton-Kantorovich (NKT) [58], [61], and Distorted Born Iterative Method (DBIM) [62]–[64].

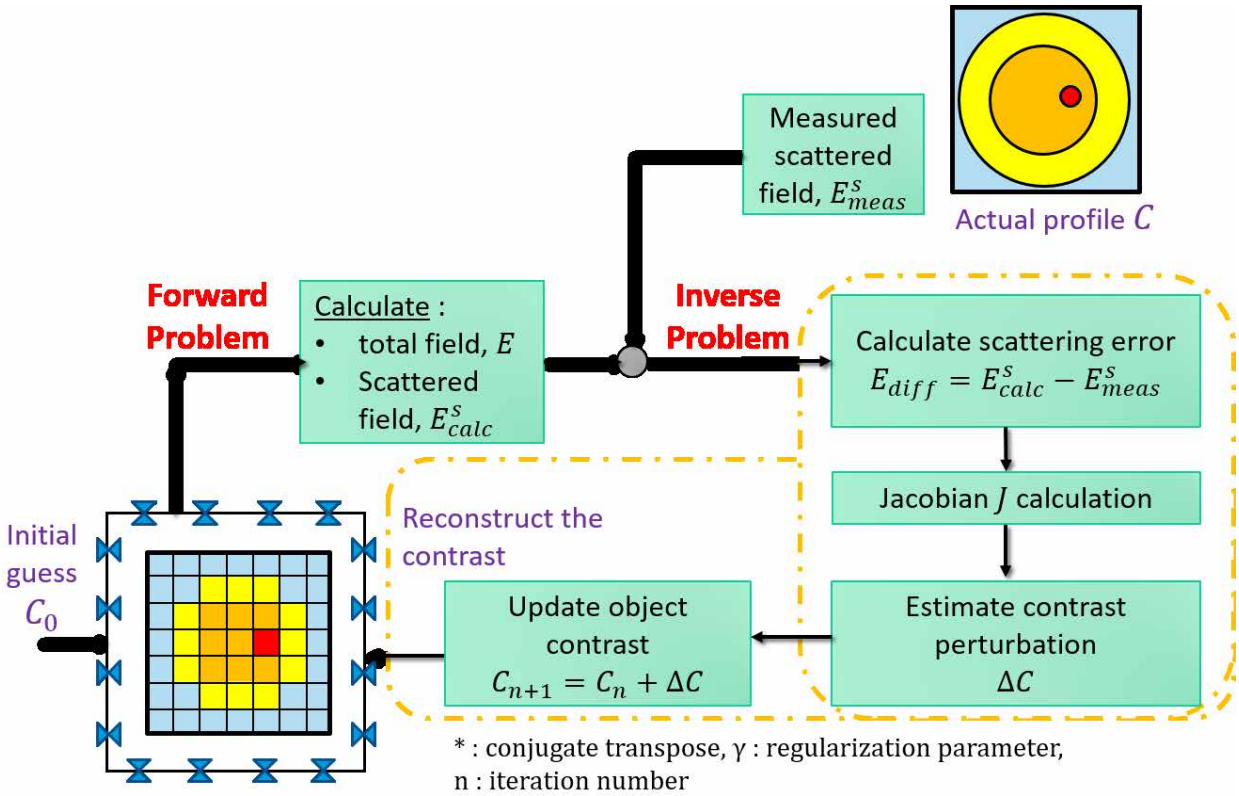

Figure 3.2 Flow-chart of the microwave tomography-based breast imaging

3.2.1 Newton-Kantorovich (NKT)

Newton-Kantorovich (NKT) is a Newton-based least square method, a step by step algorithm which if converging, tends towards an exact solution [61][58]. In this thesis, the code developed by Joachimowicz et. al. [58] is extended into a 3-D configuration solution. By starting from a defined residual as the difference between the calculated scattered field in the forward problem, $E^s_{calc}(C)$, and the measured scattered field, E^s_{meas}, as Equation (3.17).

$$E_{diff} = E^s_{calc}(C) - E^s_{meas} \tag{3.17}$$

The optimization will then be performed on the square norm $F(C)$

$$F(C) = \|E^s_{calc}(C) - E^s_{meas}\|^2 = min \tag{3.18}$$

where the C is the complex permittivity distribution matrix used in the forward problem. The goal is then to find the global minimum of this function. Using the Newton method, both the

gradient and the Hessian matrix of the function needs to be defined. The gradient be calculated as Equation (3.19) and the Hessian matrix as Equation (3.20).

$$\nabla_C F(C) = J^*(C) E_{diff}(C) \tag{3.19}$$

$$H_F(C) = J^*(C)\, J(C) + \sum_{i=1}^{M} E^i_{diff}(C) H^i_{E_{diff}}(C) \tag{3.20}$$

Where $J(C)$ is the Jacobian of the residual $E_{diff}(C)$ with respect to the contrast C, M is the number of observation points, and * denotes the conjugate transpose. The estimation of the step ΔC in the optimization done using the following linear system

$$H_F(C)\, \Delta C = \nabla_C\, F(C) \tag{3.21}$$

The Hessian matrix defined in Equation (3.20) is usually hard to compute in practical problems. Therefore Equation (3.21) is often simplified by using a Gauss- Newton method as

$$J^*(C)\, J(C)\, \Delta C = J^*(C) E_{diff}(C) \tag{3.22}$$

The computation of the Jacobian matrix J is a central part of the optimization process. J is the derivative matrix containing the scattered field dependence of the contrast C inside the object, where $J(C) = [\delta F(C)/\delta C]$ with elements of $[J]_{ij} = \delta F_i/\delta C_j$ [55]. An analytical expression for J is derived in Appendix B. Equation (3.22) can be solved for a least square solution, which is equivalent to solving the matrix equation in Equation (3.23).

$$\Delta C = [J^*(C)\, J(C)\,]^{-1}\, J^*(C) E_{diff}(C) \tag{3.23}$$

By introducing this relation into an iterative procedure, the initial nonlinear relation characterizing the inverse scattering problem can be transformed by a sequence of linear ones. However, this solution is very limited while it has no control to find the global minimum, (of Equation (3.18)), while the implementation does not support regularization to avoid local minima. Therefore the Newton-Kantorovich method is used. In this method, the $[J^*(C)\, J(C)\,]^{-1}$ in Equation (3.23) is extended with a regularization parameter, γ, as in Equation (3.24).

$$\Delta C = [J^*(C)\, J(C) + \gamma I]^{-1} J^*(C) E_{diff}(C) \tag{3.24}$$

Instead of solving Equation (3.23), the computation of the contrast step ΔC may be derived from Equation (3.24) or (3.25) with the known Jacobian matrix.

$$\Delta C = [J^* J + \gamma I]^{-1} J^* E_{diff} \tag{3.25}$$

Here, $[J^* J + \gamma I]^{-1}$ is an ill-conditioned situation, where small errors on the data may produce unphysical solution. The numerical instability of the inverse problem is here related to the large condition number of the matrix $J^* J$. The regularization parameter, γ is used to improve the convergence of an ill-posed problem. The parameter is chosen to lower the condition number of the $J^* J$ matrix, which stabilizes the convergence to avoid local minima. For an example, a large regularization parameter is needed when the convergence is far from the expected solution and a small regularization parameter is needed when the error is small and the convergence is close to the global minima.

However, to decrease the condition number, a strong regularization process may remove useful components and decrease the spatial resolution. One must look for a solution stable and accurate at once. As a consequence, the regularization parameter γ must be chosen in order to accommodate a convenient spatial resolution-stability compromise. Therefore, the regularization of the optimization is a major issue during the non-linear inverse scattering in microwave imaging. This parameter is determined in each iteration using a priori information. Another, very important factor is the initial guess. Choosing a proper starting point for the convergence has a major influence on the ability to find the global minimum, or a physically correct image.

In this thesis, γ is taken as

$$\gamma = \alpha \frac{\text{trace}\,[J^* J]}{N} [err_s]^2 \tag{3.26}$$

$$err_s = \sqrt{\frac{\sum_{i=1}^{M} \left|E_R^S(i) - E_{meas}^S(i)\right|^2}{\sum_{i=1}^{M} |E_{meas}^S(i)|^2}} \tag{3.27}$$

Where α represents the magnitude of γ, and the initial value is chosen intuitively, and is

determined empirically according to the convergence of the process. The trace of the matrix $J^* J$ in order to reduce the gap between its higher and lower eigenvalue and thus to improve its conditionment. The relative mean square (RMS) error of the scattered field err_s (M: number of observation points), in order to decrease the weight of γ during the process [58]. The new contrast is updated in each iteration as

$$C_{n+1} = C_n + \Delta C \tag{3.28}$$

where n is the iteration number. These steps are repeated according to Figure 3.2, as long as the convergence criteria on the RMS error of the scattered field is not reached.

3.2.2 Distorted Born Iterative Method (DBIM)

I. Electromagnetic inverse scattering and Born approximation

As explained in Section 3.2.1, an estimate of the unknown complex permittivity $\varepsilon^*(r)$ in S is reconstructed based on a relationship between the fields scattered from the imaging region and the contrast of the complex permittivity within that region. Based on Equation (3.8), for a measurement at an observation location r at a given frequency, the scattered electric field can be expressed by an integral equation

$$\begin{aligned} E^s(r) &= E^t(r) - E^i(r) \\ &= k_0^2 \int_S \bar{G}^b(r|r')\, E^t(r')[\varepsilon^*(r') - \varepsilon^b(r')]\, dr' \end{aligned} \tag{3.29}$$

where E^i is the incident field in the presence of the background medium permittivity $\varepsilon^b(r)$, and k_0 is the free-space wavenumber. E^s is the scattered electric field, which is the difference between the total field observed in the object environment and the total field observed in the background environment. The scattered field results from the re-radiation of the total field E^t in volume S, and the difference between the complex permittivity of the unknown region $\varepsilon^*(r)$ and the background medium $\varepsilon^b(r)$. The difference $\varepsilon^*(r) - \varepsilon^b(r)$ is the unknown quantity of interest,

and known as the contrast function C in Equation (3.8). The scattering field due to the contrast function at $r \in S$ is determined by the dyadic Green's function $\bar{G}^b(r|r')$ of the background medium [62][63].

The total field E^t in S depends on the multiple scattering interactions between the features of the complex permittivity. Therefore, the scattered field E^s is nonlinearly related to the contrast function due to the product $E^t(r)[\varepsilon^*(r) - \varepsilon^b(r)]$ in the integrand of Equation (3.29). Here, the distorted Born iterative method (DBIM) is employed, where the non-linear relation can be linearized using the Born approximation. At each iteration of the DBIM, the total field within the actual permittivity in S is approximated by the total field in the background medium $\varepsilon^b(r)$, i.e. E^b replace E^t in Equation (3.29). The approach requires computation of the fields at the antennas and inside S for each iteration of the background medium.

II. Linear system of scattering equation

Here, the formulation of linear system of scattering equation in Equation (3.29) is explained. The first-order Born approximation to Equation (3.29) is linear in the unknown contrast function $\varepsilon^*(r) - \varepsilon^b(r)$. For simplicity, the contrast function of Equation (3.29) are replaced by the frequency-dependent non-Debye model of Equation (2.1), which are relative permittivity ε_r and conductivity σ. Equation (3.30) defines a general parametric model of complex function.

$$\varepsilon^*(\omega) - \varepsilon^b(\omega) = \mathcal{F}(\omega,\ \varepsilon_r, \sigma) - \mathcal{F}(\omega, \varepsilon_r^b, \sigma^b) \tag{3.30}$$

$$\mathcal{F} = \sigma + j\omega\varepsilon_0\varepsilon_r$$

Using Equation (3.30), the multiple observation linear scattering system of Equation (3.29) can be transformed to Equation (3.31).

$$e^s = \left[\frac{\partial \mathcal{F}}{\partial \varepsilon_r}\mathbf{B} \quad \frac{\partial \mathcal{F}}{\partial \sigma}\mathbf{B}\right]\begin{bmatrix}\varepsilon_r - \varepsilon_r^b \\ \sigma - \sigma^b\end{bmatrix} \tag{3.31}$$

$$\mathbf{B} = \begin{bmatrix} \mathbf{H}_{1,1} \\ \mathbf{H}_{2,2} \\ \vdots \\ \mathbf{H}_{M,N} \end{bmatrix}, \qquad \mathbf{H}_{m,n} = \begin{bmatrix} \bar{G}^b(r_n|r'_1)\, E^b(r'_1|r_m) \\ \bar{G}^b(r_n|r'_2)\, E^b(r'_2|r_m) \\ \vdots \\ \bar{G}^b(r_n|r'_K)\, E^b(r'_K|r_m) \end{bmatrix}^T \in C^{3\times K}, \qquad \begin{matrix} m = 1, \cdots, M \\ n = 1, \cdots, N \end{matrix}$$

Where $\boldsymbol{B}$ is the matrices that associated with each observations, and collected as the block-rows of a larger matrix. M and N are numbers of transmitting and receiving antenna, K is number of voxels within volume S, and T is transpose of the matrix. The coefficients $\partial\mathcal{F}/\partial\varepsilon_r$ and $\partial\mathcal{F}/\partial\sigma$ must be constant so that the system remains linear in the unknown parameters [62]. The contrast function $\varepsilon^*(r) - \varepsilon^b(r)$ over $r \in S$ is compactly denoted as $\delta\{\varepsilon^*(r)\}$. Thus the contrast functions of these two parameters, which are $\delta\{\varepsilon_r(r)\}$, and $\delta\{\sigma(r)\}$, are the new unknowns over $r \in S$. Since these two parameters are all real-valued, Equation (3.31) is split into a pair of real and imaginary equations so that the solution space is limited to real values.

For an array of N antennas, there are N^2F total frequency-domain measurements, where F is the number of discrete frequencies to be included in the solution. Each of N^2F measurements yields a pair of real and imaginary vector equations. The resulting set of $M = N^2F$ equations is then discretized over the reconstruction region S. The imaging region S is discretized to obtain the set of K voxels and vectorized, so that the unknown contrast function for each parameter forms $K \times 1$ vector. The two vectors are collected into a single $2K \times 1$ vector $\mathbf{c}$. For each equation, the remaining elements of the summand form a $2MF \times 2K$ matrix $\mathbf{A}$. The differences between the measured fields and the calculated fields (computed by the forward problem) are collected into a vector of residual scattered fields $\mathbf{b}$ with size of $2MF \times 1$. In this thesis, we use single frequency ($F = 1$) for each transmit-receive antenna pair. From Equation (3.31), the resulting linear system as expressed in Equation (3.32) is denoted as $\mathbf{A}\,\mathbf{c} = \mathbf{b}$, then is structured for each channel d between a transmitter at r_m and a receiver at r_n.

$$\begin{bmatrix} \Re\left\{\frac{\partial \mathcal{F}}{\partial \varepsilon_r}\mathbf{B}_1\right\} & \Re\left\{\frac{\partial \mathcal{F}}{\partial \sigma}\mathbf{B}_1\right\} \\ \vdots & \\ \Re\left\{\frac{\partial \mathcal{F}}{\partial \varepsilon_r}\mathbf{B}_M\right\} & \Re\left\{\frac{\partial \mathcal{F}}{\partial \sigma}\mathbf{B}_M\right\} \\ \Im\left\{\frac{\partial \mathcal{F}}{\partial \varepsilon_r}\mathbf{B}_1\right\} & \Im\left\{\frac{\partial \mathcal{F}}{\partial \sigma}\mathbf{B}_1\right\} \\ \vdots & \\ \Im\left\{\frac{\partial \mathcal{F}}{\partial \varepsilon_r}\mathbf{B}_M\right\} & \Im\left\{\frac{\partial \mathcal{F}}{\partial \sigma}\mathbf{B}_M\right\} \end{bmatrix} \begin{bmatrix} \delta(\varepsilon_r)_1 \\ \vdots \\ \delta(\varepsilon_r)_K \\ \delta(\sigma)_1 \\ \vdots \\ \delta(\sigma)_K \end{bmatrix} = \begin{bmatrix} \Re\{E_1^s\} \\ \vdots \\ \Re\{E_M^s\} \\ \Im\{E_1^s\} \\ \vdots \\ \Im\{E_M^s\} \end{bmatrix} \tag{3.32}$$

$$\delta(\varepsilon_r) = \varepsilon_r - \varepsilon_r^b \qquad \delta(\sigma) = \sigma - \sigma^b$$

$$\partial\mathcal{F}/\partial\varepsilon_r = j\omega\varepsilon_0 \qquad \partial\mathcal{F}/\partial\sigma = 1$$

Where the $\Re\{\ \}$ and $\Im\{\ \}$ operators denote the real and imaginary parts of the complex argument in matrix $\mathbf{A}$.

The linear system $\mathbf{A}\,\mathbf{c} = \mathbf{b}$ in Equation (3.32) is a multi-static, single frequency, linearized description of the scattering with respect to the contrast function, and formulated in the non-Debye model. The linear system utilizing three parameters of Debye model $\varepsilon_\infty, \Delta\varepsilon,$ and σ_s of Equation (2.2) can be derived in the same manner. Moreover, observations at multiple frequencies can be added to the linear system of scattering equations by vertically concatenating the multiple-observation vectors at each of the frequencies. The solution of this system, i.e. $\mathbf{c}$, yields an estimate of the contrast function of the unknown object [63].

III. DBIM implementation

The DBIM has been used as an alternative iterative method to solve the 2-D nonlinear inverse scattering problem [56]. The DBIM is equivalent to a Gauss–Newton approach [65] to nonlinear least-square optimization problems, as described in Section 3.2.1, to estimate the contrast function from the observations of nonlinear scattering.

This method begins with an initial guess for the background permittivity that may include any available a *priori* information about the object permittivity. At each iteration, MoM is used in the forward problem to efficiently compute a system of scattering equations, which consists of the background fields and Green's functions (i.e. measurements data). In the inverse problem, the

solution of system, $\mathbf{c}$, yields an estimate of the contrast function of the unknown object, $\delta\{\widehat{\varepsilon_r}(r)\}$, and $\delta\{\hat{\sigma}(r)\}$, which are then combined into an estimate of the complex permittivity contrast $\delta\{\widehat{\varepsilon^*}(r)\}$. The contrast perturbations $\delta\{\widehat{\varepsilon^*}(r)\}$ is used to update the estimated object permittivity. The updated object permittivity is added to the K cells of the *i*-th background permittivity to create the new background, as expressed in Equation (3.33).

$$\varepsilon^b{}_{i+1}(r_k) = \varepsilon^b{}_i(r_k) + \delta(\widehat{\varepsilon^*}(r_k)), \quad k = 1,2,\cdots,K. \;\; r_k \in S \tag{3.33}$$

For next DBIM iteration, the total field and the scattering field at the forward problem are recalculated based on the new background permittivity $\varepsilon^b(r)$. The DBIM algorithm alternates between forward and inverse problems, while updating the $\varepsilon^b(r)$ at each iteration. As the estimate is improved, the difference in the scattering from the background permittivity and the object permittivity decreases at each iteration. The DBIM algorithm is terminated when convergence is reached in the minimization of the residual scattering $\|\mathbf{b}\|$. In this thesis, the configuration solution is based on the code developed by J.D. Shea et. al. [62][63].

3.3 Ill-posedness and Regularization

3.3.1 Ill-posed problems

Hadamard introduced the definition of mathematical term ill-posedness [66]. From $\mathbf{Ac} = \mathbf{b}$ of Equation (3.32), the inverse problem is to find $\mathbf{c}$ for a given data $\mathbf{b}$ and known matrix $\mathbf{A}$. The inverse problem is called well-posed (in the Hadamard sense), if

(a) A solution exists,

(b) The solution is unique, and

(c) The solution is stable and its behavior depends continuously on data $\mathbf{b}$.

The meaning of (a) is the solution $\mathbf{c}$ satisfy the equation. For (b), the solution $\mathbf{c}$ does not exist more than one in the space of bounded functions. Lastly, for (c), a tiny perturbation in the

data results small differences in the solution $\mathbf{c}$ [67]. Even if a problem is well-posed, it may still be ill-conditioned, implies that small changes in the data can cause arbitrarily large changes in the solution [68]. An ill-conditioned problem is indicated by a large condition number. The problem is called ill-posed otherwise than mentioned in (a) – (c). An ill-posed problem must be converted into a well-posed problem in order to be solved.

To find an approximate solution $\mathbf{c}$ of the Equation (3.32), the standard approach is based on linear least squares approach is used, as written in Equation (3.34). Linear least squares seeks to minimize the residual norm, which can written in Equation (3.35).

$$\mathrm{A}^T\mathrm{A}\,\mathrm{c} = \mathrm{A}^T\mathrm{b}$$

$$\mathrm{c} = [\mathrm{A}^T\mathrm{A}]^{-1}\mathrm{A}^T\mathrm{b} \tag{3.34}$$

$$\min_{c} \|Ac - b\|_2 \tag{3.35}$$

The linear model of the scattering system in Equation (3.35) is ill-posed problems, if both of the following criteria are satisfied:

(a) the singular values of A decay gradually to zero, and

(b) the ratio between the largest and the smallest nonzero singular values is large.

Criterion (a) implies that there is no "nearby" problem with a well-conditioned coefficient matrix and with well-determined numerical rank. Meanwhile (b) implies that the matrix A is ill-conditioned, i.e., the solution is potentially very sensitive to perturbations [69]. Ill-posed problem can cause the ordinary least squares estimation leads to an overdetermined (over-fitted) system of equations. It is also yields a highly undetermined (under-fitted) system without a unique solution if the number of unknowns in S is much greater than the number of measurements, such as $2MF \ll 2K$.

The image reconstruction problem in microwave tomography is a specific example of an inverse scattering problem that is typically ill-posed and nonlinear. It has been shown that the ill-

posedness of the inverse scattering problem varies with factors as follows [70][71]:

(1) Increasing the resolution of the reconstructed profile results in an increase in the number of unknowns and consequently an increase in the ill-posedness.

(2) The nonlinearity and ill-posedness of the inverse problem tends to increase as the number of frequency increases.

(3) The degree of the singularity is primarily depended on the data collection strategy, which includes the location of transmitting and receiving antennas.

(4) The *priori* information about the model is inconsistent with the objective function of model, thus leads to inherent non-uniqueness solution [55].

3.3.2 Regularization methods

For discrete ill-posed problems in Equation (3.35), they are essentially underdetermined due to the cluster of small singular values of A. Hence, it is necessary to incorporate further information about the desired solution in order to stabilize the problem and to single out a useful and stable solution. This is the purpose of regularization. The regularization aims at enforcing bounds or constraints on the reconstructed solution and, thus, to reduce the number of degrees of freedom in the solution.

Most commonly used regularization methods for a linear ill-posed problems are the truncated singular value decomposition (TSVD), and Tikhonov regularization. A common feature of these regularization methods is that they depend on some regularization parameter that gives a good balance, filtering out enough unnecessary data without losing too much information in the computed solution [68]. In this thesis, we examine two approaches for choosing the regularization parameter using:

(1) an empirical formula, and

(2) Tikhonov regularization based on L-curve method.

On point (1), as described in Section 3.2.1, a regularization parameter γ has been introduced in Equation (3.24) – (3.25), and calculated empirically based on Equation (3.26) – (3.27). In this section, we will elaborate on point (2).

3.3.3 L-curve method

In Equation (3.35), Tikhonov regularization method defines the regularized solution L_λ as the minimizer of the following weighted combination of the residual norm $\|\mathrm{Ac}-\mathrm{b}\|_2$ and the side constraint $\Omega(c) = \|\mathbf{I}\,(c-c^*)\|_2$.

$$\mathrm{L}_\lambda = \arg\min\{\|Ac-b\|_2^2 + \lambda^2\|\mathbf{I}\,(c-c^*)\|_2^2\} \tag{3.35}$$

Where the matrix $\mathbf{I}$ is typically the identity matrix, and c^* is an initial estimate of the solution. The regularization parameter λ controls the weight given to minimization of the side constraint $\Omega(c)$ relative to minimization of the residual norm. Clearly, a large λ favors a small solution seminorm at the cost of a large residual norm, whereas a small λ has the opposite effect. Therefore, it is important to choose an appropriate λ, which gives a good balance between the residual norm and the side constraint. A regularization method produces a regularized solution, c_{reg} [68][69][72].

In Tikhonov regularization, the L-curve method is proposed for choosing the regularization parameter. For all valid regularization parameters, L-curve is a parametric plot of the norm $\left\|\mathbf{I}\,c_{reg}\right\|_2$ of the regularized solutions versus the corresponding residual norm $\left\|Ac_{reg}-b\right\|_2$. The L-curve method consists of two procedures.

(1) Compute the curvature in log-log scale $\left(\log\left\|Ac_{reg}-b\right\|_2, \log\left\|\mathbf{I}\,c_{reg}\right\|_2\right)$

(2) Select the point with the maximum curvature.

Any regularized solution must lie on or above the Tikhonov L-curve. Hence, λ, corresponding to the L-curve's corner is chosen as the appropriate regularization parameter. The

L-curve almost always has a characteristic L-shaped appearance with a distinct corner when plotted in log-log scale, as shown in Figure 3.3.

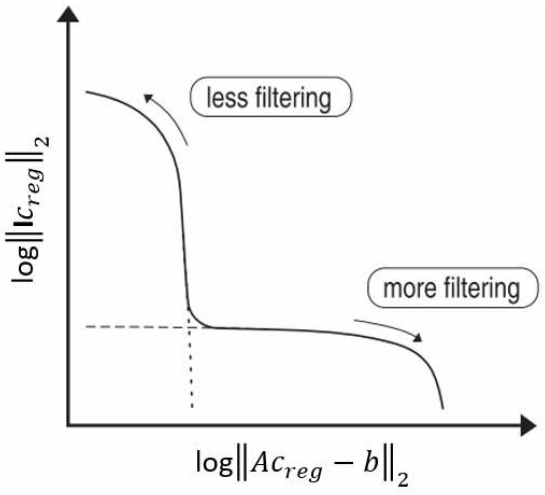

Figure 3.3 The generic form of the Tikhonov L-curve [69]

We utilized the REGULARIZATION TOOLS package of MATLAB to determine the regularization parameter λ. The routine l_curve produces a log-log plot of the L-curve and also locates the corner and identifies the corresponding regularization parameter. Given a discrete set of values of $\|Ac_{reg} - b\|_2$ and $\|\mathbf{I}\, c_{reg}\|_2$, routine plot_lc plots the corresponding L-curve, while routine l_corner locates the L- curve's corner [69].

3.4 Challenges in MWT

To make MWT a viable imaging method, its current achievable image quantitative accuracy and resolution need to be enhanced. Broadly speaking, two general approaches have been suggested to increase the image quantitative accuracy and resolution achievable from MWT.

(1) Increase the amounts of measurement data (i.e., obtain diverse observations data), and

(2) Interpret the collected scattering information in a better way.

Within the framework of these two approaches, several approaches as listed below are considered:

(1) increasing the number of antennas (or, probes) [73],

(2) using multiple-frequency data sets [74],

(3) simultaneous use of transverse magnetic and electric data sets (polarization) [75],

(4) using more effective inversion algorithms and regularization techniques [76].

Here, we will elaborate only a few techniques from mentioned above. The amount of observation data can be increased by increasing the number of antennas. However, the antennas must be arranged at a certain distance from each other because of the wavelength. Thus, the scale of the apparatus increases and the computational cost becomes substantial. Furthermore, the signal-noise ratio (SNR) is degraded by this method, which increases the measurement error, thus creates difficulties in the accurate image reconstruction.

Until now single frequency is most widely used, but a method using multi-frequencies has been proposed [63][74][77]. It is known that the lower frequencies are used to enable the imaging of large structures and high-contrast objects, and used as the initial guess for the proceeding iterations. Meanwhile higher frequencies are used to improve the resolution with the reconstruction from the lower frequency. The idea is that a combination will improve the reconstruction. However, as explained in Section 2.2.2, biological tissues is a medium with frequency dependence of the complex permittivity. Its dispersion behavior is modeled using a single-pole Debye model with parameters of $\varepsilon_\infty, \Delta\varepsilon,$ and σ_s in Equation (2.2). In this method, the number of unknown parameters is increased along with the number of frequencies; thus, the approach becomes difficult.

Lastly, the multi-polarization method has been examined as a means to obtain a variety of observations data [73][75][78][79]. Polarization is a unique aspect of MWI which is not usually

available in most other imaging modalities, which can be exploited as a source of information. This issue is the main interest in the thesis and will further discussed in next section.

3.5 Polarization Diversity

In this thesis, we investigate the impact of different antenna orientations (i.e., polarizations) on the quality of the measured data, and finally on the image reconstruction. The changes in the polarization of the scattered waves are influenced by the composition and shape of the biological tissue.

Figure 3.4 shows the developed breast imaging arrays designed for microwave inverse scattering by other researchers, which are the vertically oriented monopole antennas and horizontally oriented monopoles. In Figure 3.4(a), the data acquisition platform consists of 16 monopole antennas organized in a circular fashion, which positioned vertically to allow free vertical motion over the full tank span. The first clinical 3-D microwave tomographic images of breast were presented [80]. In Figure 3.4(b), the microwave imaging system contains 32 antennas which is oriented horizontally and positioned in in a cylindrical setup. A reasonable agreement in the shape and position of a simple object is obtained [40].

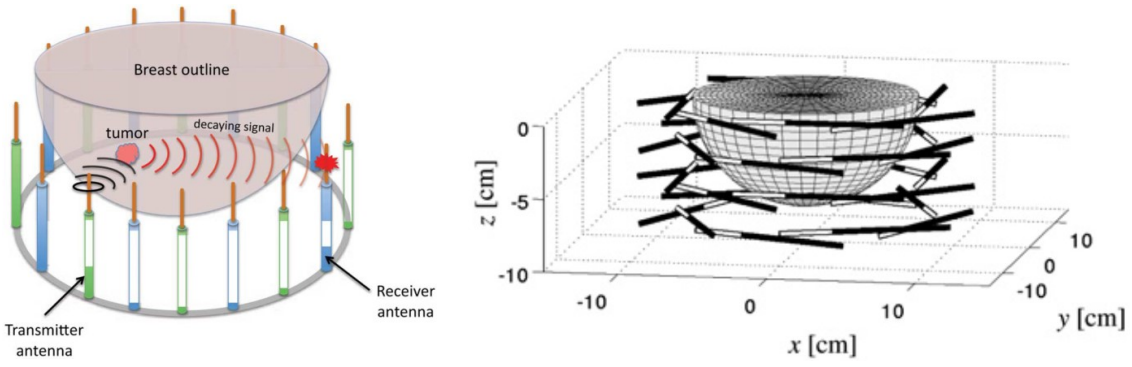

(a) vertical oriented [80], (b) horizontal oriented [40].

Figure 3.4 Schematic 3-D representation of data acquisition platform

While many techniques have been leveraged toward a microwave imaging solution, they are all fundamentally dependent on the quality of the scattering data. By sourcing and observing the field components corresponding to the polarizations of interest, the effect of the polarization on the information content of the scattering data can be studied. Therefore, a variety of polarization arrangements have been proposed for use in microwave imaging systems. For example, a truncated singular-value decomposition (TSVD) analysis on the vertical and horizontal polarization of source and receive antennas performance has been compared [81]. The fidelity performance of both polarizations is similar, but vertical polarization configuration showed a slight improvement over noise than horizontal polarization.

As mentioned in Section 3.4, in order to achieve accurate image reconstruction, the number of antennas can be increased to obtain various information content of the scattering data. However, the measurement error increases if the SNR decreases; thus, it cannot reconstruct the image accurately. Therefore, it is necessary to minimize the analysis region in order to reduce the computational cost and the ill-posedness of inverse problems. For this reason, the implementation of a compact sensor that involves a small distance between the antenna and the breast is preferred to obtain coverage in the entire imaging domain. Consequently, a large number of antennas must be arranged in a small and limited space. To overcome this, various observation data can be obtained even in a small space by changing the plane of polarization.

The use of TE and TM polarization in the near-field region within the same system has been proposed, as shown in Figure 3.5 [73]. In the imaging system, modulated scatterer technique (MST) was used to measure the scattered field from the probe array to provide a high data acquisition rate of electromagnetic field distribution. Another experimental results for 3-D imaging of simple objects with a dual-polarized array were also reported [75]. However, the frequency used is relatively high, and there are some issues regarding the imaging quality presented.

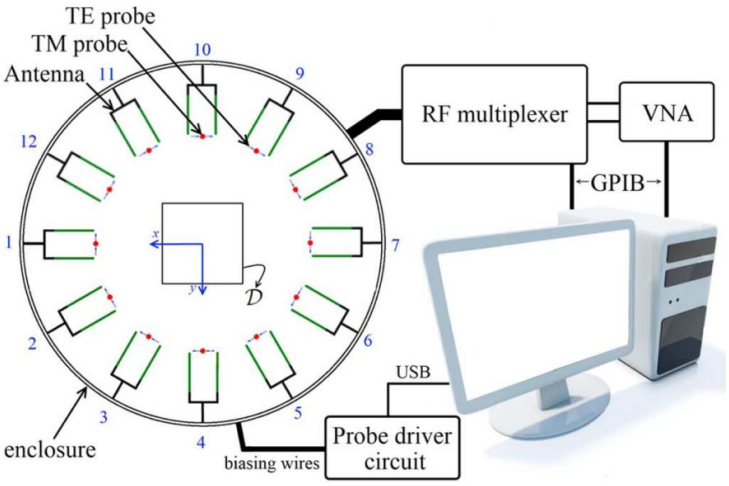

Figure 3.5 Schematic representation of the dual-polarized imaging system [73]

The impact of multi-polarization on image reconstruction was investigated with a shielded array of patch antennas using TSVD analysis [78], as the continuation of research in [81]. Based on the proposed patch antenna array of multiband, miniaturized patch antennas in [79], a multi-polarization layout was investigated in addition to uniform array configurations, as shown in Figure 3.6. The results of TSVD analysis show that the multi-polarization configuration with a higher truncation index performs better than vertical and horizontal polarizations. Although the reconstructed profiles demonstrated no significant differences between these polarizations, this indicate that polarization diversity may be introduced as one of the significant design consideration.

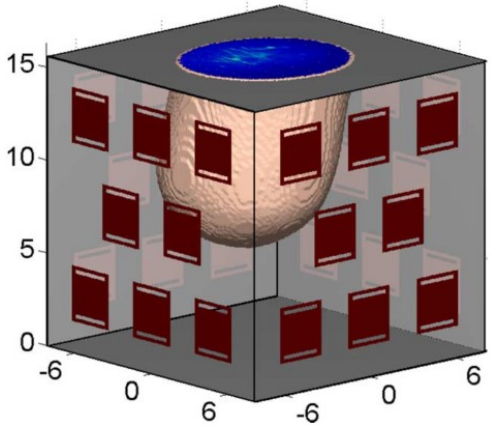

Width: 18 cm

Height: 15 cm

Length: 18 cm

(a) Proposed enclosed array [79]

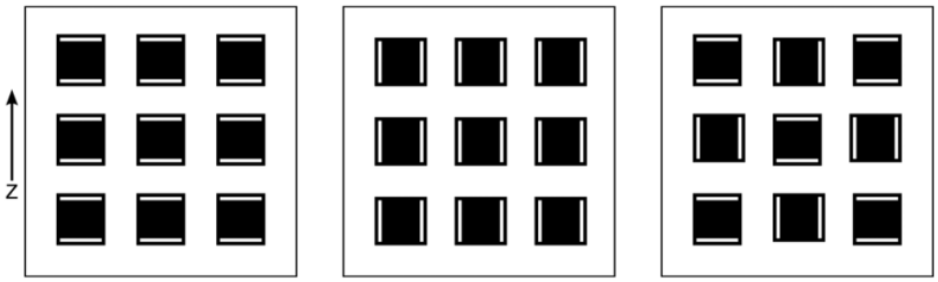

(b) Three configurations of the one side panel (vertical, horizontal, multi polarization) [78]

Figure 3.6 Illustration of a 32-element array proposed by Hagness et. al.

From above, the effectiveness of employing multi-polarization in radar-based approach to reconstruct images using TSVD analysis have been reported. However, to our knowledge, there has been no prior investigation on the physical considerations related to antenna arrangement in order to achieve sufficient image reconstruction. This information can be used as a viable parameter in antenna array design. In this thesis, in addition to the effect of the polarization, the effect of the correlation of coefficient in image reconstruction were studied. The proposed configuration array utilizing multi-polarization is explained in Chapter 4.

CHAPTER 4

PROPOSED MICROWAVE TOMOGRAPHY SYSTEM

4.1 Overview

In this thesis, we present a compact-sized imaging sensor using the multi-polarization method for breast cancer detection. This chapter explains the proposed configuration algorithm, antenna array configuration, and breast models to realize the 3-D microwave breast imaging.

4.2 Proposed Configuration

4.2.1 Imaging Algorithm

In this thesis, the algorithm is configured through different input files according to Figure 4.1. The transmitter-receiver (transceiver) configuration file introduce the positions in space of the transceivers and how many transceivers is used. The geometry file specifying the object region, the number of cells, size and the complex permittivity of the background medium. In the initial permittivity file, the initial guess of the objects complex permittivity C_0 is specified. The last input file is the measured scattered field E^s_{meas} obtained from the forward problem, which contains the expected scattered field for the optimization process. Finally, the reconstructed image C_n is stored in the reconstructed permittivity file.

MoM is used to obtain the scattering field measurement in the forward problem. Whereas in the inverse problem, Newton-Kantorovich method or DBIM is implemented to reconstruct the object under investigation. For choosing the regularization parameter, we used: (1) an empirical formula, and (2) L-curve method. The transmitter-receiver configuration file and geometry configuration file will be discussed in next section.

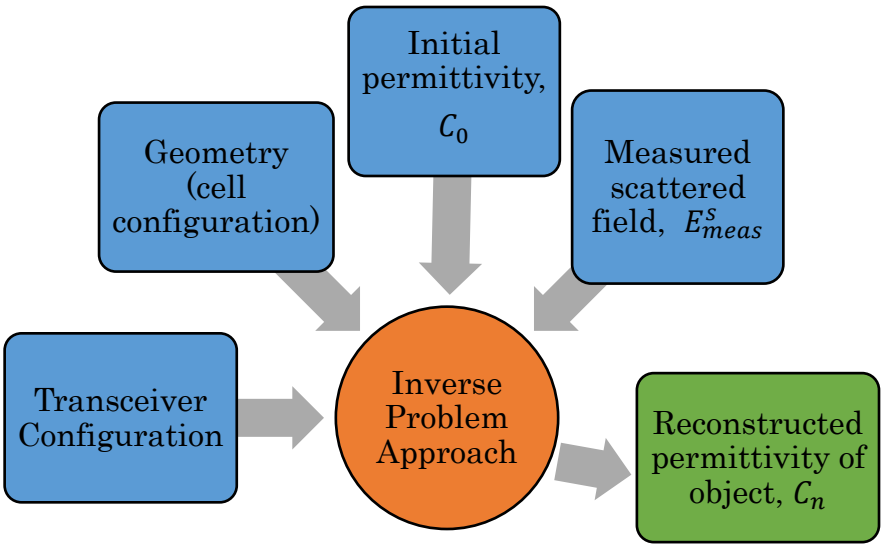

Figure 4.1 The input and output interface of the configuration algorithm

4.2.2 Imaging System Development

The proposed microwave tomography system is mainly based on the microwave mammography system developed by Kuwahara et. al., as shown in Figure 4.2(a). The equipment features an imaging sensor, an antenna switch for changing the combination of the transmitting and receiving antenna, and a 2-port vector network analyzer (VNA) as a transceiver. It also comprises of a PC to control the VNA and the antenna switch, and obtain the measurement data, and a workstation (WS) for measurement data processing. The antenna system is designed assuming that, during the examination, the patient lies prone a top a measuring tank with one breast pendant in the imaging antenna array. As shown in Figure 4.2(b), the small size of breast imaging sensor is equipped with an aspirator on top for pressure suction. Hereby, the breast is fixed to the inner shape of a sensor, thus, the shape of the breast for the imaging process is known. [13].

As mentioned in Section 3.5, if the distance between the imaging breast and the antenna array is large, the propagation loss increased. Thus, the measurement error increased as a result of reduced SNR. This condition will gives difficulties to detect changes in the breast accurately.

For this reason, it is necessary to design a compact sensor that involves a small distance between the antenna and the breast.

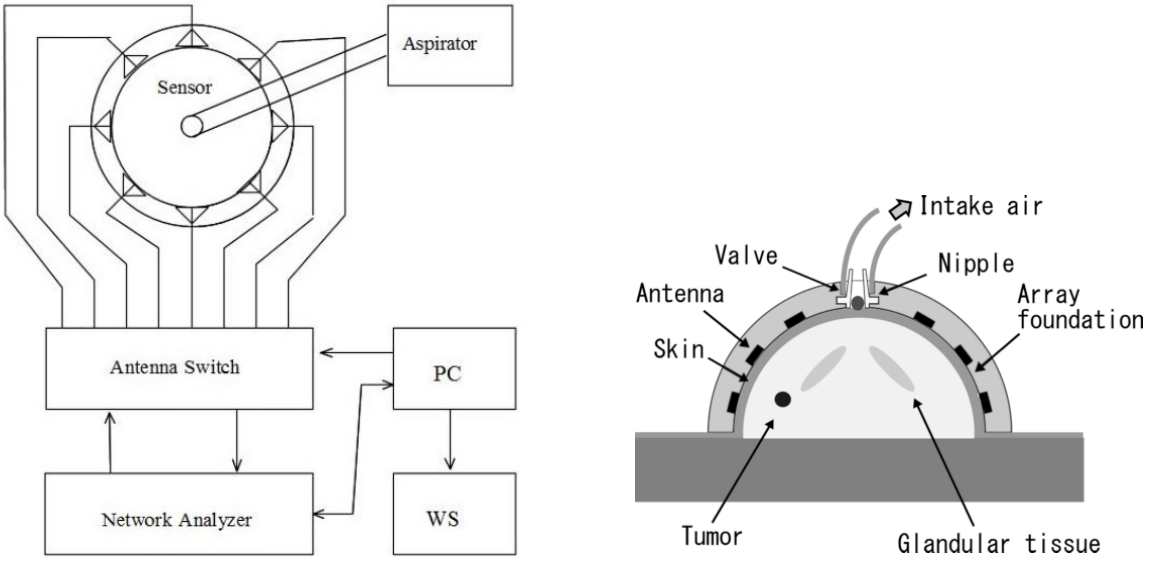

(a) Schematic diagram [13], (b) Sensor with aspirator [18]

Figure 4.2 Microwave mammography development by Kuwahara et. al.

In this thesis, the development on the imaging sensor will be focused. For our microwave tomography system, the breast imaging sensor is modified based on Figure 4.2(b). The prototype breast imaging sensor is shown in Figure 4.3. A number of antennas are embedded in a rectangular resin block which provides a hemispherical space to accommodate patient's breast. In order to maintain the hemispherical volume of imaging breast, an aspirator connected to a suction valve is equipped on the lower surface of resin block. The material constant of the resin block is approximately similar to those of the adipose tissue. Moreover, due to the close contact between the breast and the sensor, a lossy matching fluid becomes unnecessary to reduce the influence of surrounding structures.

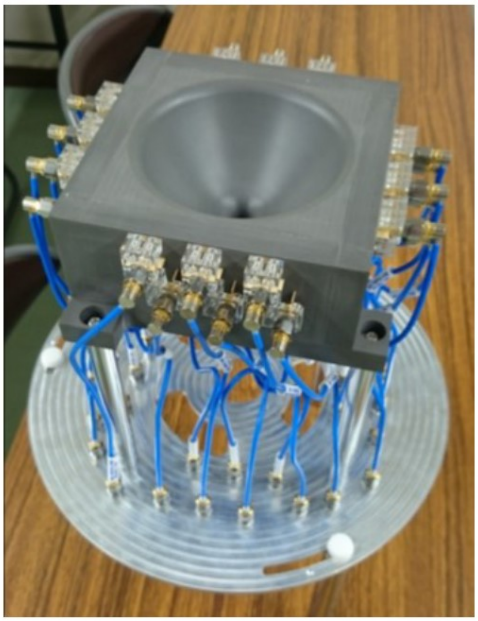

Width: 96 mm

Height: 48 mm

Length: 96 mm

Figure 4.3 Prototype breast imaging sensor [82]

4.3 Breast Imaging Sensor

Based on Figure 4.3, an enclosed array with dimensions width 96 × length 96 × height 48 mm is proposed in Figure 4.4. The size of our configuration is more compact than suggested by Burfeindt et. al. which has dimensions width 18 × length 18 × height 15 cm, as shown in Figure 3.6(a) [79]. For our investigation, 32 antennas and 36 antennas are chosen. This is based on a trade-off between maximizing the amount of measurements available for the imaging algorithm, and the limited space which is available for the measurement units and antennas in the imaging system.

4.3.1 32-elements antenna

The antennas are arranged in a 4 × 2 configuration on each of the four side-panels of the sensor. Figure 4.4(a) shows the position of the antenna. One of the antennas is used for transmitting, and all the elements including transmitter are used for receiving data. In this thesis, we investigated three different antenna arrangements to show the impact of polarizations on 3-D image reconstruction. The lines in Figure 4.4 represent the polarization direction of the antenna, where

the y-axis indicates vertical polarization, and the x- or z-axis horizontal polarization. The antenna arrangements for each side are identical, and the four side-panels are parallel to either the xy- or zy-plane.

Figure 4.4(a) illustrates the vertical polarization, Figure 4.4(b) the horizontal polarization, and Figure 4.4(c) a mix of vertical and horizontal polarization (hereafter referred to as multi-polarization). The vertical configuration in Figure 4.4(a) has 32 vertical polarized antennas, as all antennas are polarized in the y-direction. The horizontal configuration in Figure 4.4(b) has 16 x-polarized antennas and 16 z-polarized antennas. Whereas the multi-polarized configuration has 8 x-polarized, 8 z-polarized, and 16 y-polarized antennas. Furthermore, we avoid arranging antennas on the top surface of the panel to clearly show the effect of polarization.

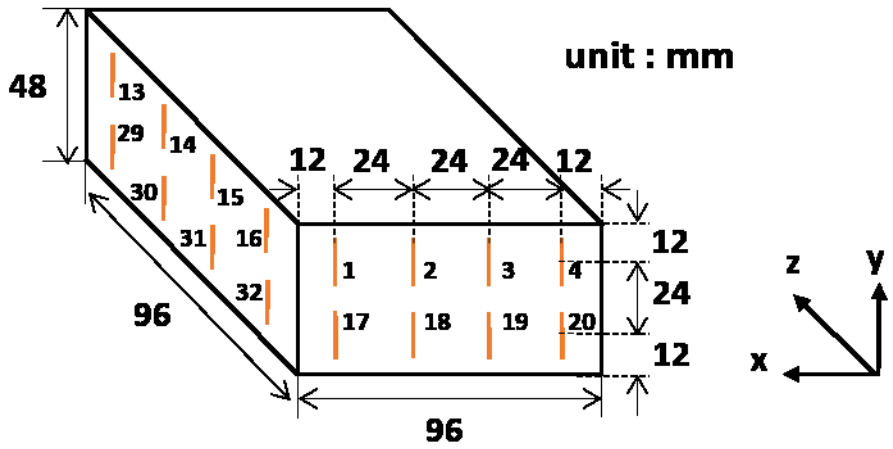

(a) Vertical polarization (VP)

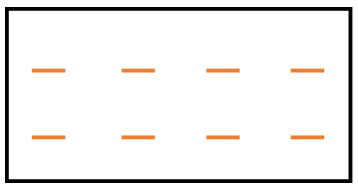

(b) Horizontal polarization (HP)

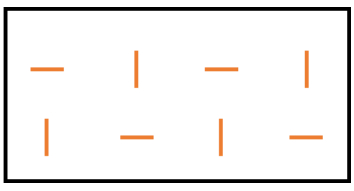

(c) Multi-polarization (MP)

Figure 4.4 Proposed imaging sensor with three polarizations in 32-elements [50]

4.3.2 36-elements antenna

The effectiveness of applying multi-polarization to transmit and receive antennas have been confirmed in [50], [51]. As a continuity from 32-elements antenna in Section 4.3.1, we use more antennas and different antenna layouts on the side panels. In addition, we also arranged antennas on the top surface of the enclosed array.

We assumed two imaging sensors consists of 36 antennas installed on the rectangular box. The antennas are arranged in a 3 × 2 configuration on each of the four side-panels, and 12 antennas on top surface of the sensor. The antenna arrangements for each of the four side-panels are identical. Figure 4.5 shows the position of the antenna. Similar with Figure 4.4, one of the antennas is used for transmitting, and all the elements including transmitter are used for receiving data. The lines in Figure 4.5 shows the polarization direction of the antenna, where the y-axis indicates vertical polarization. The configuration shown in Figure 4.5(a), the antennas are organized to generate single polarization which has 24 y-polarized, and 12 z-polarized antennas. Whereas, the configuration shown in Figure 4.5(b), the antennas are arranged to generate multi-polarization which has 12 x-polarized, 12 z-polarized, and 12 y-polarized antennas.

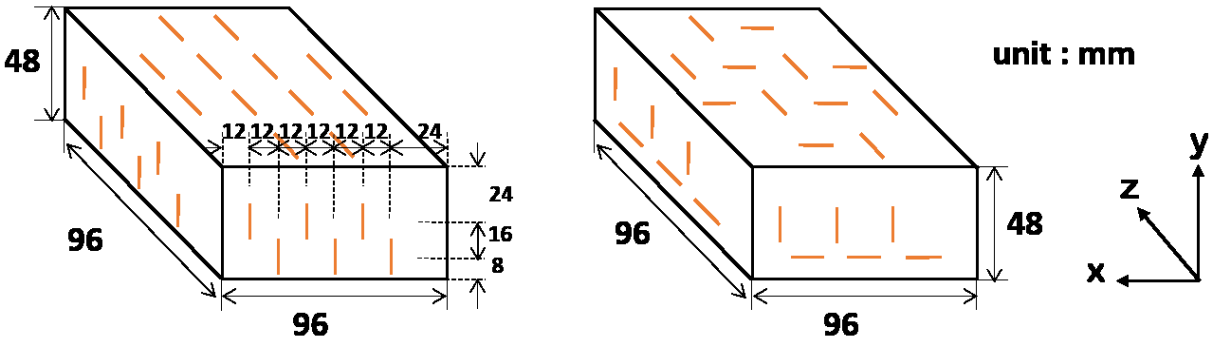

(a) Single polarization (b) Multi-polarization

Figure 4.5 Proposed imaging sensor with multi-polarizations in 36-elements [83]

Comparing the performance of the layouts shown in Figure 4.4(a) – (b), we addresses the question of whether uniform vertical or uniform horizontal polarization yields better performance. Meanwhile, evaluating the performance of the layout shown in Figure 4.4(c) and Figure 4.5 further addresses the question of whether employing diversity polarizations is a viable strategy for accurate image reconstruction, as mentioned in Section 3.5. The proposed antenna array configurations are summarized in Table 4.1.

Table 4.1 Proposed antenna array configurations

Array ID	No. of antennas		Polarization		
	32	36	VP*	HP*	MP*
32VP	✔		✔		
32HP	✔			✔	
32MP	✔				✔
36SP*		✔	✔	✔	
36MP		✔			✔

✔: the considered elements

*VP = Vertical polarization, HP = Horizontal polarization, MP = Multi polarization

*SP = Single polarization

4.1 Breast Model

This section discusses the design of the breast model based on tissue-mimicking method. The breast is modeled by a hemisphere with radius of 4.8 cm. Here, the breast can be simplified in an approximation model. It can be modelled as skin, adipose tissue, fibro glandular tissue, cancer, and chest wall. Several parameters are used to indicate the dielectric properties of each tissues. For the sake of simplicity, the following assumptions have been made:

(1) The thickness and the complex permittivity of skin is assumed as known parameters and not considered in simulations.

(2) The mathematical complexity of the Cole-Cole model in Equation (2.3) is avoided due to large number of unknowns and high computational cost. This led us to investigate simple models of tissue structures using Equation (2.1), which has two unknown parameters, ε_r and σ.

Suppose the inhomogeneous medium with a finite volume S is embedded in homogeneous background medium with relative permittivity ε_r^b and conductivity σ^b. Let assume a time dependence $\exp(-j\omega t)$, the complex permittivity $\varepsilon^*(r)$ at a point $r(x,y,z)$ of S is denoted by $\varepsilon^*(r) = \sigma(r) + j\omega\varepsilon_0\varepsilon_r(r)$. The contrast function χ at a point r is defined by Equation (4.1)

$$\chi = (\sigma - \sigma^b) + j\omega\varepsilon_0(\varepsilon_r - \varepsilon_r^b) \tag{4.1}$$

where ε_0 is the vacuum permittivity, and ω is the angular frequency. The conductivity σ and relative permittivity ε_r of the imaging object are the unknown parameters that will be measured.

As shown in Figure 4.6, the background medium is taken to be a rectangular solid and subdivided into K sub-squares (cells or voxels). Each cells of the background and inhomogeneous medium (object of interest) is characterized by relative permittivity ε_r and conductivity σ. Table 4.2 shows the average parameters of each tissue for our numerical analysis. The value of malignant tissue (cancer) is set higher than those of adipose tissues and slightly high than fibro glandular tissues. The high contrast between malignant and adipose tissues provides significant rationale for the advantages of microwave imaging in breast cancer detection.

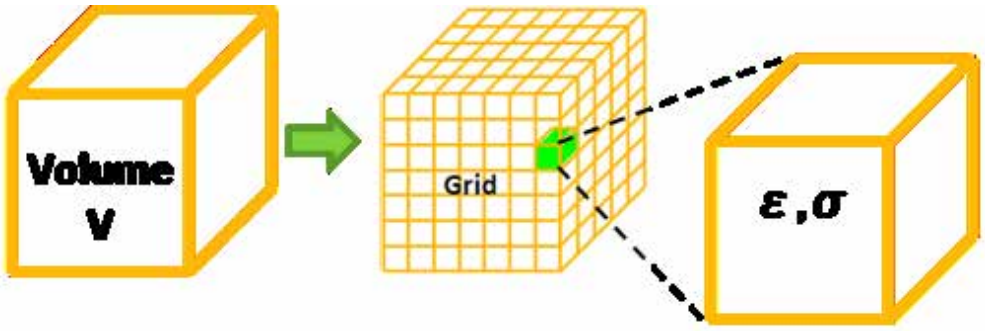

Figure 4.6 Discretized imaging area

Table 4.2 Dielectric properties of breast model

Parameter	Background	Chest wall	Adipose	Fibro glandular	Cancer
$\boldsymbol{\varepsilon_r}$	8.2	57	7	25 – 40	52
$\boldsymbol{\sigma}$ [S/m]	0.15	2	0.4	1.0 – 2.2	4

For the object of interest, we propose two simple breast models for investigation. The composition of our imaging object are as follows:

(1) Breast I:

Composed of the adipose tissue and cancer, based on the high contrast between these two tissues. A hemispherical distribution of fibro glandular tissue is also added. Here, the complex permittivity of fibro glandular is $\{\varepsilon_r, \sigma\} = \{35,\ 1.5\ [\mathrm{S/m}]\}$, and distributed uniformly. This represents a simple model of breast cancer.

(2) Breast II:

Chest wall is added which represents a complicated model of breast, and tissue-mimicking of real breast shown in Figure 2.1. Here, the fibro glandular distribution in Breast I is changed to randomly distributed, and its complex permittivity is characterized according to Table 4.2.

The above mentioned breast models are summarized in Table 4.3. Figure 4.7 shows the configuration of breast models. After the breast models discretized into K cubic cells, the dielectric properties are allocated to each cells, according to tissues type in Table 4.2. Here, the cancer accounts for one cell. Note that, the radius of cancer is 10 mm and 4 mm for 12-mm resolution and 8-mm resolution, respectively. The example of characterization of dielectric properties to each tissue for Breast II is shown in Figure 4.8.

Table 4.3 Breast models composition

Breast ID	Chest wall	Adipose	Fibro glandular	Cancer
Breast I		✔	✔ (H*)	✔
Breast II	✔	✔	✔ (R*)	✔

✔: the considered elements

*H: hemispherical, R: random distribution

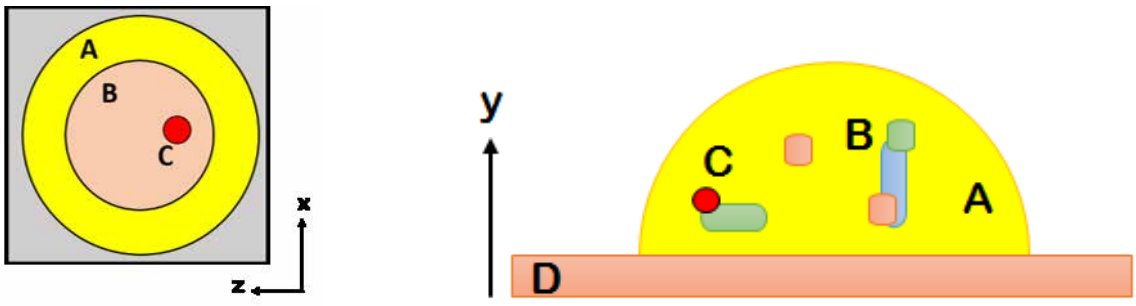

(a) Breast I (b) Breast II

A: Adipose tissue, **B**: Fibro glandular tissue, **C**: Cancer, **D**: Chest wall

Figure 4.7 Configuration of proposed breast model

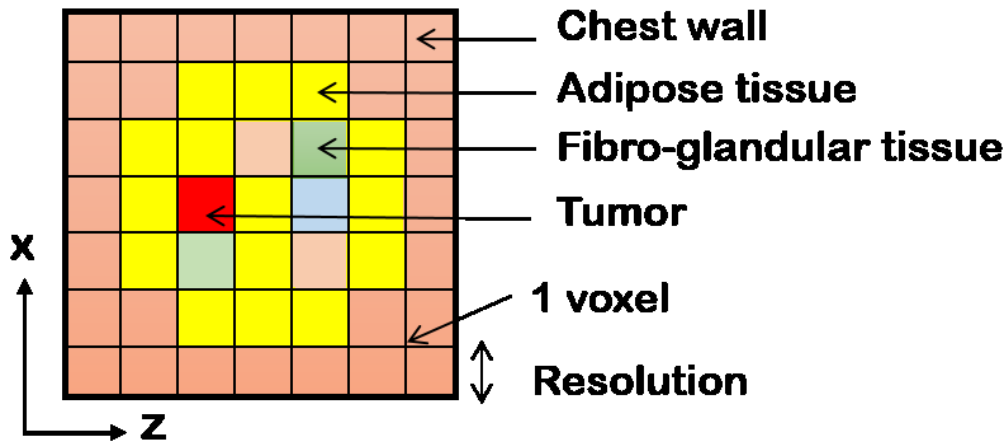

Figure 4.8 Allocation of dielectric properties into cells for Breast II

CHAPTER 5

NUMERICAL RESULTS & DISCUSSION

5.1 Overview

Numerical programs using MATLAB have been developed to investigate the impact of diversity polarizations and correlation coefficient on the complex permittivity reconstruction. Three type of polarizations are evaluated, which are vertical polarization (VP), horizontal polarization (HP), and multi-polarization (MP). The numerical simulations were done according to proposed array configurations and characterized breast model. The total field within the scattering object was calculated in the forward problem based on the Method of Moment (MoM), and the nonlinear relationship is solved with appropriate inverse problems approach. The results were divided based on two different inverse problem approaches, i.e., Newton-Kantorovich (NKT) and Distorted Born Iterative Method (DBIM).

5.2 Simulation Setup and Performance Metrics

In order to obtain accurate and high resolution of image reconstruction, the following assumptions have been made for all numerical simulations:

(1) For biomedical applications in MWI, only a single frequency of 2.5 GHz is used.

(2) Non-Debye model of Equation (2.1) is used. Therefore, only relative permittivity ε_r and conductivity σ are the physical quantities of interest.

(3) For simplicity, a point source is used for the transmitting antennas.

(4) The analysis region is limited only to the imaging breast, which is the background is not included, to reduce the number or unknowns.

(5) Apply a simple bound constraints to reduce the span of the solution space.

Along with above assumptions, the numerical simulations according to polarizations, inverse problem approaches, array configuration, and breast models are categorized in Table 5.1.

Table 5.1 Categorized numerical simulations

Configuration ID	Number of antennas	Breast ID*	Inverse Problem	
			NKT	DBIM
32NKT_Br.I	32	Br.I	✔	
32DBIM_Br.II	32	Br.II		✔
36DBIM_Br.II	36	Br.II		✔

✔: the considered elements

*: Br.I = Breast I, Br.II = Breast II

In all numerical simulations of Table 5.1, the performance considerations of quantitative comparisons between reconstructions for ε_r and σ are as follows:

(1) The 3-D image reconstruction,

(2) The dielectric property in 2-D distribution,

(3) The correlation of coefficient between adjacent antennas,

(4) The quality factor (or known as similarity or fidelity),

(5) The error measure based on the normalized root mean square (RMSE).

Performance in criterion (1) generates the quantitative images of breast model in 3-D distribution. Whereas the performance in criterion (2) shows the quantitative 2-D distribution with respect to cell number by vectorized the 3-D quantities.

Performance in criterion (3) is calculated to evaluate quantitatively the diversity of measurements data obtained by changing polarizations. The average correlation of coefficient between adjacent antennas, ρ is written in Equation (5.1). N is the total number of antennas and t is the current transmitting antenna. Here, it is necessary to remove the transmitting antenna and its pair to calculate the correlation of adjacent elements.

$$\rho = \frac{1}{N}\left|\sum_{t=1}^{N}\frac{\sum_{n=1,t\neq n}^{N/2} X_{t,2n-1}\, X_{t,2n}}{\sqrt{X_{t,2n-1}\, X_{t,2n-1}{}^{*}}\sqrt{X_{t,2n}\, X_{t,2n}{}^{*}}}\right| \tag{5.1}$$

Performance in criterion (4) is intended as a measure of the qualitative similarity between actual and estimated quantity. The two 3-D quantities to be compared are vectorized and the metric is calculated as the cosine of the angle between the vectors. Let ϕ be the angle between two quantities represented by vectors of q_1 (actual quantity) and q_2 (estimated quantity). The quality factor (QF) or fidelity measure is written in Equation (5.2). The ideal fidelity curve would have a peak of unity, corresponding to a perfect reconstruction.

$$\mathrm{QF} = \cos(\phi) = \frac{(q_1^T q_2)}{\|q_1\|_2 \|q_2\|_2} \tag{5.2}$$

Lastly, performance in criterion (5) is designed to represent the error relative to the actual dielectric properties of two parameter estimates with a single metric. The proposed error metric is given in Equation (5.3). K is the total number of voxels in volume V which also denotes the length of each parameter vector. The hat notation denotes an estimated quantity.

$$e_{rmse} = \frac{1}{\sqrt{K}}\left(\left\|\frac{\varepsilon_r - \widehat{\varepsilon_r}}{\varepsilon_r}\right\|_2 + \left\|\frac{\sigma - \hat{\sigma}}{\sigma}\right\|_2\right) \tag{5.3}$$

5.3 Newton-Kantorovich (NKT) approach

Here, we apply the Newton-Kantorovich (NKT) in the inverse scattering problem. The imaging region including the background are discretized to 405 cubic cells to obtain 12-mm resolution. In accordance with assumption criterion (4), the number of unknowns in the analysis region is 108 cells. We assumed the breast model is immersed in the background medium with complex permittivity of $\{\varepsilon_r, \sigma\}$ = {6.2, 0.15 [S/m]}. The complex permittivity for initial guess is $\{\varepsilon_r, \sigma\}$ = {7, 0 [S/m]}, and the value chosen is closer to those of adipose tissue. The iteration is terminated when the norm of residual error of scattering data reached 1×10^{-3} or when the iteration reached the maximum iteration number, which is 20 iterations.

5.3.1 32-elements antenna and Breast I (32NKT_Br.I)

The simulation results for Breast I and corresponding polarizations after 10 iterations are presented. Figure 5.1 shows the 3-D distribution images of the two unknown parameters. The relative permittivity ε_r and conductivity σ are on the left and right of each images. The actual model of Breast 1 is shown in Figure 5.1(a). The fibro glandular tissues are uniformly distributed within adipose tissue and its presence is indicated by yellow and cyan in relative permittivity and conductivity, respectively. The cancer accounts for one cell, and its existence is red and marked with an arrow.

Figure 5.1(b)-(d) show the results using vertical, horizontal, and multi-polarization, respectively, for transmitting and receiving data. From Figure 5.1(b), we could not reconstruct the imaging breast for both relative permittivity and conductivity using vertical polarization. Figure 5.1(c) gradually reconstruct the shape of fibro glandular tissue, but could not estimates the cancer in conductivity using horizontal polarization. In contrast, Figure 5.1(d) clearly reconstruct the imaging breast and indicates the cancer presence for both parameters using multi-polarization.

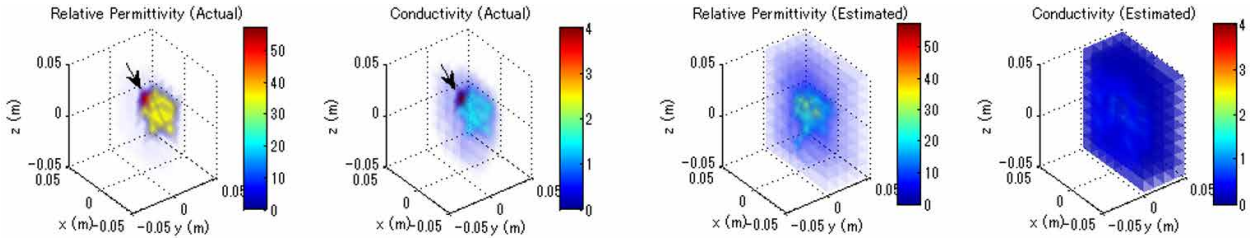

(a) Actual model (b) Vertical polarization

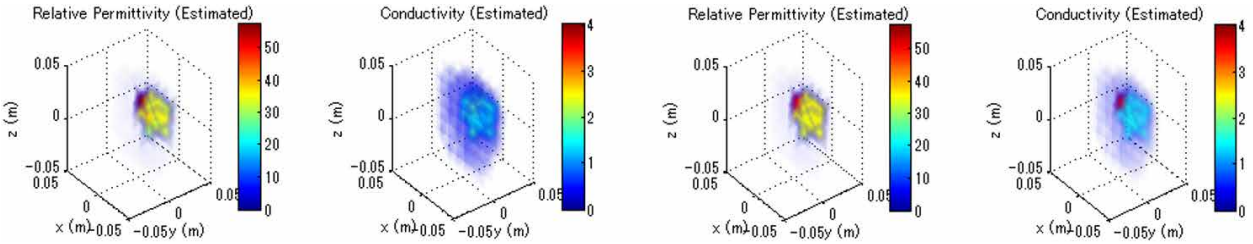

(c) Horizontal polarization (d) Multi-polarization

Figure 5.1 Actual and estimated 3-D image reconstructions for 32NKT_Br.I

Figure 5.2 shows the 2-D distribution of imaging region in the cross section which includes the cancer cell. The x-axis indicates the x-coordinate of the voxel and the y-axis indicates either the relative permittivity or conductivity. The actual value is shown by black dash line. The cancerous cell accounts for one cell and its actual value is $\{\varepsilon_r, \sigma\}$ = {52, 4 [S/m]}. The reconstructed parameters of the cancer for the different polarizations are as follows. Vertical polarization (VP): $\{\varepsilon_r, \sigma\}$ = {25.96, 1.05 [S/m]}, Horizontal polarization (HP): $\{\varepsilon_r, \sigma\}$ = {55.04, 1.52 [S/m]}, and multi-polarization (MP): $\{\varepsilon_r, \sigma\}$= {50.61, 3.53 [S/m]}. The fibro-glandular tissue is approximately reconstructed using horizontal and multi-polarization. Overall, we observed that the dielectric properties of the cancer are lower than the expected setting values when using uniform polarizations (vertical polarization and horizontal polarization). However, the dielectric properties of the cancer are improved and accurately estimated using multi-polarization.

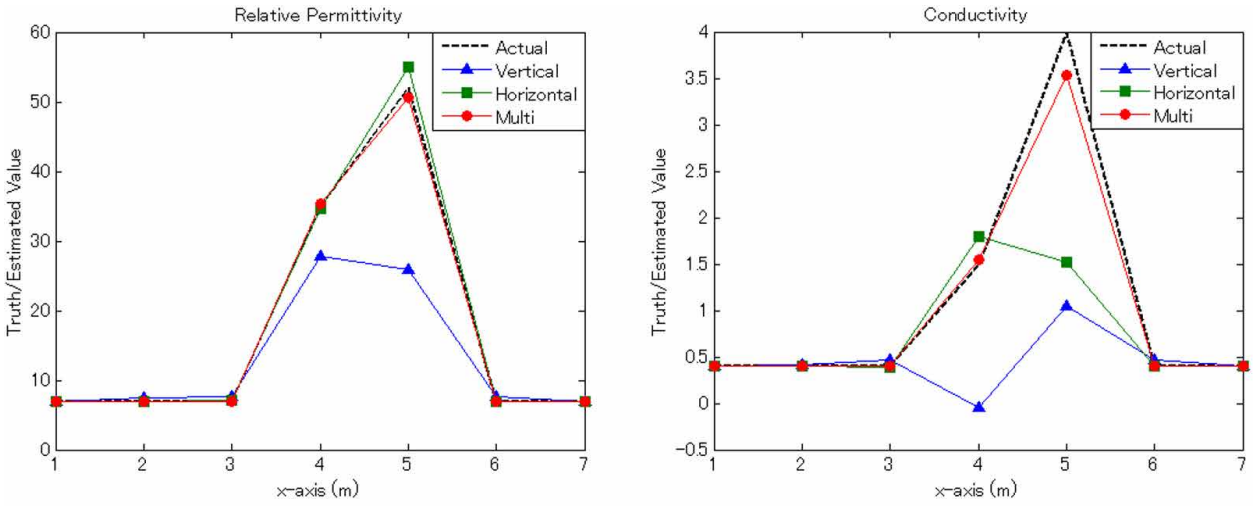

(a) Relative permittivity (b) Conductivity

Figure 5.2 Dielectric property distributions including the cancer voxel for 32NKT_Br.I

Next, the performance in criterion (3) is discussed. The average correlation of coefficient of adjacent antennas for all polarizations are given as {VP, HP, MP} = {0.9968, 0.9964, 0.1530}. Overall, the correlation coefficient was significantly reduced when using multi-polarization compared to uniform polarizations. An adequate image reconstruction was obtained using multi-polarization owing to the low correlation coefficient, as shown in Figure 5.1 – 5.2.

Figure 5.3(a) illustrates the quality factor are increasing significantly and towards unity when using horizontal and multi-polarization, whereas the quality factor for vertical polarizations is gradually increasing along with iteration number. At 10^{th} iteration, the quality factor reached 0.8415, 0.9797, 0.9993 when using vertical, horizontal, and multi-polarization, respectively. Meanwhile, in Figure 5.3(b), the RMSE for vertical polarization is gradually decreasing, and the RMSE for horizontal and multi-polarization perform similar behavior. However the RMSE for multi-polarization start to decrease drastically after 6^{th} iteration compared to uniform polarizations.

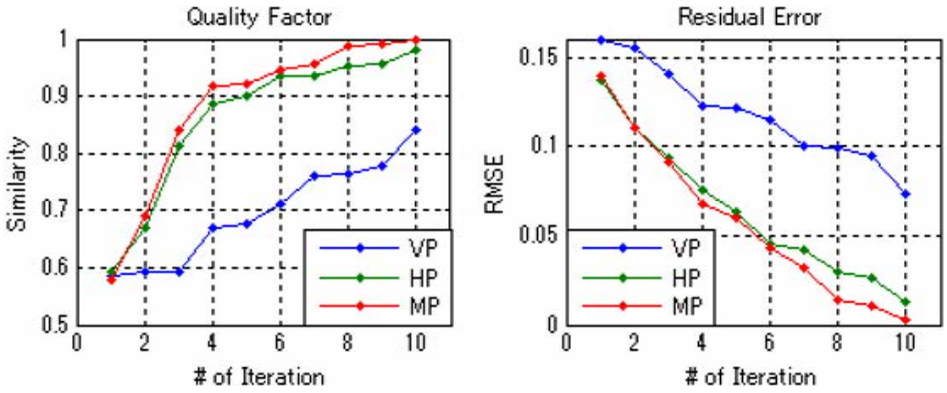

(a) Quality Factor (b) RMSE

Figure 5.3 Performance metrics for 32NKT_Br.I

Since, high resolution and sensitivity are required in microwave imaging system, the imaging resolution is increased to 8 mm. This can be done by discretizing the imaging region to 1183 cubic cells, where the number of unknowns in the analysis region is 369 voxels. Since configuration 32NKT_Br.I_MP in Figure 5.1(d) provide better results, this configuration is implemented to evaluate the 8-mm resolution imaging. Here, the maximum iteration number is set to 250 iterations.

Figures 5.4 shows the numerical results of the relative permittivity and conductivity in 8-mm resolution when using multi-polarization. In Figure 5.4(a), the fibro glandular tissue was reconstructed gradually over the adipose tissue region for relative permittivity and conductivity. After 250th iteration, the image reconstruction for both parameters were unsuccessful. Meanwhile, the dielectric property distribution of analysis region is shown in Figure 5.4(b). The x-axis indicates the voxel number, and the y-axis indicates the actual and estimated value for either relative permittivity or conductivity. The actual value is defined by red solid line, whereas the reconstructed parameters are marked with blue dot. The cancerous cell accounts for one cell. We observed that the estimated dielectric properties in analysis region, particularly for fibro-glandular tissues, are scattered than the expected setting values, regardless using multi-polarization. Thus,

the imaging method using NKT in 8-mm resolution can be considered ineffective and require further improvements.

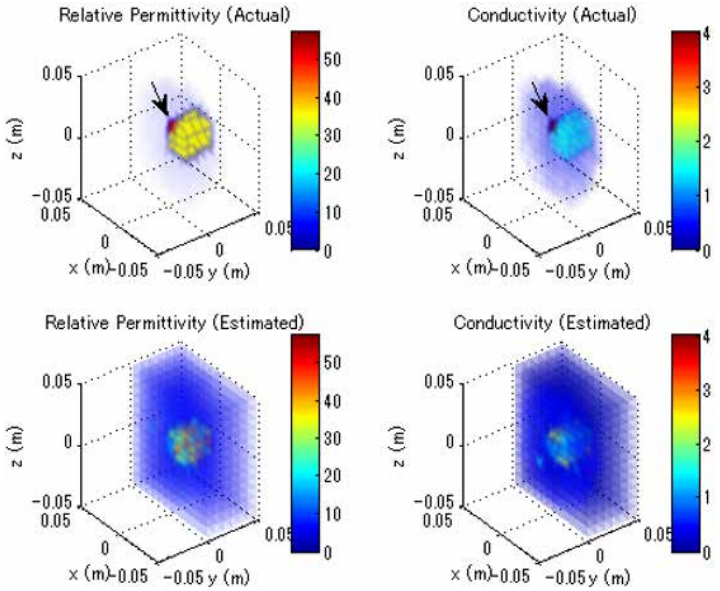

(a) 3-D image reconstruction

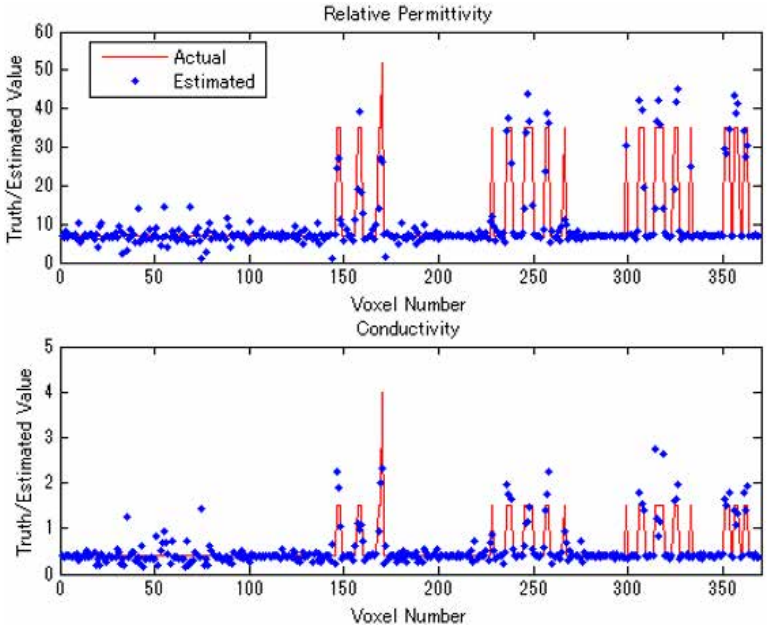

(b) Dielectric property distribution

Figure 5.4 Results using multi-polarization in 8-mm resolution for 32NKT_Br.I

5.3.2 Discussion on 32NKT_Br.I

The non-linear inverse scattering problems are solved by Newton-Kantorovich (NKT) approach using least square method, as written in Equation (3.25). The Jacobian J is full rank, therefore all of the vectors in the Jacobian matrix are linearly independent. The inverse matrix is an ill-conditioned situation. The regularization parameter γ was determined empirically to decrease the condition number in 12-mm resolution imaging. For multi-polarization, the quality factor is close to unity, and the iterative algorithm stopped at 10^{th} iteration, due to the termination criterion (1×10^{-3}), as shown in Figure 5.5. These performances indicate that a small number of iterations is suffice for accurate image reconstruction when using multi-polarization. Therefore, the results shown in Figure 5.1 – 5.3 were based on 10^{th} iteration for reasonable comparison between different polarizations.

Moreover, low correlation coefficient due to multi-polarization leads to sufficient image reconstruction in Figure 5.1(d). This performance metric can be considered as a suitable parameter in determining antenna configuration. However, further investigation is needed to relate the correlation coefficient with image reconstruction, regarding the configuration of horizontal polarization.

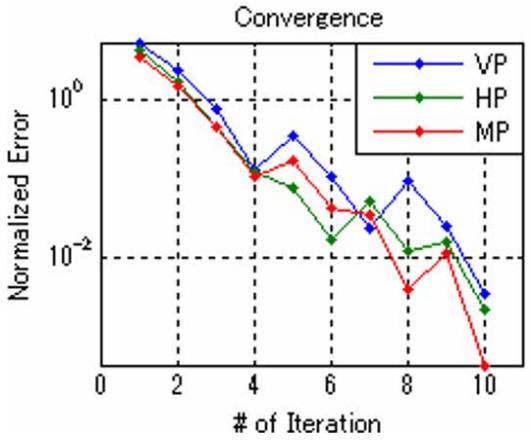

Figure 5.5 Convergence between different polarizations for 32NKT_Br.I

The NKT method creates difficulties in dielectric properties reconstruction despite multi-polarization configuration, such as low resolution and high computational cost. As shown in Figure 5.4, this method failed to reconstruct the analysis region with 8-mm resolution, regardless using multi-polarization, and neither empirical method nor L-curve method in regularization. It also involves high computational cost, because of the extensive calculations of the inverse matrix performed to compute the Jacobian in higher resolution. Figure 5.6 displays the computation of Jacobian calculation using NKT approach in MATLAB code, where D : Jacobian matrix, N : total number of unknowns in the analysis region, NR : number of transmitting antennas, T : estimated contrast in N, G : the Green's function between cells in the analysis region, KB : the Green's Function between transmitting antenna and the analysis region, and Ec : calculated total field. The inverse matrix calculation, inSG, for the computation of Jacobian matrix is performed at each iteration, thus increase the computation cost, especially for higher resolution. In 8-mm resolution imaging, 22 seconds are taken for one iteration, and 1 hour 36 minutes are taken for 250 iterations (CPU Intel® Core™ i3-4130 @ 3.40 GHz, RAM 4.00 GB). The calculation cost was considerably large. Therefore, an alternative approach for inverse problem is required to overcome these limitations.

```
inSG = (eye(3*N)-T*G)^-1;
D = [];
    for l=1:NR
        D = [D; KB*inSG*diag(Ec(3*N*(l-1)+1:3*N*l))];
    end
```

Figure 5.6 Jacobian calculation in NKT approach

5.4 Distorted Born Iterative Method (DBIM) approach

As an alternative to NKT method in Section 5.3, we employ the Distorted Born Iterative Method (DBIM) in the inverse scattering problem. Similarly, we discretized the imaging region to 1183 cubic cells to obtain 8-mm resolution. Here, the Breast II will be evaluated. The number of unknowns including the chest wall is 538 voxels. The dielectric properties of background medium for the relative permittivity and conductivity is $\{\varepsilon_r, \sigma\}$ = {8.2, 0.15 [S/m]}, meanwhile the initial guess is $\{\varepsilon_r, \sigma\}$ = {9, 0 [S/m]}.

5.4.1 32-elements antenna and Breast II

The impact of polarizations using 32-elements antenna is examined. Besides that, we also investigate the responses at different antenna positions than those in Figure 4.4(a). This is to show the impact on physical measurements using the analysis of the correlation coefficient of the received data on the image reconstruction.

Figure 5.7(a) is the actual model of Breast II and the cancer is marked by an arrow for clarity. Here, 10% of the volume ratio of breast model is occupied by fibro-glandular tissues that are distributed randomly within the adipose tissue. The existence of chest wall is omitted to clearly show the contrast between tissues in breast model. Figure 5.7(b)-(d) show the results of the 3-D reconstructed images after 250 iterations, using vertical, horizontal, and multi- polarization, respectively. As shown in Figure 5.7(b), the shape of fibro glandular tissue is gradually reconstructed but insufficient, when vertical polarization antennas are used. Meanwhile, the image reconstruction cannot be performed correctly neither for fibro glandular tissue nor cancer when using horizontal polarization in Figure 5.7(c). However, the results in Figure 5.7(d) indicate that the image reconstruction of the breast model is adequate when using multi-polarization antennas for transmitting and receiving. The fibro glandular tissues were approximately reconstructed and the cancer presence is distinct for relative permittivity and conductivity.

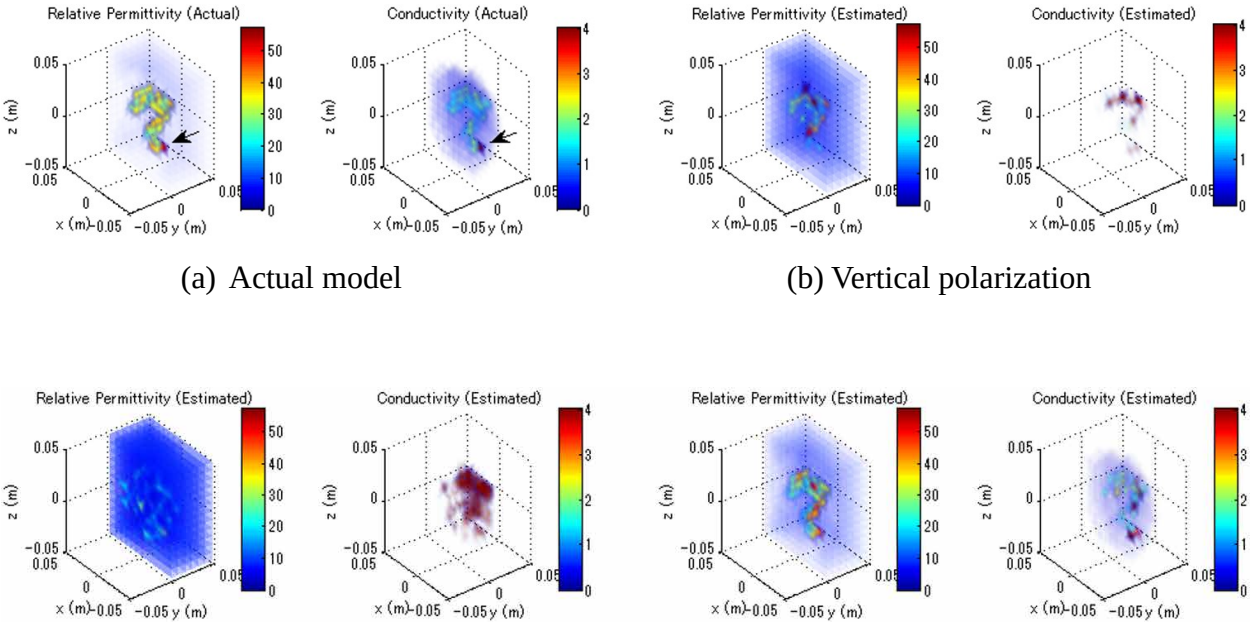

(a) Actual model (b) Vertical polarization

(c) Horizontal polarization (d) Multi-polarization

Figure 5.7 Actual and estimated 3-D image reconstructions for 32DBIM_Br.II

Figures 5.8 shows the setting and reconstruction values of the dielectric properties of the cancer voxel in the x-axis direction. The reconstructed parameters of the cancer for the different polarizations are as follows. Figure 5.8(a) demonstrates that the relative permittivity of the cancer and the fibro-glandular tissue are low when using vertical and horizontal polarization. Nevertheless, the reconstruction value obtained using multi-polarization is approaching to the actual value for both tissues. Meanwhile, the conductivity of the cancer and fibro-glandular tissue are improved and estimated approximately when using multi-polarization, whereas other polarizations perform reverse results. Table 5.2 shows the reconstructed relative permittivity and conductivity values of the cancer when using different polarizations. For multi-polarization, the reconstructed percentage was -14.29% and -14% for relative permittivity and conductivity, respectively. Overall, the results indicate that vertical and horizontal polarization provide different information of the image reconstruction and dielectric properties. The multi-polarization array configuration consistently performed better than uniform polarizations.

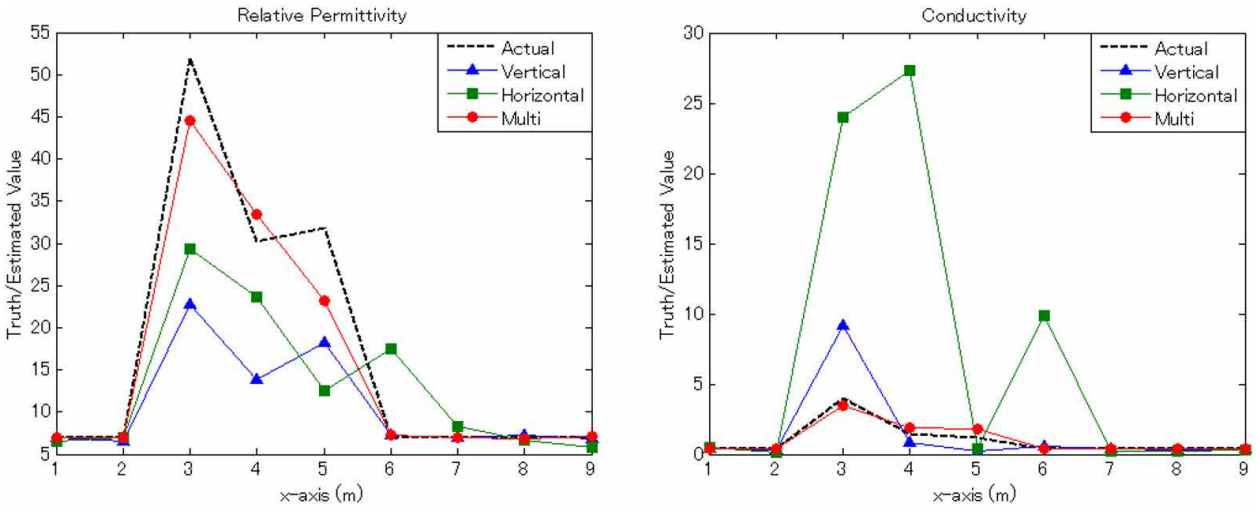

(a) Relative permittivity (b) Conductivity

Figure 5.8 Dielectric property distributions in the cross section including the cancer voxel for 32DBIM_Br.II

Table 5.2 Reconstructed values of cancer in different polarizations for 32DBIM_Br.II

Parameter	Actual value	Vertical Pola.*	Horizontal Pola.	Multi-Pola.
$\boldsymbol{\varepsilon_r}$	52	22.8	29.35	44.57
$\boldsymbol{\sigma}$ $[\boldsymbol{S/m}]$	4	9.18	23.98	3.44

*Pola.: Polarization

In addition, we investigated the impact on image reconstruction by the analysis of the correlation coefficient of the received data between adjacent antennas in our imaging sensor. Different antenna positions in y-axis with different polarizations were also considered. First, we examined the positions of the antennas shown in Figure 4.4(a), with the upper antenna at 36 mm and the lower antenna at 12 mm (Position 1). Table 5.3 summarizes the correlation coefficients for different polarizations and positions. At Position 1, we observed that uniform polarizations achieve

correlation coefficient close to 1 and the correlation coefficient of the multi-polarization is 0.1459, which is significantly low compared to the uniform polarizations. Next, we changed the position of the upper antenna to 24 mm and lower antenna to 8 mm (Position 2). For Position 3, 32 mm and 16 mm are assigned for the upper and lower antenna, respectively. The results for Position 2 and Position 3 are tabulated in Table 5.3. We observed that the results for both positions show a similar trend to that exhibited at Position 1.

Overall, the correlation coefficient of the receiver pair was significantly reduced when using multi-polarization compared to uniform polarizations. At Position 1, the high correlation coefficient when using vertical and horizontal polarizations associate that the image reconstruction and the reconstructed values of dielectric properties were unseccessful. Meanwhile, an adequate image reconstruction was obtained using multi- polarization because of the low correlation coefficient, as shown in Figures 5.7 – 5.8.

Table 5.3 The correlation coefficient between different positions of the antennas for 32DBIM_Br.II

Position	Position of antenna (upper, lower) mm	Vertical Polarization	Horizontal Polarization	Multi Polarization
1	36, 12	0.8029	0.7381	0.1459
2	24, 8	0.9461	0.9080	0.1506
3	32, 16	0.9210	0.8530	0.1998

Moreover, the correlation coefficient of the multi-polarization at Position 3 is slightly higher than that at Position 1. Figure 5.9 shows the x-axis projection of the actual and reconstruction values of the dielectric properties including the cancer voxel obtained using multi-polarization at different positions. These results demonstrate that positions with low correlation

coefficients reconstruct the dielectric properties sufficiently. Therefore, we can conclude that a low correlation coefficient is a viable specification for successful image reconstruction.

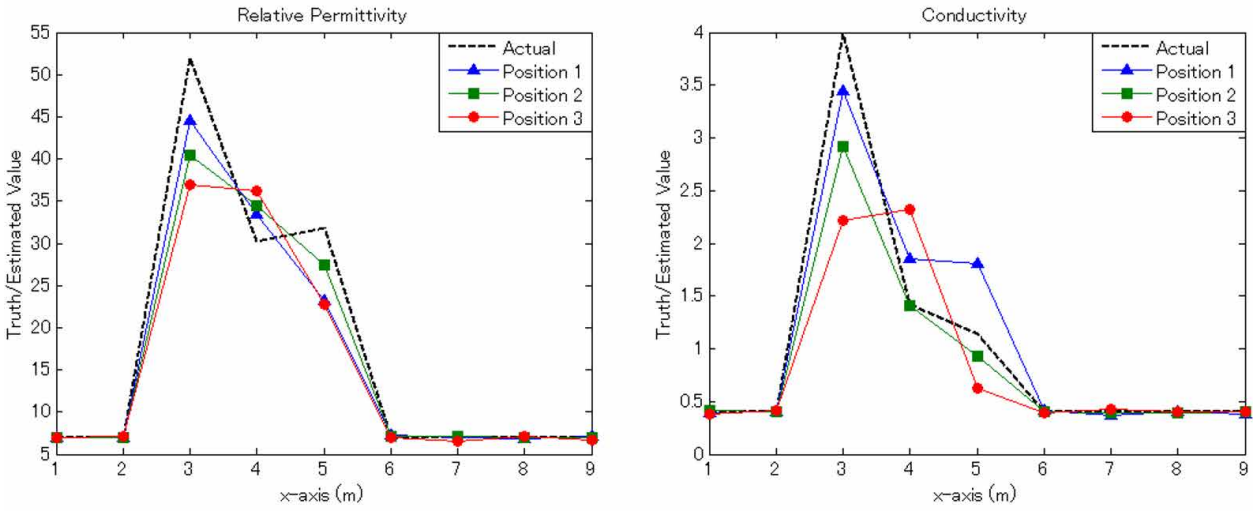

(a) Relative permittivity (b) Conductivity

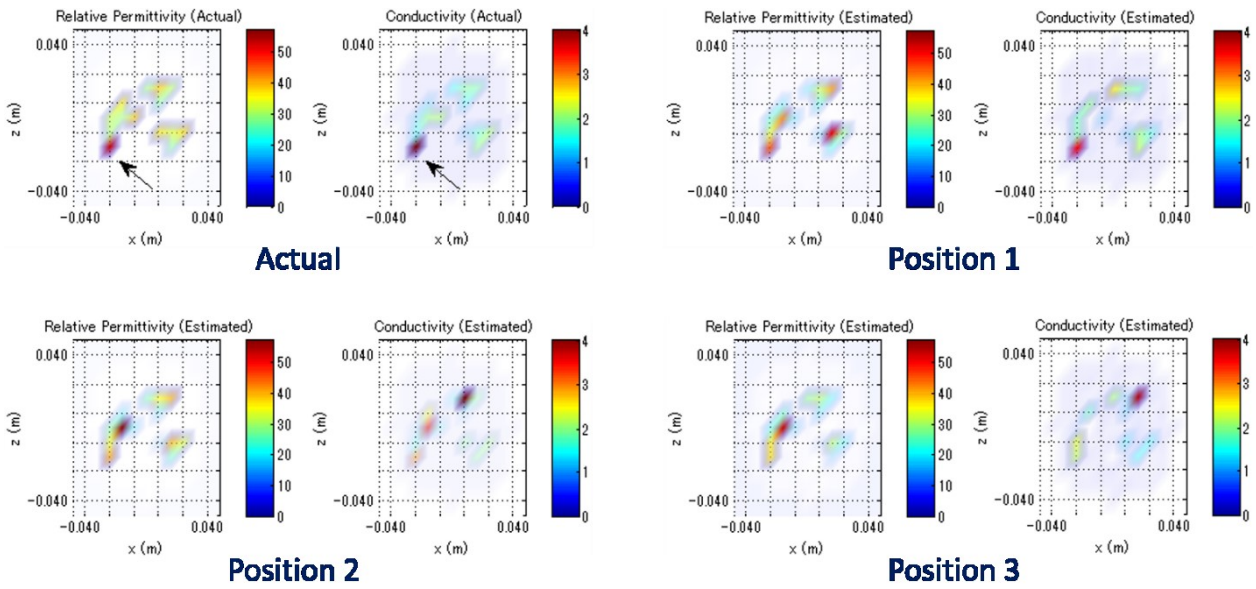

(c) Reconstructed dielectric properties at cross section view

Figure 5.9 Dielectric property distributions between different positions of the antenna

The performance metrics for 100 iterations are shown in Figure 5.10. The dielectric properties of chest wall is assumed known at the initial guess, and its property varies iteratively. The chest wall occupies 169 voxels (31.4%) of 538 voxels in the analysis region, hence the initial value of quality factor for all polarizations is 0.9672, as shown in Figure 5.10(a). In Figure 5.10(a), the quality factor for multi-polarization is moving towards unity, meanwhile the quality factor for vertical and horizontal polarizations are decreasing with increasing iteration number. At 250^{th} iteration, the quality factor for all polarizations are given as {VP, HP, MP} = {0.6932, 0.6179, 0.9687}. In Figure 5.10(b), the RMSE for vertical and horizontal polarization are increasing, whereas the RMSE for multi-polarizations are decreasing along with iteration number. Thus, the image reconstruction using uniform polarization were poor compared with multi-polarization, as shown in Figure 5.7, particularly for horizontal polarization in Figure 5.7(c).

Overall, the results from Figure 5.7 – 5.10 indicate that the vertical and horizontal array configurations perform different outcomes from each other, and vertical polarization gives slightly better results than those with horizontal polarization. The array configuration with multi-polarization which gives low correlation coefficient performs well than uniform polarizations to determine the image reconstruction and the dielectric property distributions of a simple breast model. Furthermore, in Breast II, the cancer is adjacent to fibro-glandular tissues and the contrast difference between the tissues is small. The findings confirm that we can detect the cancer accurately with the presence of fibro-glandular tissues by employing multi-polarization.

These results demonstrate that polarization diversity with low correlation coefficient do not degrade information quality compared to uniform polarization configurations and may represent a viable parameter for image reconstruction in microwave tomography aimed at breast cancer detection.

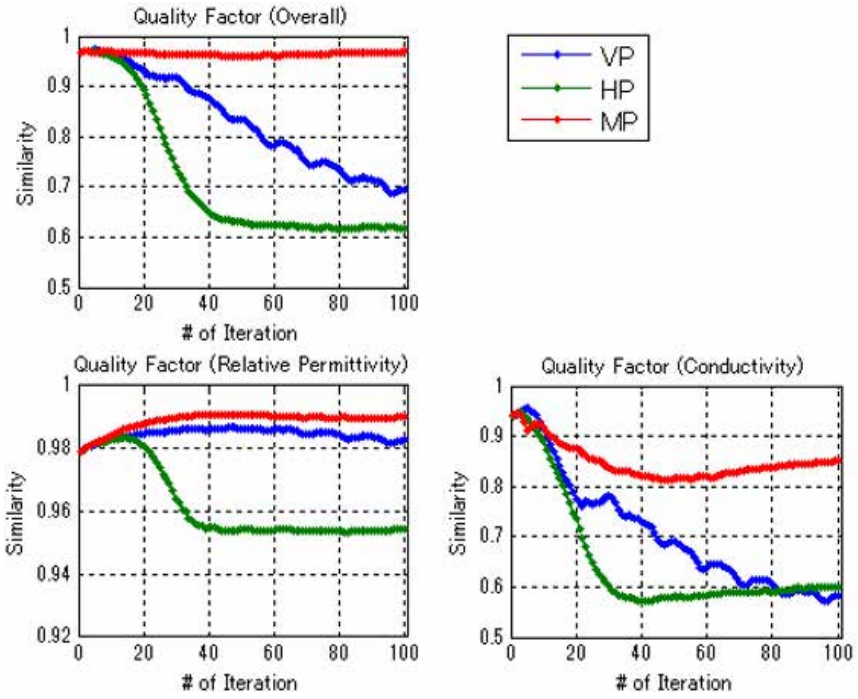

(a) Quality factor

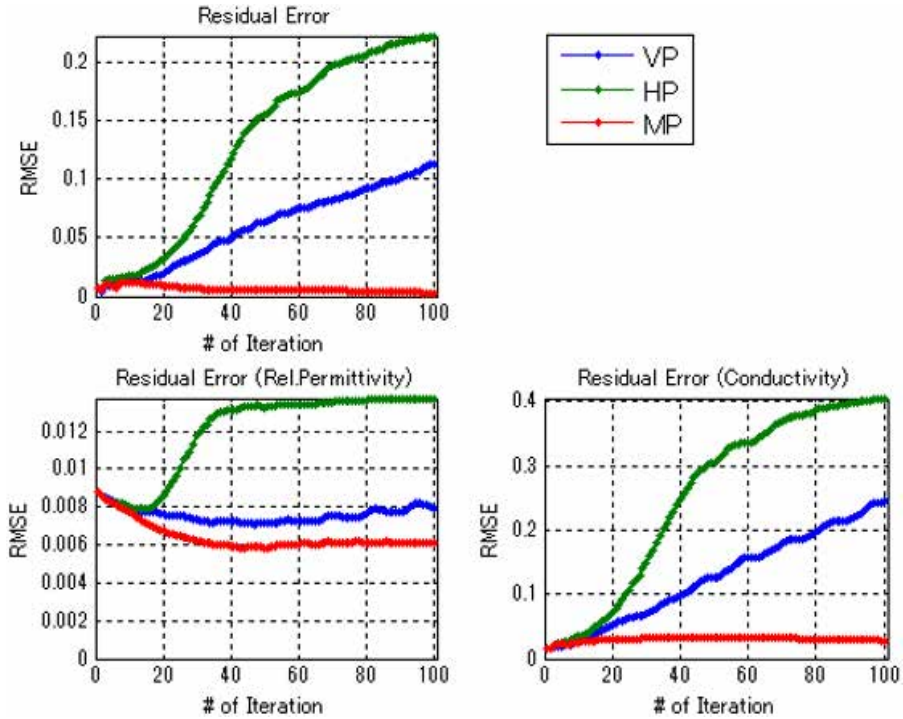

(b) RMSE

Figure 5.10 Performance metrics for 32DBIM_Br.II

5.4.2 Discussion on 32DBIM_Br.II

In a situation of larger objects with large contrast to the background medium, a non-linear method is needed. Here, the Distorted Born Iterative Method (DBIM) is implemented where it uses Born approximation to linearize the non-linear relation of Equation (3.29) at each iteration. In the Born approximation, the unknown total field within the actual permittivity in the analysis region E^t is approximated by the background medium field, E^b, that is, the total field of estimated permittivity distribution. In other words, E^b replace E^t in Equation (3.29). DBIM method begins with an initial guess for the background permittivity that may include any available a *priori* information about the object permittivity. In this case, the initial guess was chosen to be close to those of adipose tissues.

In contrast to NKT approach in Figure 5.6, DBIM does not require inverse matrix calculation for the computation of the Jacobian matrix D. Figure 5.11 shows the implementation of Jacobian calculation using DBIM approach in MATLAB code, where D : Jacobian matrix, N : total number of unknowns, NR : number of transmitting antenna, Ec : calculated total field, and KB : the Green Function's between transmitting antenna and the analysis region.

```
D = []; dPH = [];
    for I = 1:NR
        Eb = Ec(3*N*(I-1)+1:3*N*I).';
        Eb = Eb(ones(1,NR),:);
        KE = KB.*Eb;
        Ke = KE(:,1:N)+KE(:,N+1:2*N)+KE(:,2*N+1:3*N);
        Aa = [real(Ke) real(j*w*eo*Ke); imag(Ke) imag(j*w*eo*Ke)];
        D = [D; aa];
    end
```

Figure 5.11 Jacobian calculation in DBIM approach

In 8-mm resolution imaging, 16 seconds are taken for one iteration, and 24 minutes are taken for 250 iterations (CPU Intel® Core™ i3-4130 @ 3.40 GHz, RAM 4.00 GB). This step can reduce about 57 minutes (59.9%) of computation time significantly for 8-mm resolution imaging, compared to NKT method.

In order to solve the system of linear equations, the contrast perturbations or solution can be determined by Gauss-Newton method (empirical method) or Tikhonov method. The regularization parameter in first method can be determined by empirically according to the convergence of the process, as shown in Equation (3.25) – (3.27). Whereas, in latter method, the regularization parameter and solution can be obtained by L-curve method, as explained in Section 3.3.3. Therefore, to choose an appropriate regularization parameter in every iteration of DBIM is difficult. Even though the multi-polarization configuration is used, the results using these methods were insufficient, particularly in conductivity, as shown in Figure 5.12 – 5.13. In Figure 5.13, the actual value is defined by red solid line, whereas the estimated value is defined by blue asterisk. The dielectric property distribution of chest wall are scattered. Still, we observed that the L-curve method perform better reconstruction compared to empirical method.

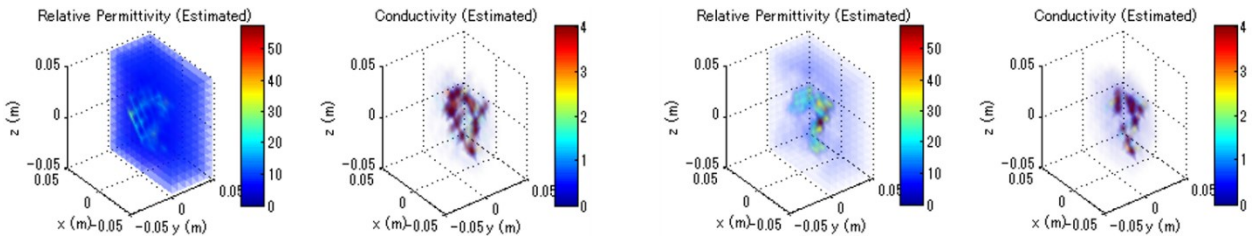

(a) Empirical method (b) L-curve method

Figure 5.12 3-D distribution using two solving techniques for 32DBIM_Br.II

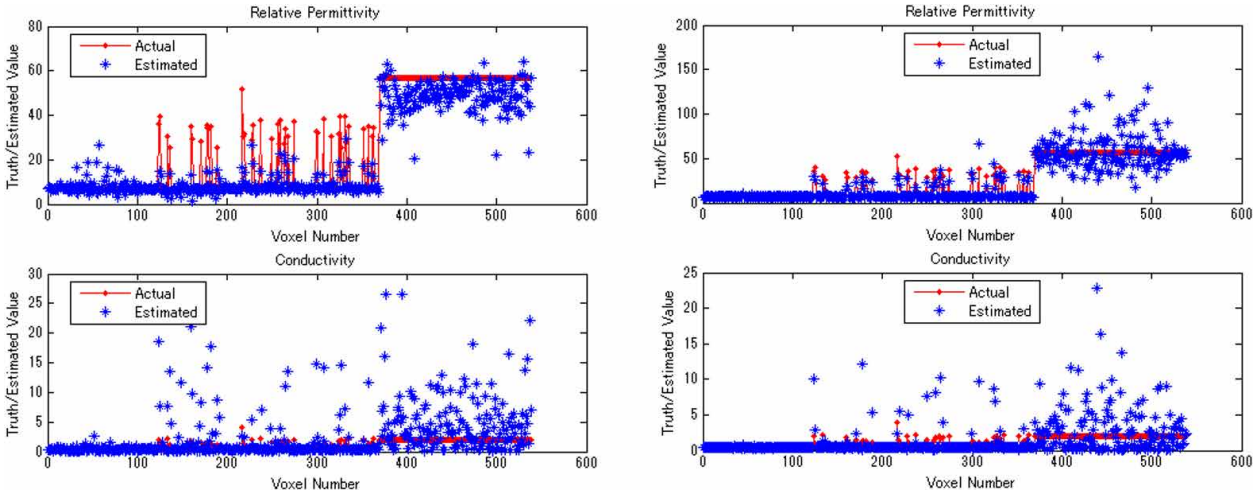

(a) Empirical method (b) L-curve method

Figure 5.13 Dielectric property distribution using two solving techniques for 32DBIM_Br.II

Therefore, another technique to solve the system of linear equations was implemented using Bi-Conjugate Gradient Stabilized Method (Bi-CGSTAB) algorithm [84]. This algorithm is rather stable, converge smoother and produces more accurate solutions. The algorithm of the pre-conditioned with Bi-CGSTAB method for solving linear equations $Ax = b$ is explained in Appendix C. The preconditioning is referred to as diagonal scaling.

We utilized the bicgstab command of MATLAB at the requested tolerance and number of iterations to solve the system of linear equations. For a linear equation of $Ax = b$, the unknown x is determined by $x = \text{bicgstab}(A, b, \text{tol}, \text{maxit})$, where tol and maxit specifies the tolerance of the method and the maximum number of iterations, respectively. Here, we assumed that the regularization parameter determined by empirical method is empirically good.

Figure 5.14 shows the implementation of Bi-CGSTAB method in MATLAB code, where D : Jacobian matrix, N : total number of unknowns, g : a regularization parameter determined by empirical method, dPH : difference between measured and calculated scattered field, and ds :

solutions or contrast perturbations (i.e., x). From Figure 5.15, we observed that Bi-CGSTAB performs better result than those in Figure 5.13.

```
Q = D'*D+g*eye(2*N);
DD = diag(Q);
DD = DD.^-1;
DD = diag(DD);
Qt = DD*Q;
c = D'*dPH;
ct = DD*c;
ds = bicgstab(Qt,ct,1e-3,1000);
```

Figure 5.14 Contrast perturbations determined by Bi-CGSTAB method

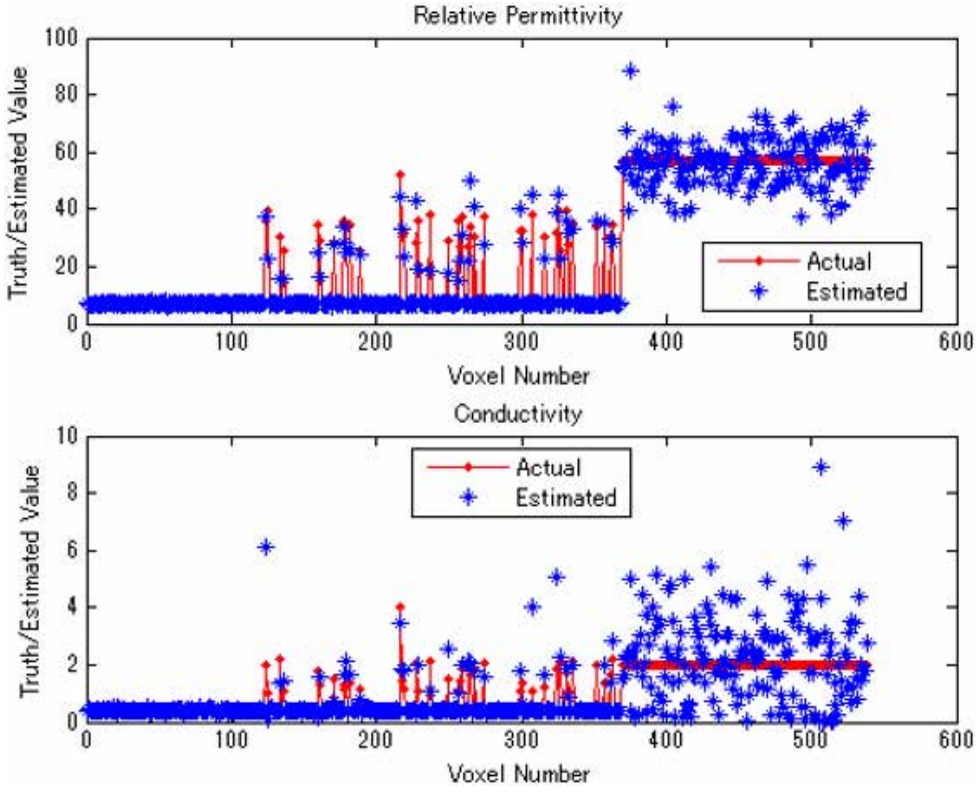

Figure 5.15 Dielectric property distribution using Bi-CGSTAB for 32DBIM_Br.II

The comparison on performance metrics for 100 iterations using three solving techniques of nonsymmetrical linear systems is shown in Figure 5.16. We observed that the quality factor performance of Bi-CGSTAB is superior to empirical and L-curve method. Similarly, the RMSE of Bi-CGSTAB is gradually decreasing along with iteration number. Moreover, we can see that the normalized error of Bi-CGSTAB converges faster, and its convergence behavior was much smoother towards iteration number compared to other two methods. The numerical results using Bi-CGSTAB method were shown in Figure 5.7 – 5.10, and 5.15.

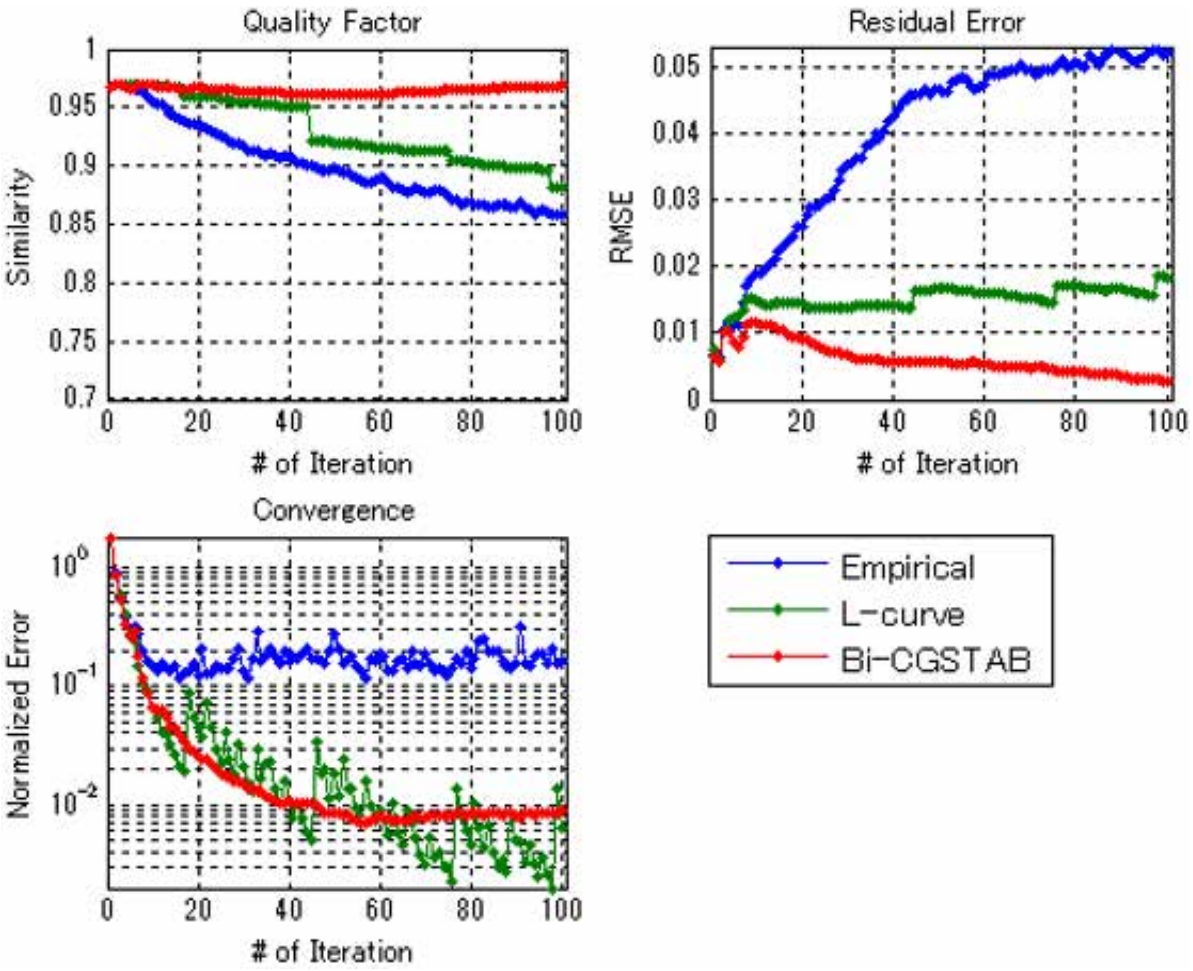

Figure 5.16 Performance metrics between three solving techniques for 32DBIM_Br.II

5.4.3 36-elements antenna and Breast II

From Section 5.4.1 and 5.4.2, the effectiveness of multi-polarization to transmit and receive antennas in image reconstruction are confirmed. Hence, we proposed 36-elements of array configuration as illustrated in Figure 4.5, which is completely utilize the multi-polarization approach in Figure 4.5(b). Here, the input setting of simulation and other assumptions are in the same way as implemented in Section 5.4.1 and 5.4.2.

Figure 5.17 shows the 3-D distribution of image reconstruction for single polarization and multi-polarization. Here, the region of chest wall is shown, and the cancer presence is marked with an arrow. From Figure 5.17(b), the fibro glandular tissue were reconstructed successfully for both parameters, but we could not estimate the cancer for conductivity. In contrast, Figure 5.17(c) gradually reconstruct and estimates the cancer for both parameters using multi-polarization.

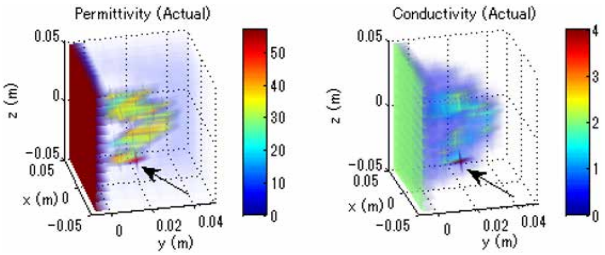

(a) Actual model

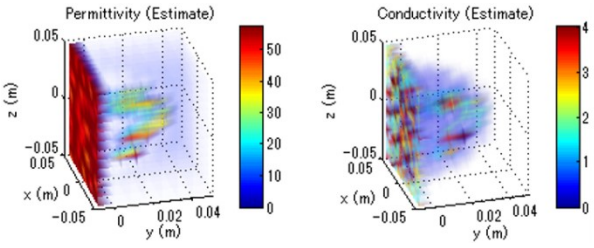

(b) Single polarization

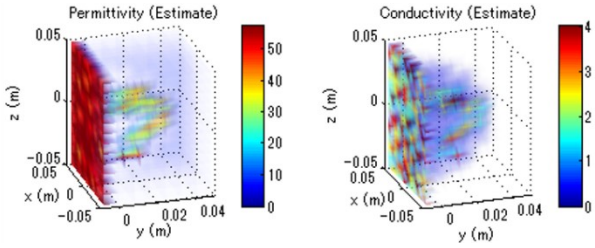

(c) Multi-polarization

Figure 5.17 Actual and estimated 3-D image reconstructions for 36DBIM_Br.II

Meanwhile, Figure 5.18 shows the dielectric properties distribution for the analysis region. The reconstructed parameters of the cancer for different polarizations are as follows. Single polarization (SP): $\{\varepsilon_r, \sigma\}$ = {52.70, 1.10 [S/m]}, and multi-polarization (MP): $\{\varepsilon_r, \sigma\}$ = {46.09, 3.36 [S/m]}. We observed that the relative permittivity of cancer is accurately estimated, and the conductivity of cancer is significantly low when using single polarization. Nevertheless, the conductivity of cancer are improved and approximately estimated using multi-polarization. The x-axis projection of the actual and reconstruction values of the dielectric properties including the cancer voxel obtained is shown in Figure 5.19. These results also demonstrate that the configuration with multi-polarization reconstruct the dielectric properties sufficiently compared to single polarization.

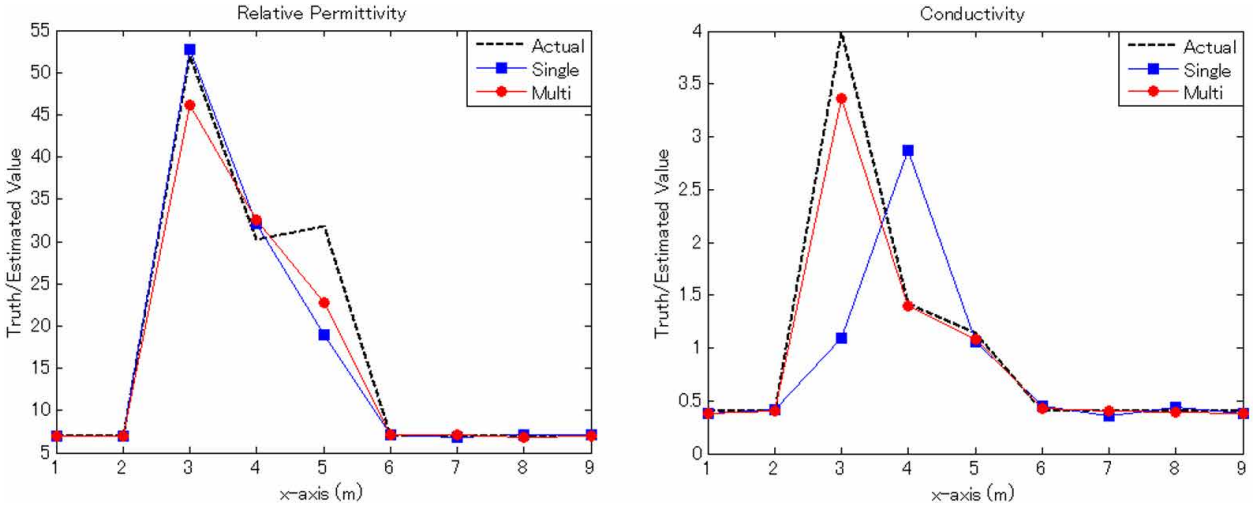

(a) Relative permittivity (b) Conductivity

Figure 5.18 Dielectric property distribution for 36DBIM_Br.II

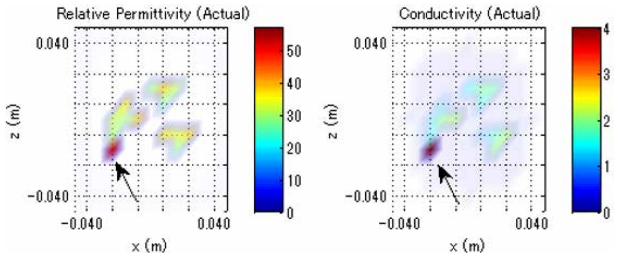

(a) Actual

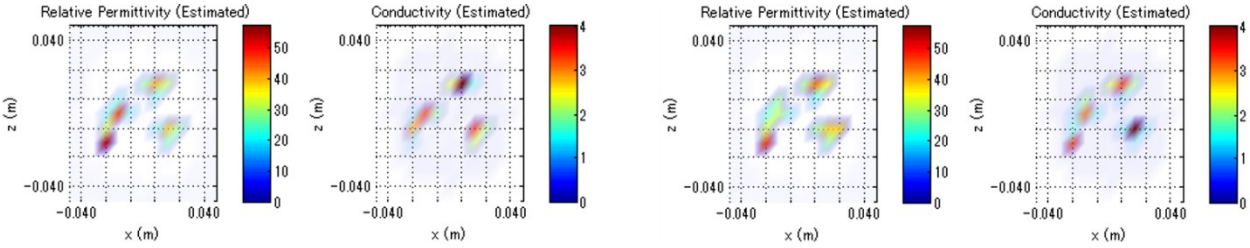

(b) Single polarization (c) Multi-polarization

Figure 5.19 Reconstructed dielectric properties at cross-section for 36DBIM_Br.II

5.4.4 Discussion on 36DBIM_Br.II

From results in Figure 5.17 – 5.19, we have verified that 36-elements antenna array can reconstruct the imaging object in 8-mm resolution. These results are supported by the average correlation of coefficient of antennas and the performance metrics. The average correlation of coefficient of antennas for two kind of polarizations are given as {SP, MP} = {0.1853, 0.1780}. The correlation coefficient was slightly reduced when using multi-polarization compared to single polarization. The combination of vertical polarization on the side panel and horizontal polarization on the top panel in the single polarization configuration gives low correlation coefficient, hence an adequate image reconstruction was obtained, compared to uniform polarizations in Section 5.4.1. This is also resulted from the increment on number of measurements, thus can reduce the ill-posedness of inverse problem. In addition, the multi-polarization configuration can enhance the reconstruction of the imaging object, compared to single polarization.

The performance metrics for 100 iteration is shown in Figure 5.20. The quality factor for both polarizations are increasing and towards unity along with iteration number. At 250th iteration, the quality factor reached 0.9727 and 0.9770 when using single and multi-polarization, respectively. Meanwhile, the RMSE for single polarization is gradually decreasing, and the RMSE for multi-polarization start to decrease drastically after 20th iteration. Furthermore, we observe that the normalized error of both polarizations gradually converges towards iteration number, and the convergence behavior of multi-polarization was much smoother after 30th iteration.

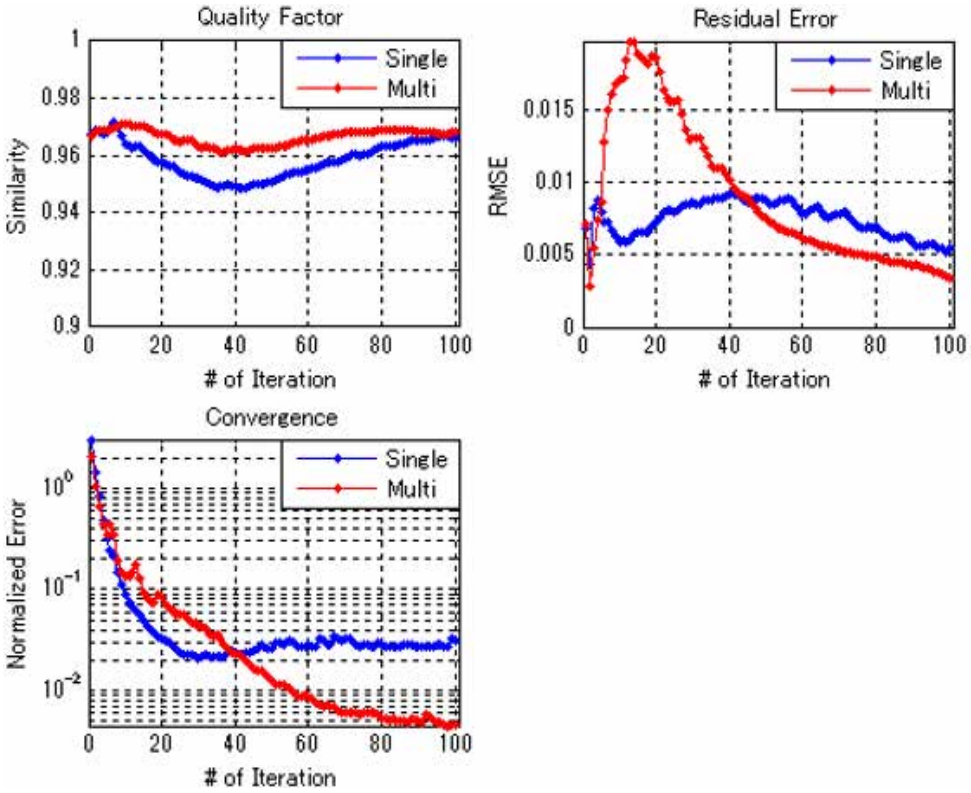

Figure 5.20 Performance metrics for 36DBIM_Br.II

Overall, the array configuration with single polarization and multi polarization perform similar results, for a given breast model, but multi-polarization gives slightly better results than the other. Thus, there is no reason to avoid introducing additional polarizations in Figure 4.5(a) if

doing so will yield other benefits. The results also indicate that multi-polarization configurations enhance imaging performance compared to single polarization configuration, and thus represent viable design options for microwave breast imaging systems.

CHAPTER 6

CONCLUSION

6.1 Conclusion

Microwave imaging based for breast cancer detection has the potential to be used for cancer diagnosis and to replace currently used clinical methods, based on its low cost, non-ionizing radiation, efficiency and small dimensions. The work included in this thesis is the continuity from the establishment of the microwave mammography research at Shizuoka University under supervision of Professor Yoshihiko Kuwahara.

In this thesis, we proposed microwave tomography method as an alternative to UWB radar imaging for breast cancer detection. In microwave tomography, it is necessary to increase the amount of diverse observation data for accurate image reconstruction of the dielectric properties of the imaging area. The multi-polarization method has been proposed as a suitable technique for the acquisition of a variety of observation data. The effectiveness of employing multi-polarization to reconstruct images is investigated. In order to investigate the effectiveness of multi-polarization, a compact-sized imaging sensor using multi-polarization for breast cancer detection is presented. Along with this, a simple breast model and a tissue-mimicking of real breast model were also proposed. The physical considerations related to image reconstruction also has been examined, where an analysis of the correlation coefficient of the received data of adjacent antennas was performed to interpret the imaging results.

Microwave tomography is an inverse scattering problem which is typically nonlinear and ill-posed. For the forward problem, MoM is used to obtain the measurement scattering data. For the inverse problem, two approaches were proposed to solve the non-linear inverse scattering method, i.e., Newton-Kantorovich and DBIM. In addition, three types of solving techniques to

reduce the ill-posedness and perform more stable solution were also introduced. The ill-posed of non-linear problem can be avoided by the choosing appropriate solving techniques, considerable number of unknowns used in the analysis region, and the use of a *priori* information.

A feasibility study has been performed on breast model with Newton-Kantorovich in 12-mm resolution. In this case, the dielectric permittivity was well reconstructed for multi-polarization configuration even with empirically determined regularization parameter. Furthermore, we have confirmed the effectiveness of applying multi-polarization to transmit and receive antennas to determine the dielectric property distributions in 8-mm resolution using DBIM. This is achieved using our proposed compact-sized of antenna array configuration and a mimicked breast model. In addition, the correlation coefficient of multi-polarization is relatively low compared to those corresponding to uniform polarizations. For this reason, the correlation coefficient may represent a viable parameter for image reconstruction in microwave tomography aimed at breast cancer detection.

6.2 Recommendation

MoM is the conventional approach for solving volume integral equations in the frequency domain. However, given the complex nature and large number of unknowns, MoM for volume integral equations is too computationally expensive. The Finite Difference Time Domain (FDTD) method is the most widely used numerical modeling technique to model the propagation of electromagnetic waves in biological tissue [85]. In the forward problem, FDTD can be considered to substitute MoM in order to model the propagation and calculate the scattering field accurately. Furthermore, higher resolution and sensitivity of image reconstruction can be accomplished by FDTD approach.

An accurate FDTD breast model must account for the physical geometry of the breast, the natural heterogeneity and dispersive nature of normal breast tissue. This approach is differ to

our proposed method that model the variance of dielectric properties as being randomly distributed. The details on MRI-derived breast model is explained in Appendix D. The numerical simulations in 12-mm resolution using the breast model and 36-elements antenna with simulator FEMTET were reported by Mr. Ozawa Naoyuki in [82] and still need further improvements.

Lastly, Debye model for complex permittivity in Equation (2.3) is commonly used as the dispersive behavior of breast tissue. Since this model has three unknown parameters in the imaging domain, which are ε_∞, $\Delta\varepsilon$ and σ_s, a linear Debye relationship between the three parameters can be implemented, as proposed in [86]. The resulting linear model will reduce the number of unknowns to one parameter, ε_s per cell in the computation. This method can reduce the computational cost and the complexity of the microwave breast imaging problem.

APPENDICES

Appendix A

Method of Moments (MoM) [7]

A. Integral Formulation

Consider an arbitrary shape of a finite body with relative permittivity $\varepsilon_r(r)$ and conductivity $\sigma(r)$, illuminated in free-space by electromagnetic wave, The induced current in the body generates a scattered field E^s, which may be represented by Equation (A.1).

$$J_{eq}(r) = [\sigma(r) + j\omega(\varepsilon_r(r) - \varepsilon_0)]E(r) = \tau(r)E(r) \tag{A.1}$$

The first-term of Equation (A.1) is the conduction current and the second terms is the polarization current. J_{eq} is the free-space current density, ε_0 is the free-space permittivity, and $E(r)$ is the total electric field inside the body. According to Van Bladel's paper, the scattered field E^s at an arbitrary point inside the body can be expressed as follows.

$$E^s(r) = \int_V J_{eq}(r') \cdot \left[PV\ G(r,r') - \frac{I\delta(r-r')}{3j\omega\varepsilon_0}\right] dV'$$

$$= \text{PV} \int_V J_{eq}(r') \cdot G(r,r')\, dV' - \frac{J_{eq}(r)}{3j\omega\varepsilon_0} \tag{A.2}$$

$$G(r,r') = -j\omega\mu_0 \left[1 + \frac{\nabla\nabla}{k_0^2}\right] \psi(r,r') \tag{A.3}$$

$$\psi(r,r') = \frac{exp(-jk_0|r-r'|)}{4\pi|r-r'|}, \qquad k_0 = \omega(\mu_0\varepsilon_0)^{1/2} \tag{A.4}$$

μ_0 is the permeability of free space, $G(r,r')$ is the free-space tensor Green's function, and the PV symbol denotes the principal value of the integral as defined by Van Bladel.

The total electric field $E(r)$ inside the body may written as the sum of the incident electric field E^i and the scattered field E^s, as shown in Equation (A.5).

$$E(r) = E^i(r) + E^s(r) \qquad \text{Eq. (A.5)}$$

Substituting Equation (A.2) in (A.5) and rearranging terms gives the desired integral equation for $E(r)$ in Equation (A.6). In Equation (A.6), $E^i(r)$ is the incident electric field and is a known quantity. $E(r)$ is the unknown total electric field inside the body. $E(r)$ can be determined from Equation (A.6) by method of moment (MoM).

$$\left[1+\frac{\tau(r)}{3j\omega\varepsilon_0}\right]E(r)-PV\int_V \tau(r')E(r')\cdot G(r,r')dV'=E^i(r) \qquad \text{Eq. (A.6)}$$

B. <u>Transformation to Matrix Equation</u>

We may represent the inner product $E(r')\cdot G(r,r')$ as follows:

$$\mathrm{E(r')\cdot G(r,r')}=\begin{bmatrix}\mathrm{G_{xx}(r,r')} & \mathrm{G_{xy}(r,r')} & \mathrm{G_{xz}(r,r')}\\ \mathrm{G_{yx}(r,r')} & \mathrm{G_{yy}(r,r')} & \mathrm{G_{yz}(r,r')}\\ \mathrm{G_{zx}(r,r')} & \mathrm{G_{zy}(r,r')} & \mathrm{G_{zz}(r,r')}\end{bmatrix}\begin{bmatrix}\mathrm{E_x(r')}\\ \mathrm{E_y(r')}\\ \mathrm{E_z(r')}\end{bmatrix} \qquad (A.7)$$

Let $x_1=x \quad x_2=y \quad x_3=z$

Then, $G_{x_px_q}(r,r')$ is given by

$$\mathrm{G_{x_px_q}(r,r')}=-\mathrm{j\omega\mu_0}\left[\delta_{\mathrm{pq}}+\frac{1}{\mathrm{k_0^2}}\frac{\partial^2}{\partial \mathrm{x_q}\,\partial \mathrm{x_p}}\right]\psi(\mathrm{r,r'}),\quad \mathrm{p,q}=1,2,3 \qquad (A.8)$$

The matrix in Equation (3A7) is symmetric. Each scalar component of (A.6) may be written as

$$\left[1+\frac{\tau(r)}{3j\omega\varepsilon_0}\right]E_{x_p}(r)-PV\cdot\int_V \tau(r')\left[\sum_{q=1}^{3}G_{x_px_q}(r,r')E_{x_q}(r')\right]dV'=E^i_{x_p}(r),\qquad p=1,2,3 \qquad (A.9)$$

Starting from exact integral equation formulations in Equation (A.6), the MoM is utilized to generate matrix equations for the forward scattering problem. We partition the body into N subvolumes and assume that $E(r)$ and $\tau(r)$ are constant in each subvolume. We will denote the m-th subvolume by V_m, and denote the position of a representative interior point of V_m by r_m. By requiring that (A.9) be satisfied at each r_m, after some rearranging, we obtain

$$\left[1+\frac{\tau(r_m)}{3j\omega\varepsilon_0}\right]E_{x_p}(r_m)-\sum_{q=1}^{3}\sum_{n=1}^{N}\left[\tau(r_n)\,PV\cdot\int_{V_n}G_{x_px_q}(r_m,r')\,dV'\right]E_{x_q}(r_n)=E^i_{x_p}(r_m)$$

(A.10)

We define the following quantity in Equation (A.11)

$$\bar{G}_{x_px_q}{}^{mn}=\tau(r_n)\,PV\int_{V_n}G_{x_px_q}(r_m,r')\,dV' \tag{A.11}$$

Equation (A.10) can rewritten in Equation (A.12)

$$\sum_{q=1}^{3}\sum_{n=1}^{N}\left[\bar{G}_{x_px_q}{}^{mn}-\delta_{pq}\delta_{mn}\left(1+\frac{\tau(r_m)}{3j\omega\varepsilon_0}\right)\right]E_{x_q}(r_n)=-E^i_{x_p}(r_m),\quad m=1,2,\cdots,N,\ \ p=1,2,3.$$

(A.12)

$\left[G_{x_px_q}\right]$ is $N\times N$ matrix, and the elements are defined by

$$G_{x_px_q}{}^{mn}=\bar{G}_{x_px_q}{}^{mn}-\delta_{pq}\delta_{mn}\left[1+\frac{\tau(r_m)}{3j\omega\varepsilon_0}\right] \tag{A.13}$$

The $\left[E_{x_p}\right]$ and $\left[E^i_{x_p}\right]$ be N-dimensional vectors and given as Equation (A.14)

$$\left[E_{x_p}\right]=\begin{bmatrix}E_{x_p}(r_1)\\ \vdots\\ E_{x_p}(r_N)\end{bmatrix},\qquad \left[E^i_{x_p}\right]=\begin{bmatrix}E^i_{x_p}(r_1)\\ \vdots\\ E^i_{x_p}(r_N)\end{bmatrix},\ \ p=1,2,3. \tag{A.14}$$

As m and p range over all possible values in Equation (A.12), the following matrix representation of Equation (A.6) is obtained.

$$\begin{bmatrix}[G_{xx}] & | & [G_{xy}] & | & [G_{xz}]\\ -- & | & -- & | & --\\ [G_{yx}] & | & [G_{yy}] & | & [G_{yz}]\\ -- & | & -- & | & --\\ [G_{zx}] & | & [G_{zy}] & | & [G_{zz}]\end{bmatrix}\begin{bmatrix}E_x\\ --\\ E_y\\ --\\ E_z\end{bmatrix}=-\begin{bmatrix}[E^i_x]\\ --\\ [E^i_y]\\ --\\ [E^i_z]\end{bmatrix} \tag{A.15}$$

Symbolically, we rewritten Equation (A.15) as Equation (A.16)

$$[G][E]=-\left[E^i\right] \tag{A.16}$$

$[G]$ is a $3N\times 3N$ matrix, while $[E]$ and $\left[E^i\right]$ have dimension $3N$. The total electric field at each of the N points can be determined by inverting $[G]$ in Equation (A.16).

C. Evaluation of Matrix Elements

Equation (A.11) and (A.13) define the elements of $\left[G_{x_p x_q}\right]$.

$$G_{x_p x_q}{}^{mn} = \tau(r_n)\, PV \int_{V_n} G_{x_p x_q}(r_m, r')\, dV' - \delta_{pq}\delta_{mn}\left[1 + \frac{\tau(r_m)}{3j\omega\varepsilon_0}\right] \tag{A.17}$$

The off-diagonal elements of $\left[G_{x_p x_q}\right]$ is considered.

$$G_{x_p x_q}{}^{mn} = \tau(r_n) \int_{V_n} G_{x_p x_q}(r_m, r')\, dV', \quad m \neq n. \tag{A.18}$$

At first approximation, we have

$$G_{x_p x_q}{}^{mn} = \tau(r_n) G_{x_p x_q}(r_m, r_n)\Delta V_n, \quad m \neq n. \tag{A.19}$$

$$\Delta V_n = \int_{V_n} dV'.$$

We use Equation (A.8) to evaluate $G_{x_p x_q}(r_m, r_n)$.

$$\begin{aligned} G_{x_p x_q}{}^{mn} &= \frac{-j\omega\mu_0 k_0 \tau(r_n)\Delta V_n \exp(-j\alpha_{mn})}{4\pi {\alpha_{mn}}^3} \\ &\cdot [({\alpha_{mn}}^2 - 1 - j\alpha_{mn})\delta_{pq} + \cos\theta_{x_p}{}^{mn} \\ &\cdot \cos\theta_{x_q}{}^{mn}(3 - {\alpha_{mn}}^2 + 3j\alpha_{mn})], \quad m \neq n. \end{aligned} \tag{A.20}$$

$$\alpha_{mn} = k_0 R_{mn} \qquad R_{mn} = |r_m - r_n|$$

$$\cos\theta_{x_p}{}^{mn} = \frac{\left(x_p^m - x_p^n\right)}{R_{mn}} \qquad \cos\theta_{x_q}{}^{mn} = \frac{\left(x_q^m - x_q^n\right)}{R_{mn}}$$

$$r_m = (x_1^m, x_2^m, x_3^m) \qquad r_n = (x_1^n, x_2^n, x_3^n).$$

For diagonal elements of $\left[G_{x_p x_q}\right]$, Equation (A.17) becomes

$$G_{x_p x_q}{}^{nn} = \tau(r_n)\, PV \int_{V_n} G_{x_p x_q}(r_n, r')\, dV' - \delta_{pq}\left[1 + \frac{\tau(r_n)}{3j\omega\varepsilon_0}\right] \tag{A.21}$$

In Equation (A.21), we approximate V_n by a sphere of equal volume centered at r_n, and a_n is the radius of the sphere.

$$G_{x_p x_q}{}^{nn} = \delta_{pq}\left\{\frac{-2j\omega\mu_0\tau(r_n)}{3k_0^2}[\exp(-jk_0 a_n)(1 + jk_0 a_n) - 1] - \left[1 + \frac{\tau(r_n)}{3j\omega\varepsilon_0}\right]\right\} \tag{A.22}$$

$$a_n = \left(\frac{3\Delta V_n}{4\pi}\right)^{1/3}$$

Appendix B

Analytical of Jacobian [54]

An analytic expression for the Jacobian matrix J is derived. Consider first-order variations of Equation (3.13) and (3.14)

$$\delta e_v = G^r \delta[C e_v] \tag{B.1}$$

$$\delta e_v^s = G_v^s \delta[E_v c] \tag{B.2}$$

Where $E_v c = C e_v$

$$\delta[C e_v] \approx [\delta C] e_v + C[\delta e_v] \tag{B.3}$$

Substituting Equation (B.1) into (B.3) gives

$$\delta[C e_v] = [I - C G^r]^{-1} [\delta C] e_v \tag{B.4}$$

Substituting Equation (B.4) into (B.2) gives

$$J_v = G_v^s [I - C G^r]^{-1} E_v \tag{B.5}$$

For the $M \times N$ derivative matrix J_v relating the field and contrast variations δe_v^s and δc. The computation of $[I - C G^r]^{-1}$ is straightforward since its transposed $[I - G^r C]^{-1}$ has been computed in the forward problem.

Gathering the v points of matrices J_v in one matrix yields the Jacobian J, and E is the total field inside the object region.

$$J = G^s [I - C G^r]^{-1} E \tag{B.6}$$

Appendix C

Preconditioning Bi-Conjugate Gradient Stabilized Method (Bi-CGSTAB) Algorithm [84]

The algorithm of the preconditioned with Bi-CGSTAB for solving linear equations $Ax = b$ is as follow. K : preconditioning matrix, i.e., $K \approx A$. r_i : residual vectors.

x_0 is an initial guess (zero vector) to calculate $r_0 = b - Ax_0$
$\widehat{r_0}$ is an arbitrary vector, such that $(\widehat{r_0}, r_0) \neq 0$, e.g., $\widehat{r_0} = r_0$
$\rho_0 = \alpha = \omega_0 = 1, \quad v_0 = p_0 = 0$
for i $= 1, 2, 3, \cdots,$
$\rho_i = (\widehat{r_0}, r_{i-1});$
$\beta = (\rho_i/\rho_{i-1})(\alpha/\omega_{i-1});$
$p_i = r_{i-1} + \beta(p_{i-1} - \omega_{i-1}v_{i-1});$
$y = K^{-1}p_i$
$v_i = Ay;$
$\alpha = p_i/(\widehat{r_0}, v_i);$
$s = r_{i-1} - \alpha v_i;$
$z = K^{-1}s;$
$t = Az$
$\omega_i = (K_1^{-1}t, K_1^{-1}s)/(K_1^{-1}t, K_1^{-1}t);$
$x_i = x_{i-1} + \alpha y + \omega_i z;$
if x_i is accurate enough then quit;
$r_i = s - \omega_i t;$
end

This scheme too delivers the variables x_i and r_i corresponding to the original system $Ax = b$. Preconditioning matrix K is determined from the matrix D obtained by extracting the diagonal elements of the matrix the A. This preconditioning is generally referred as diagonal scaling.

Appendix D

MRI-derived Breast Model and Numerical Simulation using Finite Difference Time Domain (FDTD) method

A. FDTD Breast Model

Mr. Yuki Ono from Sumitomo Electric Industries, Ltd. has developed an FDTD breast model based on the actual MRI images obtained from Hamamatsu University School of Medicine, Hamamatsu Shizuoka, as shown in Figure D.1. The breast model with 1.0 mm grid dimension is consists of skin, adipose tissue, fibro glandular tissue, malignant tissue (cancer) and chest wall (muscle). The breast model is characterized to corresponding dielectric properties shown in Table D.1. In FDTD numerical simulation, the grid dimension for the breast model is downgraded to 3.0 mm. For sake of simplicity, the background, muscle and skin are neglected in the analysis region. Therefore, the analysis region only consists of adipose tissue, fibro-glandular tissue and malignant tissue (cancer), as shown in Figure D.2. The number of unknown to be reconstructed within the analysis region is 6727 cells.

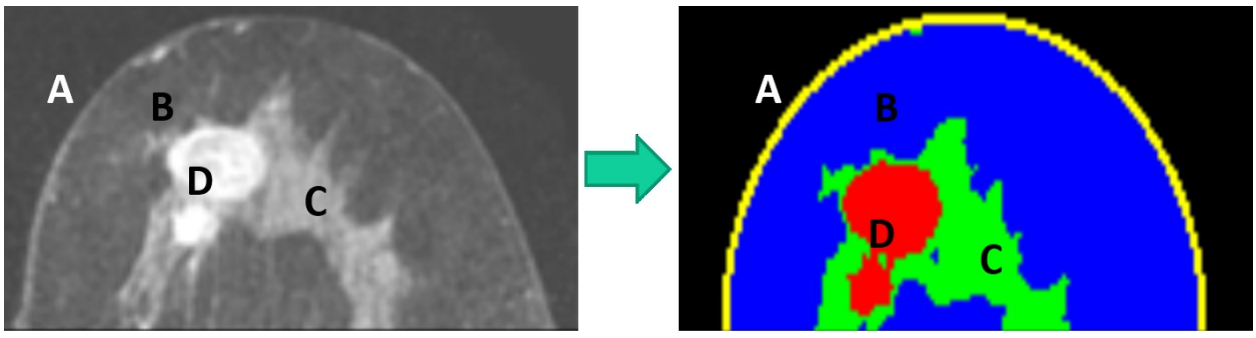

(a) MRI image (b) Numerical breast model

Figure D.1 MRI-derived numerical breast phantom by Kuwahara et. al. [82];
A: background, B : adipose tissue, C : fibro-glandular tissue, D: malignant tissue (cancer)

Table D.1 Dielectric properties in FDTD breast model

Parameter	Background ± dev.*	Adipose ± dev.*	Glandular ± dev.*	Cancer ± dev.*	Muscle ± dev.*	Skin ± dev.*
ε_r	6.2 ± 0.01	6.5 ± 0.05	40.0 ± 0.10	54 ± 0.05	50.0 ± 0.05	35.0 ± 0.05
σ [S/m]	0.15 ± 0.01	0.20 ± 0.05	1.0 ± 0.10	1.3 ± 0.05	1.13 ± 0.05	0.8 ± 0.05

*dev. = deviation

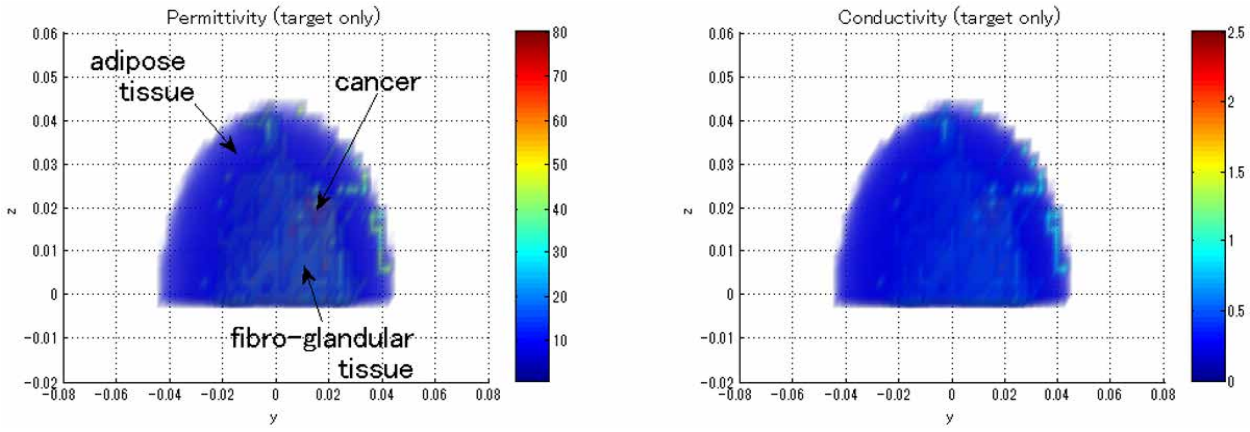

(a) zy-view

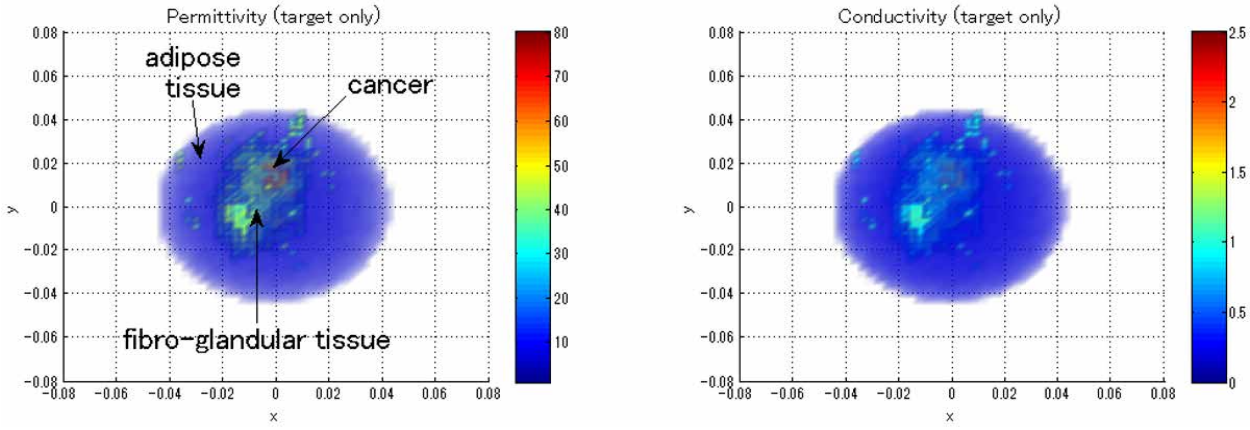

(b) xy-view

Figure D.2 MRI-derived FDTD breast model

B. FDTD Antenna Configuration

In FDTD numerical simulation, the single frequency used is 1.8 GHz, which gives the length of the antenna leg is 4. The dimension for the enclosed antenna array is width 144 × length 144 × height 60 mm. Here, the z-axis is taken as vertical polarization, meanwhile x-axis or y-axis is horizontal polarization. Figure D.3 shows the one side of 32-element antenna array configuration modeled in FDTD for three types of polarization. The antenna arrangements for each side are identical, and the four side-panels are parallel to either the xz- or yz-plane.

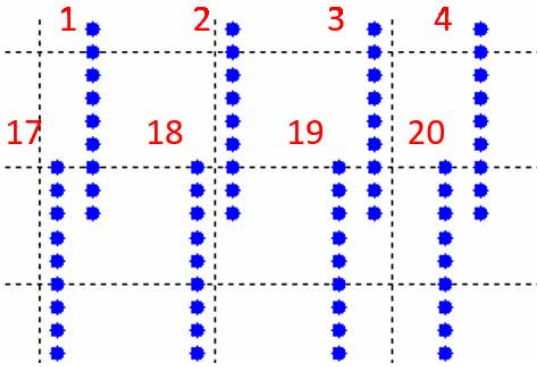

(a) Vertical polarization (VP)

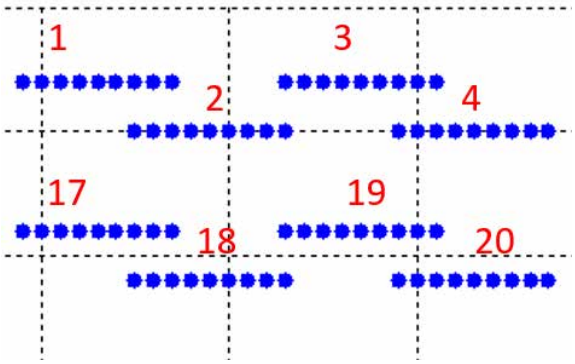

(b) Horizontal polarization (HP)

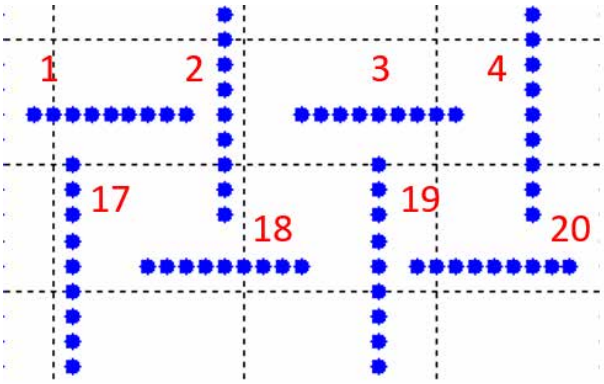

(c) Multi-polarization (MP)

Figure D.3 32-element antenna array configuration in FDTD

C. Numerical Simulations

The numerical simulations using Figure D.2 – D.3 after 50 iterations are presented. The initial guess is given by $\{\varepsilon_r, \sigma\}$ = {6.5, 0.2 [S/m]}, which is equivalent to the adipose tissue. A simple bound constraints is applied to the contrast perturbations to reduce the span of the solution space that leads to an underdetermined, and ill-posed system.

Figure D.4 – D.6 show the actual and reconstruction images for all polarizations in axial view, sagittal view, and coronal view, respectively. In the actual model, the fibro-glandular tissue and cancer are shown in cyan and yellow, respectively for both parameters. The shape and location of fibro-glandular tissue and cancer were unsatisfied when using the configurations in Figure D.3(a) and Figure D.3(b). In contrast, the quality of image reconstructions are improved using the configuration in Figure D.3(c). Overall, the multi-polarization configuration exhibit better image reconstructions than the vertical and horizontal polarizations.

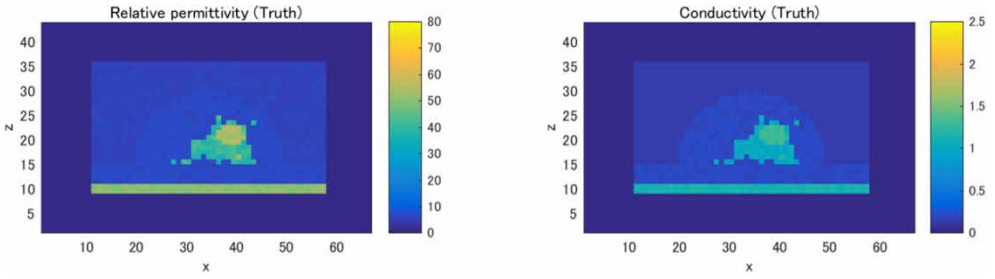

(a) Actual

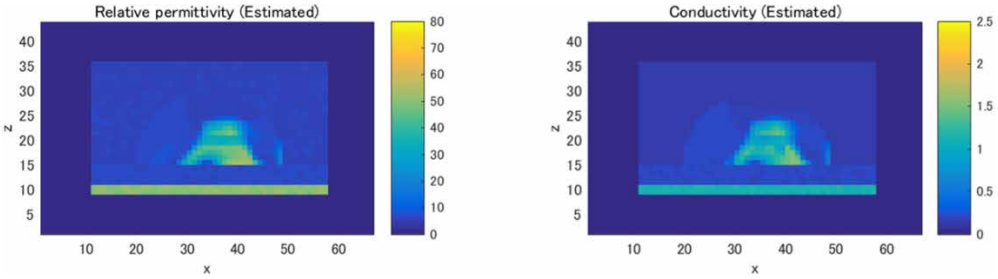

(b) Vertical polarization

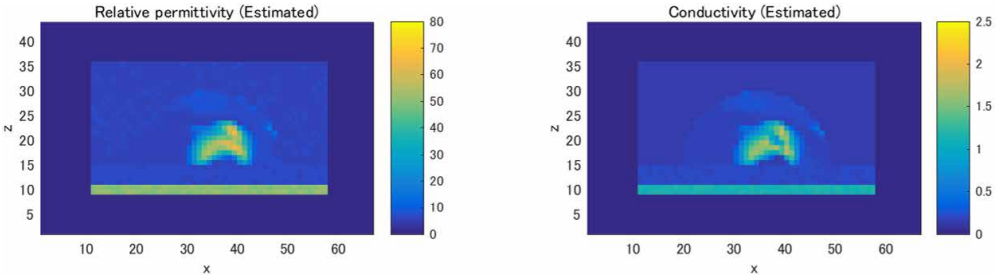

(c) Horizontal polarization

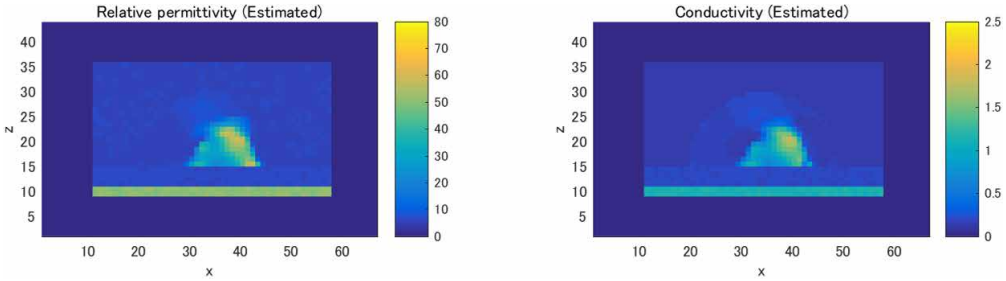

(d) Multi-polarization

Figure D.4 Image reconstruction in axial view

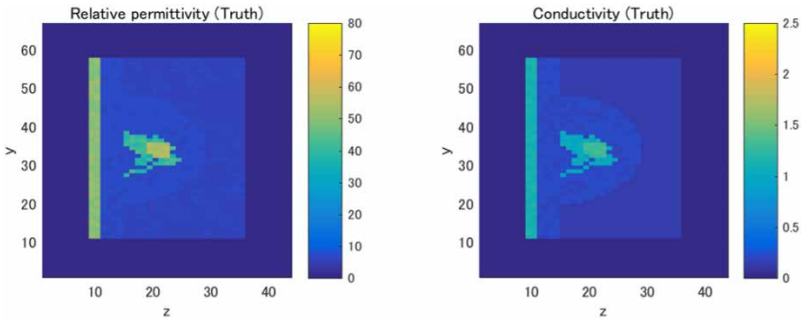

(a) Actual

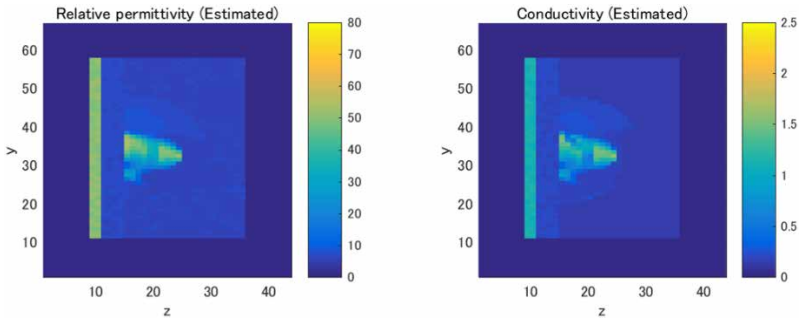

(b) Vertical polarization

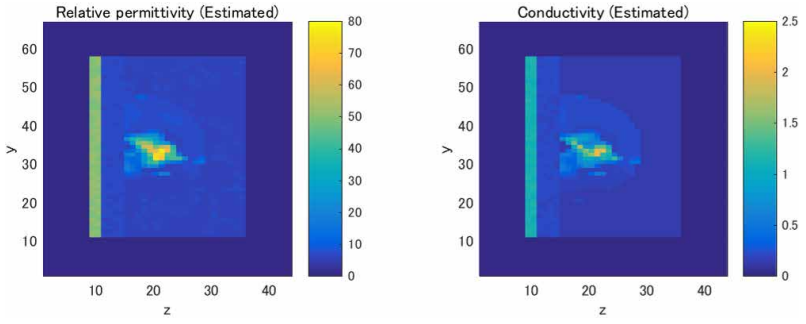

(c) Horizontal polarization

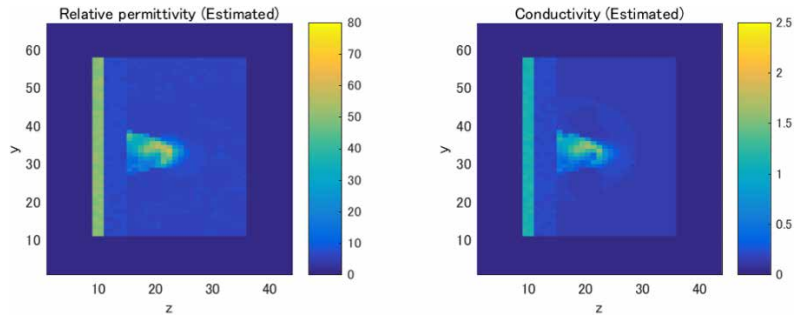

(d) Multi-polarization

Figure D.5 Image reconstruction in sagittal view

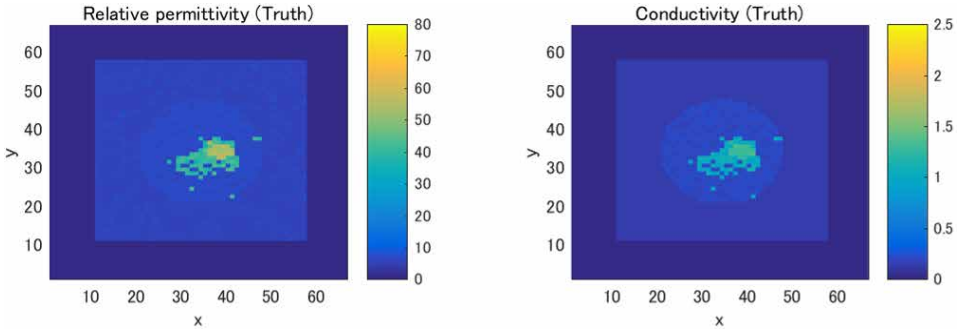

(a) Actual

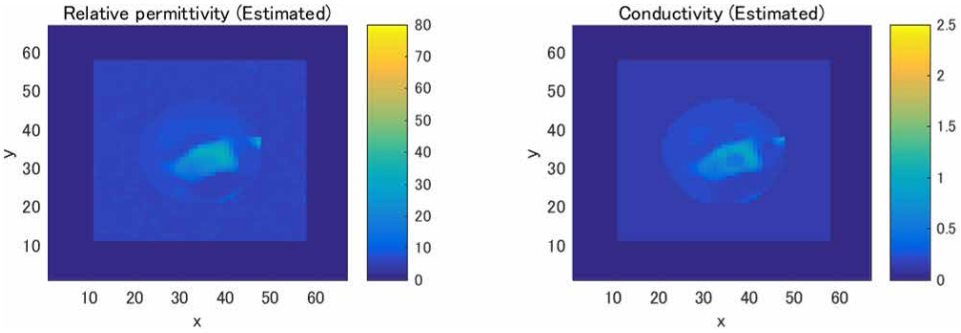

(b) Vertical polarization

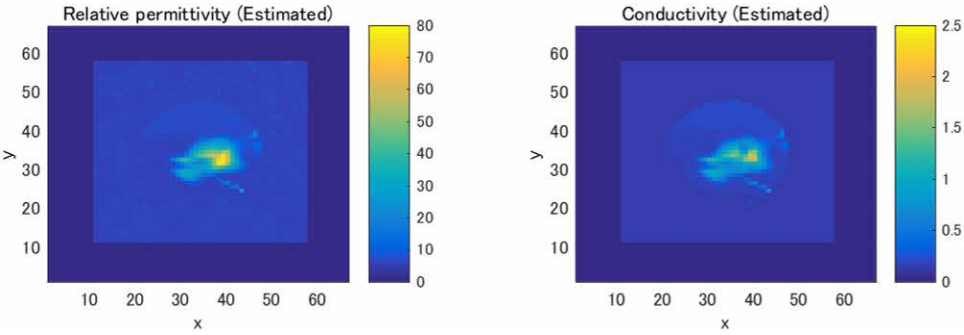

(c) Horizontal polarization

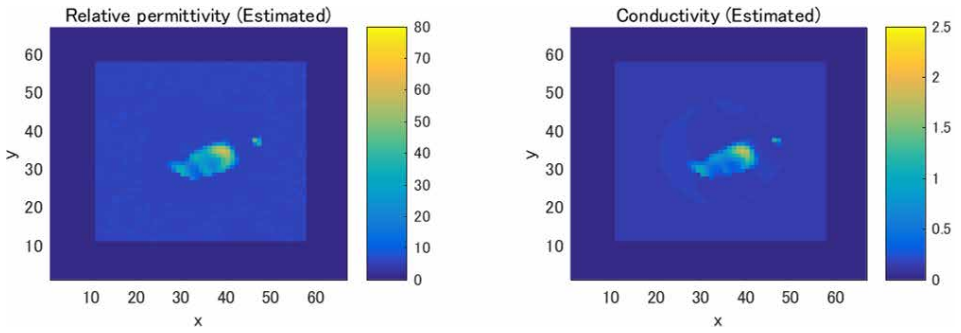

(d) Multi-polarization

Figure D.6 Image reconstruction in coronal view

The actual (red solid line) and estimated values (blue asterisk) of the dielectric properties in the analysis region for all polarizations is shown in Figure D.7. Overall, the multi-polarization configuration enhanced the performance of uniform polarizations to yield better reconstruction.

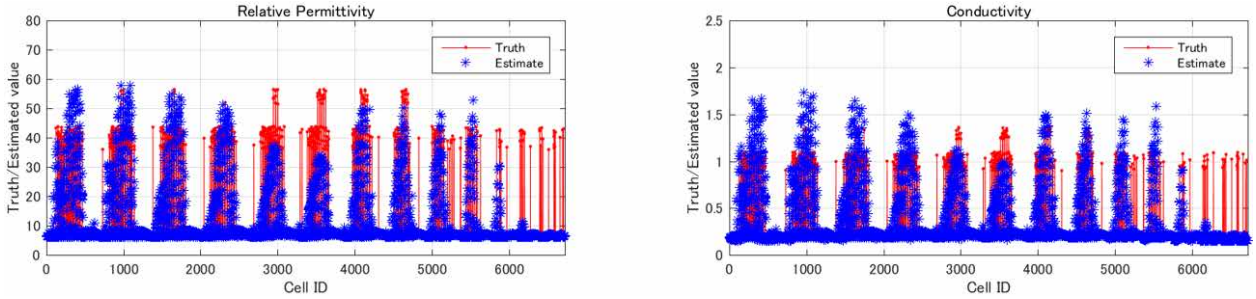

(a) Vertical polarization

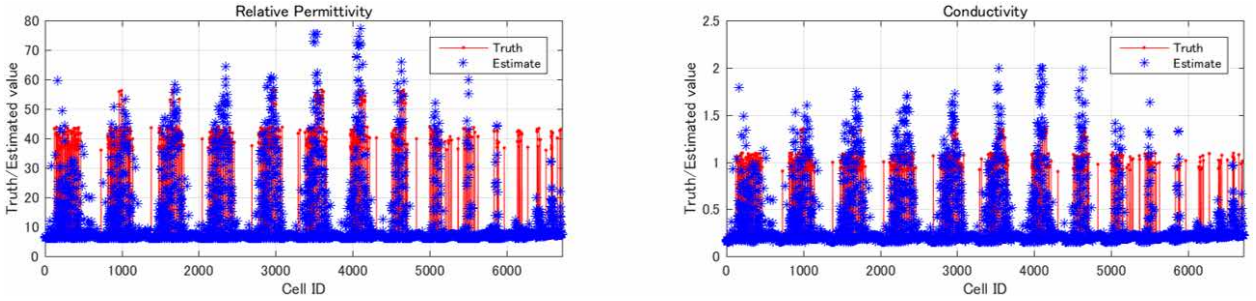

(b) Horizontal polarization

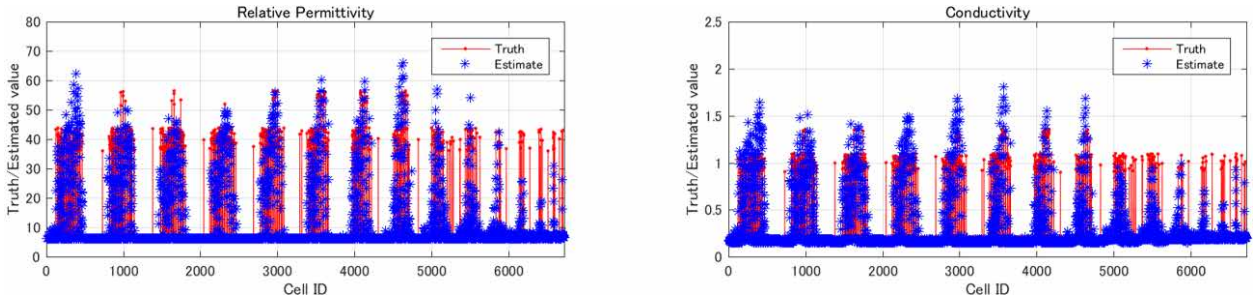

(c) Multi-polarization

Figure D.7 Dielectric property distribution among polarizations

The average correlation of coefficient of adjacent antennas for all polarizations are given as {VP, HP, MP} = {0.8070, 0.4998, 0.2448}. Overall, the correlation coefficient was reduced when using multi-polarization compared to uniform polarizations. An adequate image reconstruction was obtained using multi-polarization owing to the low correlation coefficient, as shown in Figure D.4 – D.7. Meanwhile, Figure D.8 shows the performance metrics in FDTD modeling. Figure D.8(a) illustrates that the quality factor are increasing when using vertical and multi-polarization along with iteration number. At 20th iteration, the quality factor of multi-polarization reached 0.8735 and maintaining its value. In Figure D.8(b), the RMSE for vertical and multi-polarization are gradually decreasing, and the RMSE for multi-polarization start to decrease drastically after 8th iteration compared to uniform polarizations.

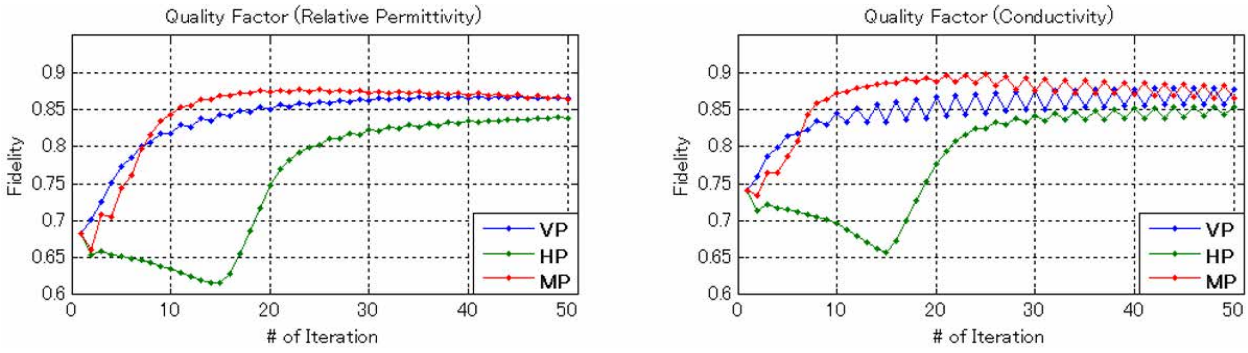

(a) Quality Factor

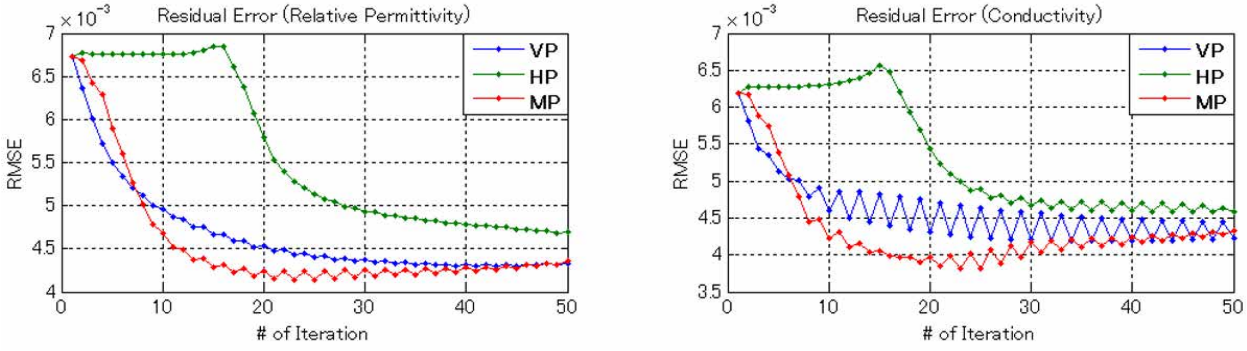

(b) RMSE

Figure D.8 Performance metrics in FDTD modeling for all polarizations

Appendix E

Polynomial Fitting of Breast Model

In this section, the dielectric properties of relative permittivity, ε_r and conductivity, σ is compared to obtain a linear model (polynomial fit) to mend their gap. Fitting requires a parametric model that relates the response data to the predictor data with one or more coefficients. The result of the fitting process is an estimate of the model coefficients [87]. Based on Least Square (LS) method described in [88], the polynomial fit is used to fit a linear model to data and provide approximation of dielectric properties. A linear model is defined as an equation that is linear in the coefficients. The linear least-squares fitting can be illustrated by a first-degree polynomial as written in Equation (E.1). In MATLAB, two commands are used to solve the unknown coefficients p_1 and p_2, which are polyfit and polyval.

$$y = p_1 x + p_2 \tag{E.1}$$

Figure E.1 shows the linear model between relative permittivity and conductivity for MRI-based breast model of Figure D.2. Since the adipose tissue, fibro-glandular tissue and cancer are considered in the analysis region, the linear model in Figure E.1(b) with Equation (E.2) is chosen as the appropriate linear model to approximate the dielectric properties involved.

$$\sigma = 0.0233\varepsilon_r + 0.0531 \tag{E.2}$$

In FDTD reconstruction algorithm, Equation (E.2) is applied in the contrast function to replace the conductivity, σ. Therefore, the unknown parameter in the contrast function for linear model is only the relative permittivity, ε_r. This method can decrease the number of unknowns to estimate the contrast perturbations.

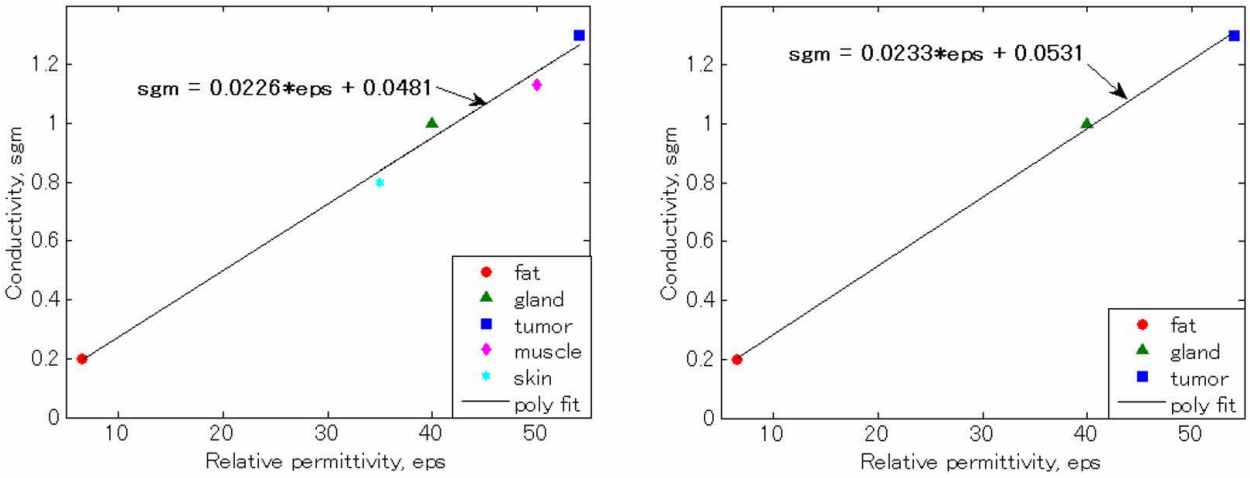

(a) (b)

Figure E.1 Linear model for MRI-based breast model (a) based on all tissues (b) based on adipose, fibro-glandular and cancerous tissue

The antenna array with multi-polarization configuration of Figure D.3(c) is used as the comparison between the non-linear and linear model. The image reconstruction in axial view, dielectric property distribution and the performance metrics after 10^{th} iteration are shown in Figure E.3 – E.5, respectively. For non-linear model in Figure E.3(b), the fibro-glandular tissue was gradually reconstructed, but the existence of cancer is unidentified. In contrast, the shape and location of cancer is distinctly visible when using the linear model, as shown in Figure E.3(c). In linear model, the decrease of unknown parameter can reduce the ill-posedness of inverse problem. Overall, the linear model show better image reconstruction than the non-linear model.

Meanwhile, the actual (red solid line) and estimated values (blue asterisk) of the dielectric properties in the analysis region for all polarizations is shown in Figure E.4. After 10^{th} iteration, the estimated values in Figure E.4(a) are low estimated, meanwhile in Figure E.4(b), the values are highly estimated. Overall, the linear model in Figure E.4(b) emphasize the estimation values of the non-linear model in Figure E.4(a) to yield an adequate image reconstruction.

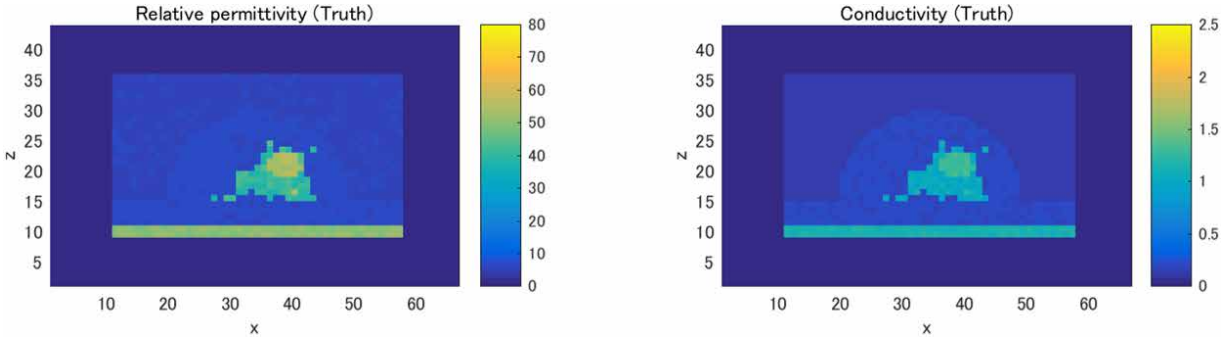

(a) Actual model

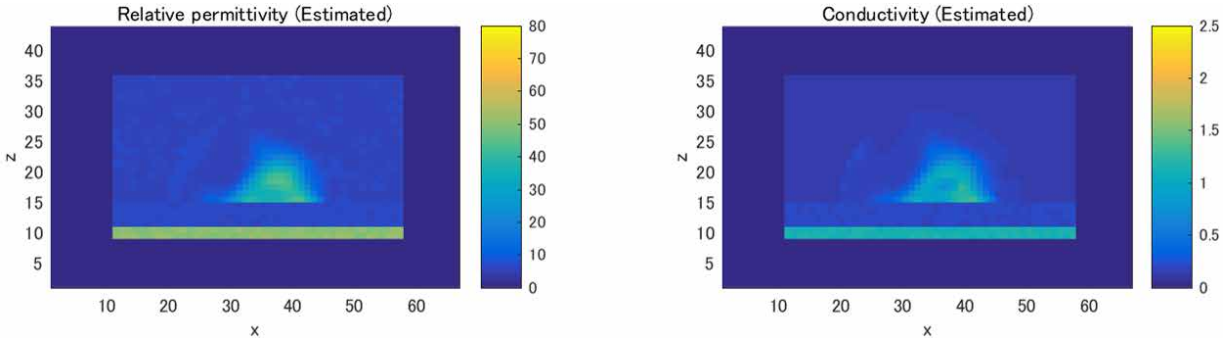

(b) Non-linear model

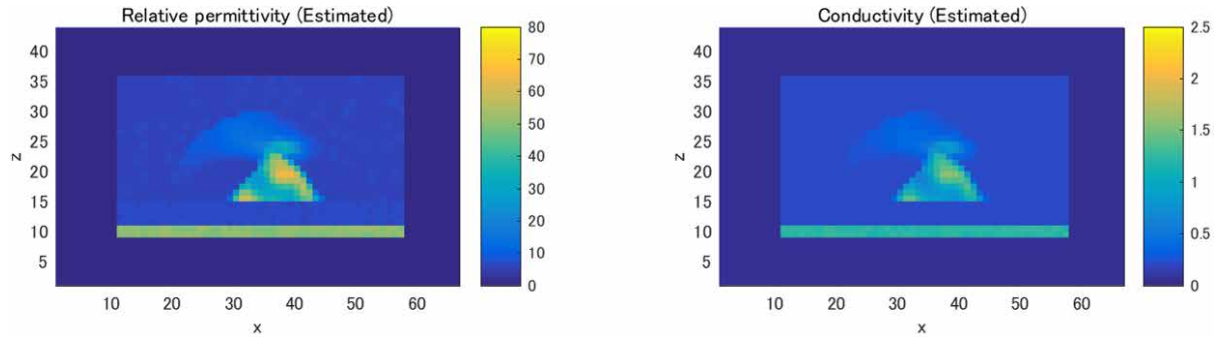

(c) Linear model

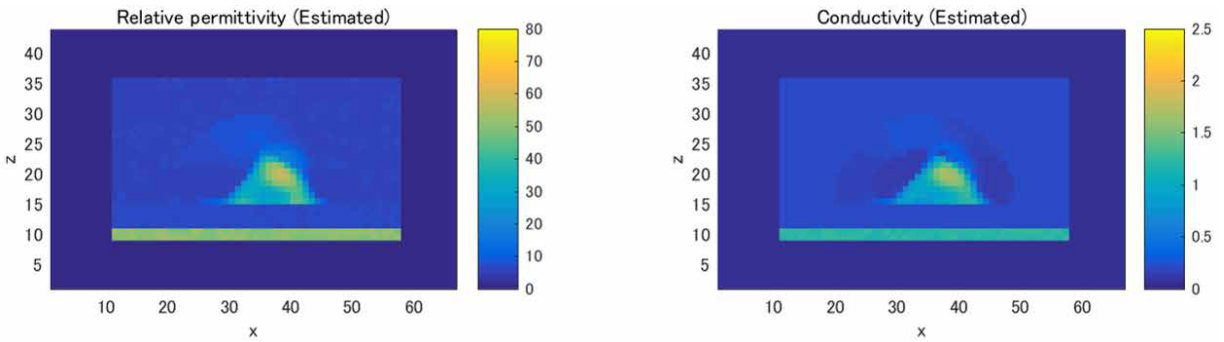

(d) Mix model

Figure E.3 Image reconstruction in axial view for non-linear, linear and mix model

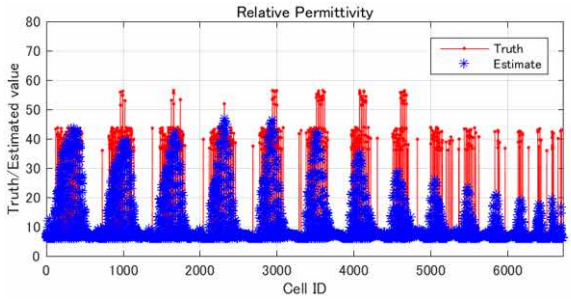

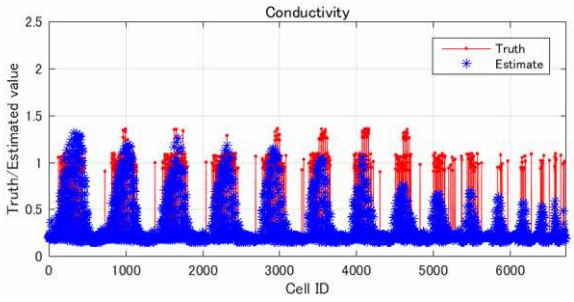

(a) Non-linear model

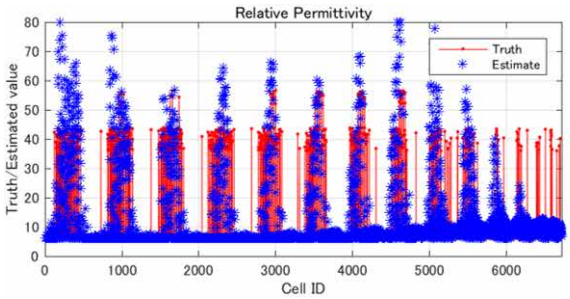

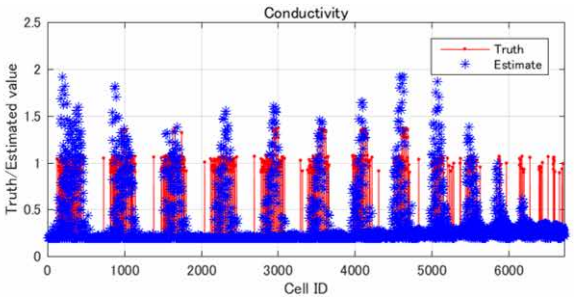

(b) Linear model

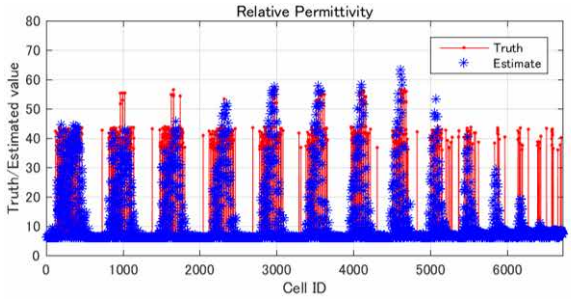

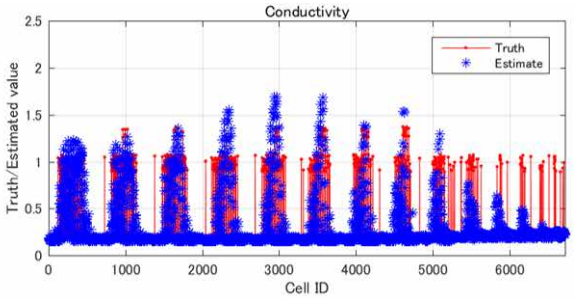

(c) Mix model

Figure E.4 Dielectric property distribution for non-linear, linear and mix model

Figure E.5(a) illustrates that the quality factor of linear model is increasing significantly after 3rd iteration, compared to the non-linear model. However, the quality factor of linear model decreasing after 5th iteration. In Figure E.5(b), the RMSE of linear model is decreasing remarkably after 2nd iteration, and it start to increase after 5th iteration. These results might lead to the overestimated in estimated values of linear model in Figure E.4(b).

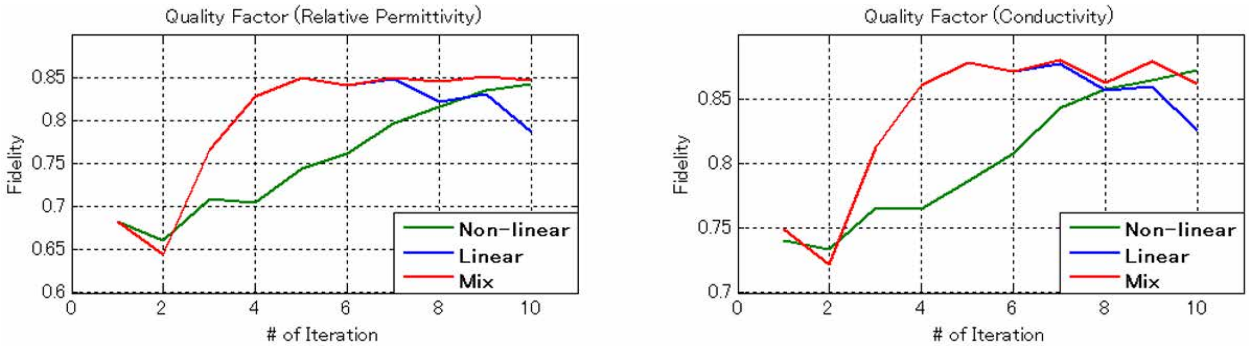

(a) Quality factor

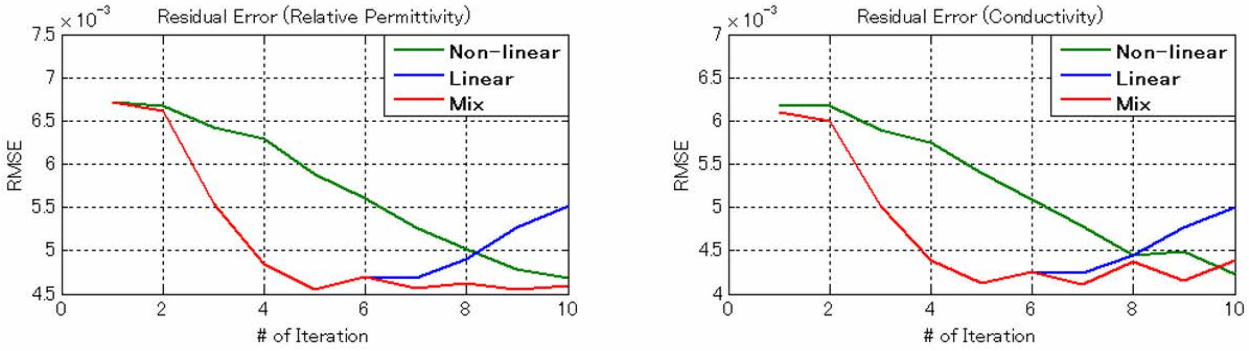

(b) RMSE

Figure E.5 Performance metrics in FDTD modeling for non-linear, linear and mix model

Therefore, a mix model, which consists of linear and non-linear model, is proposed to improve the performances. This step can be realized by applying the linear model in first 5 iterations, and the non-linear model after 5th iterations in the FDTD reconstruction algorithm. The results of mix model are shown in Figure E.3(d) and Figure E.4(c). Overall, the mix model enhanced the performances of the linear model to yield better reconstruction. The quality factor and RMSE of linear model is improved after 6th iteration when using the mix model. In conclusion, a mix of linear and non-linear model can produce sufficient image reconstruction, even in a small iteration number.

REFERENCES

[1] "World Cancer Report 2014 (ePUB) - WHO - OMS -." [Online]. Available: http://apps.who.int/bookorders/anglais/detart1.jsp?codlan=1&codcol=80&codcch=275. [Accessed: 12-May-2016].

[2] K. Saika and T. Sobue, "Epidemiology of Breast Cancer in Japan and the US," *J. Japan Med. Assoc.*, vol. 52(1), pp. 39–44, 2009.

[3] "Cancer Statistics in Japan 2015 (Graphs)," *Foundation for Promotion of Cancer Research*, 2015. [Online]. Available: http://ganjoho.jp/data/reg_stat/statistics/brochure/2015/cancer_statistics_2015_fig_E.pdf. [Accessed: 11-May-2016].

[4] T. Morimoto, T. Nagao, K. Okazaki, M. Kira, Y. Nakagawa, and A. Tangoku, "Current Status of Breast Cancer Screening in the World," *Breast Cancer (Japanese Breast Cancer Soc.*, vol. 16, no. 1, pp. 2–9, 2009.

[5] C. Hamashima, "The Japanese Guidelines for Breast Cancer Screening," *Jpn. J. Clin. Oncol.*, no. 1, pp. 1–11, 2016.

[6] N. K. Nikolova, "Microwave Imaging for Breast Cancer," *IEEE Microw. Mag.*, vol. 12, no. 7, pp. 78–94, 2011.

[7] D. E. Livesay and K.-M. Chen, "Electromagnetic Fields Induced Inside Arbitrarily Shaped Biological Bodies," *IEEE Trans Microw. Theory Tech.*, vol. MTT-22, no. 12, pp. 1273–1974, 1974.

[8] P. M. Meaney, M. W. Fanning, T. Raynolds, C. J. Fox, Q. Fang, C. a. Kogel, S. P. Poplack, and K. D. Paulsen, "Initial Clinical Experience with Microwave Breast Imaging in Woman with Normal Mammography," *Acad Radiol.*, vol. 8, no. 3, pp. 1–22, 2007.

[9] A. Baran, D. Kurrant, A. Zakaria, E. Fear, and J. LoVetri, “Breast Imaging Using Microwave Tomography with Radar-Based Tissue-Regions Estimation,” *Prog. Electromagn. Res.*, vol. 149, pp. 161–171, 2014.

[10] X. Li and S. C. Hagness, “A confocal microwave imaging algorithm for breast cancer detection,” *IEEE Microw. Wirel. Components Lett.*, vol. 11, no. 3, pp. 130–132, 2001.

[11] S. C. Hagness, A. Taflove, and J. E. Bridges, “Two-Dimensional FDTD Analysis of a Pulsed Microwave Confocal System for Breast Cancer Detection: Fixed-Focus and Antenna-Array Sensors,” *IEEE Trans Biomed. Eng.*, vol. 45, no. 12, pp. 1470–1474, 1998.

[12] E. C. Fear, X. Li, S. C. Hagness, and M. A. Stuchly, “Confocal Microwave Imaging for Breast Cancer Detection: Localization of Tumors in Three Dimensions,” *IEEE Trans Biomed. Eng.*, vol. 49, no. 8, pp. 812–822, 2002.

[13] Y. Kuwahara, S. Miura, Y. Nishina, K. Mukumoto, H. Ogura, and H. Sakahara, “Clinical setup of microwave Mammography,” *IEICE Trans. Commun.*, vol. E96-B, no. 10, pp. 2553–2562, 2013.

[14] Y. Kuwahara, S. Miura, Y. Nishina, K. Mukumoto, H. Ogura, and H. Sakahara, “Clinical Test of Microwave Mammography,” in *IEEE Antennas and Propagation Society, AP-S International Symposium (Digest)*, 2013, pp. 2028–2029.

[15] Y. Nishina, S. Miura, Y. Kuwahara, H. Sakahara, and H. Ogura, “Clinical Setup of Microwave Mammography: Phase 2,” in *Proceedings of ISAP2012*, pp. 483–486.

[16] Y. Kuwahara, “マイクロ波マンモグラフィの技術,” *RF World No.25*, pp. 8–19, 2013.

[17] Y. Kuwahara, K. Suzuki, H. Horie, and H. Hatano, “Conformal Array Antenna with the Aspirator for the Microwave Mammography,” in *2010 IEEE International Symposium on Antennas and Propagation and CNC-USNC/URSI Radio Science Meeting* -, 2010, pp. 10–13.

[18] K. Suzuki, H. Hatano, and Y. Kuwahara, “Expansion of Microwave Imaging via Space-Time Beamforming to the Multi-Static Radar for Breast Cancer Detection,” *IEICE Trans. Electron. (Japanese Ed.)*, vol. J94–C, no. 10, pp. 306–315, 2011.

[19] H. S. Lui, A. Fhager, and M. Persson, “On the forward scattering of microwave breast imaging,” *Int. J. Biomed. Imaging*, vol. 2012, no. Article ID 582037, pp. 1–15, 2012.

[20] “Anatomy and physiology of the breast - Canadian Cancer Society.” [Online]. Available: http://www.cancer.ca/en/cancer-information/cancer-type/breast/anatomy-and-physiology/?region=qc. [Accessed: 12-May-2016].

[21] G. M. Cooper, *Elements of Human Cancer*. Jones & Bartlett Learning, 1992.

[22] “What Is Breast Cancer? | Breastcancer.org.” [Online]. Available: http://www.breastcancer.org/symptoms/understand_bc/what_is_bc. [Accessed: 12-May-2016].

[23] R. M. Rangayyan, N. M. El-Faramawy, J. E. Desautels, and O. a Alim, “Measures of Acutance and Shape for Classification of Breast Tumors,” *IEEE Trans Med Imaging*, vol. 16, no. 6, pp. 799–810, 1997.

[24] J. C.Lin, Ed., *Electromagnetic Fields in Biological Systems*. CRC Press, 2012.

[25] A. H. Barrett, P. C. Myers, and N. L. Sadowsky, “Microwave Thermography in the Detection of Breast Cancer,” *Am. J. Roentgenol.*, vol. 134, no. 2, pp. 365–368, 1980.

[26] C. Gabriel, S. Gabriel, and E. Corthout, “The dielectric properties of biological tissues: I. Literature survey,” *Phys. Med. Biol.*, vol. 41, pp. 2231–49, 1996.

[27] S. Gabriel, R. Lau, and C. Gabriel, “The dielectric properties of biological tissues : II. Measurements in the frequency range 10 Hz to 20 GHz,” *Phys. Med. Biol.*, vol. 41, pp. 2251–2269, 1996.

[28] M. Lazebnik, L. McCartney, D. Popovic, C. B. Watkins, M. J. Lindstrom, J. Harter, S.

Sewall, A. Magliocco, J. H. Booske, M. Okoniewski, and S. C. Hagness, “A large-scale study of the ultrawideband microwave dielectric properties of normal breast tissue obtained from reduction surgeries.,” *Phys. Med. Biol.*, vol. 52, pp. 2637–2656, 2007.

[29] S. Gabriel, R. W. Lau, and C. Gabriel, “The dielectric properties of biological tissues: III. Parametric models for the dielectric spectrum of tissues.,” *Phys. Med. Biol.*, vol. 41, pp. 2271–2293, 1996.

[30] M. Lazebnik, D. Popovic, L. McCartney, C. B. Watkins, M. J. Lindstrom, J. Harter, S. Sewall, T. Ogilvie, A. Magliocco, T. M Breslin, W. Temple, D. Mew, J. H. Booske, M. Okoniewski, and S. C. Hagness, “A large-scale study of the ultrawideband microwave dielectric properties of normal, benign and malignant breast tissues obtained from cancer surgeries,” *Phys. Med. Biol.*, vol. 52, no. 10, pp. 6093–6115, 2007.

[31] A. M. Campbell and D. V Land, “Dielectric properties of female human breast tissue measured in vitro at 3.2 GHz.,” *Phys. Med. Biol.*, vol. 37, no. 1, pp. 193–210, 1992.

[32] R. A. Smith, D. Saslow, K. Andrews Sawyer, W. Burke, M. E. Costanza, W. P. Evans, R. S. Foster, E. Hendrick, H. J. Eyre, and S. Sener, “American Cancer Society Guidelines for Breast Cancer Screening: Update 2003,” *CA Cancer J. Clin.*, vol. 53, no. 8, pp. 141–169, 2003.

[33] C. K. Kuhl, S. Schrading, C. C. Leutner, N. Morakkabati-Spitz, E. Wardelmann, R. Fimmers, W. Kuhn, and H. H. Schild, “Mammography, Breast Ultrasound, and Magnetic Resonance Imaging for Surveillance of Women at High Familial Risk for Breast Cancer,” *J. Clin. Oncol.*, vol. 23, no. 33, pp. 8469–8476, 2005.

[34] H. Zhang, “Microwave Imaging for Cancer Detection,” Edinburgh University, 2014.

[35] P. A. Carney, D. L. Miglioretti, B. C. Yankaskas, K. Kerlikowske, R. Rosenberg, C. M. Rutter, B. M. Geller, L. A. Abraham, S. H. Taplin, M. Dignan, G. Cutter, and R. Ballard-

Barbash, “Individual and Combined Effects of Age, Breast Density, and Hormone Replacement Therapy Use on the Accuracy of Screening Mammography,” *Ann. Intern. Med.*, vol. 138, no. 3, pp. 168–175, 2003.

[36] “Ultrasound,” *Breastcancer.org*. [Online]. Available: http://www.breastcancer.org/symptoms/testing/types/ultrasound. [Accessed: 13-May-2016].

[37] D. Saslow, C. Boetes, W. Burke, S. Harms, M. O. Leach, C. D. Lehman, E. Morris, E. Pisano, M. Schnall, S. Sener, R. A. Smith, E. Warner, M. Yaffe, K. S. Andrews, and C. A. Russell, “American Cancer Society Guidelines for Breast Screening with MRI as an Adjunct to Mammography,” *CA. Cancer J. Clin.*, vol. 57, no. 2, pp. 75–89, Mar. 2007.

[38] “Medical ultrasound.” [Online]. Available: https://en.wikipedia.org/wiki/Medical_ultrasound. [Accessed: 13-May-2016].

[39] M. Tozaki, I. Isomoto, Y. Kojima, K. Kubota, Y. Kuroki, K. Ohnuki, S. Ohsumi, and H. Mukai, “The Japanese Breast Cancer Society Clinical Practice Guidelines for Screening and Imaging Diagnosis of Breast Cancer,” *Breast Cancer (Japanese Breast Cancer Soc.*, pp. 1–10, 2015.

[40] V. Zhurbenko, T. Rubæk, V. Krozer, and P. Meincke, “Design and realisation of a microwave three-dimensional imaging system with application to breast-cancer detection,” *IET Microwaves, Antennas Propag.*, vol. 4, no. 12, pp. 2200–2211, 2010.

[41] V. Zhurbenko, “Challenges in the Design of Microwave Imaging Systems for Breast Cancer Detection,” *Adv. Electr. Comput. Eng.*, vol. 11, no. 1, pp. 91–96, 2011.

[42] A. Fhager, M. Gustafsson, and S. Nordebo, “Image reconstruction in microwave tomography using a dielectric debye model,” *IEEE Trans Biomed. Eng.*, vol. 59, no. 1, pp. 156–166, 2012.

[43] P. M. Meaney, K. D. Paulsen, and T. P. Ryan, “Microwave thermal imaging using a hybrid element method with a dual mesh scheme for reduced computation time,” in *Proceedings of the 15th Annual International Conference of the IEEE Engineering in Medicine and Biology Society*, 1993, pp. 96–97.

[44] Q. Fang, P. M. Meaney, S. D. Geimer, A. V. Streltsov, and K. D. Paulsen, “Microwave image reconstruction from 3-D fields coupled to 2-D parameter estimation,” *IEEE Trans. Med. Imaging*, vol. 23, no. 4, pp. 475–484, 2004.

[45] T. Rubæk, P. M. Meaney, P. Meincke, and K. D. Paulsen, “Nonlinear microwave imaging for breast-cancer screening using Gauss-Newton’s method and the CGLS inversion algorithm,” *IEEE Trans Antennas Propag.*, vol. 55, no. 8, pp. 2320–2331, 2007.

[46] Y. Xie, B. Guo, L. Xu, J. Li, and P. Stoica, “Novel Multistatic Adaptive Microwave Imaging Methods for Early Breast Cancer Detection,” *EURASIP J. Adv. Signal Process.*, vol. Article ID, no. 8, pp. 1–13, 2006.

[47] S. Caorsi, G. L. Gragnani, and M. Pastorino, “Two-dimensional microwave imaging by a numerical inverse scattering solution,” *IEEE Trans Microw. Theory Tech.*, vol. 38, no. 8, pp. 981–989, 1990.

[48] N. Bayat and P. Mojabi, “The Effect of Antenna Incident Field Distribution on Microwave Tomography Reconstruction,” *Prog. Electromagn. Res.*, vol. 145, pp. 153–161, 2014.

[49] P. M. Meaney, M. W. Fanning, D. Li, S. P. Poplack, and K. D. Paulsen, “A Clinical Prototype for Active Microwave Imaging of the Breast,” *IEEE Trans Microw. Theory Tech.*, vol. 48, no. 11, pp. 1841–1853, 2000.

[50] L. Mohamed, Y. Ono, T. Kamiya, and N. Ozawa, “乳癌検出のためのマイクロ波トモグラフィにおける多偏波の使用について‘Study of Multi-Polarization in Microwave

Tomography for Breast Cancer Detection,’” *電子情報通信学会論文誌 C*, vol. J99–C, no. 8, pp. 393–401, 2016.

[51] L. Mohamed, N. Ozawa, Y. Ono, T. Kamiya, and Y. Kuwahara, “Study of Correlation Coefficient for Breast Tumor Detection in Microwave Tomography,” *Open J. Antennas Propag.*, vol. 3, no. December, pp. 27–36, 2015.

[52] L. Mohamed and Y. Kuwahara, “Distortion Born Iterative Method in Microwave Tomography,” in *Thailand-Japan MicroWave (TJMW) 2014*, 2014, no. 5.

[53] R. E. Kleinman and P. M. van den Berg, “A modified gradient method for two-dimensional problems in tomography,” *J. Comput. Appl. Math.*, vol. 42, pp. 17–35, 1992.

[54] A. Franchois and C. Pichot, “Microwave Imaging-Complex Permittivity Reconstruction with a Levenberg-Marquardt Method,” *IEEE Trans Antennas Propag.*, vol. 45, no. 2, pp. 203–215, 1997.

[55] D. W. Oldenburg, “Practical strategies for the solution of large-scale electromagnetic inverse problems,” *Radio Sci.*, vol. 29, no. 4, pp. 1081–1099, 1994.

[56] W. C. Chew and Y. M. Wang, “Reconstruction of Two-Dimensional Permittivity Distribution Using the Distorted Born Iterative Method,” *IEEE Trans Med Imaging*, vol. 9, no. 2, pp. 218–225, 1990.

[57] C. Pichot, G. Peronnet, J. C. Bolomey, and L. Jofre, “Active Microwave Imaging of Inhomogeneous Bodies,” *IEEE Trans Antennas Propag.*, vol. AP-33, no. 4, pp. 416–425, 1985.

[58] N. Joachimowicz, C. Pichot, and J.-P. Hugonin, “Inverse Scattering: An Iterative Numerical Method for Electromagnetic Imaging,” *IEEE Trans Antennas Propag.*, vol. 39, no. 12, pp. 1742–1752, 1991.

[59] T. Gunnarsson, “Microwave Imaging of Biological Tissues : Applied Toward Breast

Tumor Detection," Malardalen University, Sweden, 2007.

[60] Q. Fang, "Computational Methods for Microwave Medical Imaging," Dartmouth College, New Hampshire, 2004.

[61] A. Roger, "Newton-Kantorovitch Algorithm Applied to an Electromagnetic Inverse Problem," *IEEE Trans Antennas Propag.*, vol. AP-29, no. 2, pp. 232–238, 1981.

[62] J. D. Shea, P. Kosmas, B. D. Van Veen, and S. C. Hagness, "Contrast-enhanced microwave imaging of breast tumors: a computational study using 3D realistic numerical phantoms," *Inverse Probl.*, vol. 26, no. 074009, pp. 1–22, 2010.

[63] J. D. Shea, P. Kosmas, S. C. Hagness, and B. D. Van Veen, "Three-dimensional microwave imaging of realistic numerical breast phantoms via a multiple-frequency inverse scattering technique.," *Med. Phys.*, vol. 37, no. 8, pp. 4210–4226, 2010.

[64] D. W. Winters, B. D. Van Veen, and S. C. Hagness, "A Sparsity Regularization Approach to the Electromagnetic Inverse Scattering Problem," *IEEE Trans Antennas Propag.*, vol. 58, no. 1, pp. 145–154, 2010.

[65] R. F. Remis and P. M. van den Berg, "On the equivalence of the Newton – Kantorovich and distorted Born methods," *Inverse Probl.*, vol. 16, pp. 1–4, 2000.

[66] "Well-posed Problems." [Online]. Available: https://en.wikipedia.org/wiki/Well-posed_problem.

[67] S. Cohn, "Lecture Notes on Well-posed." [Online]. Available: https://www.math.unl.edu/~scohn1/8423/wellposed.pdf. [Accessed: 18-May-2016].

[68] P. C. Hansen and D. P. O'Leary, "The Use of the L-Curve in the Regularization of Discrete Ill-Posed Problems," *SIAM J. Sci. Comput.*, vol. 14, no. 6, pp. 1487–1503, 1993.

[69] P. C. Hansen, "Regularization Tools -- A Matlab Package for Analysis and Solution of Descrete Ill-Posed Problems," 2008.

[70] D. W. Winters, E. J. Bond, B. D. Van Veen, and S. C. Hagness, “Estimation of the Frequency-Dependent Average Dielectric Properties of Breast Tissue Using a Time-Domain Inverse Scattering Technique,” *IEEE Trans. Antennas Propag.*, vol. 54, no. 11, pp. 3517–3528, 2006.

[71] D. G. Drogoudis, G. A. Kyriacou, and J. N. Sahalos, “A Sensitivity Matrix Based Microwave Tomography Exploiting an Adjoint Network Theorem,” *IEEE Trans Magn.*, vol. 45, no. 3, pp. 1686–1689, 2009.

[72] C. Liu, L. Xu, Z. Cao, and Z. Qian, “Simulation on Measuring of Nonuniform Temperature Distribution Based on Line-of-sight TDLAS by Using Tikhonov Regularization Method,” *2012 8th IEEE Int. Symp. Instrum. Control Technol. ISICT 2012 - Proc.*, pp. 92–95, 2012.

[73] M. Ostadrahimi and A. Zakaria, “A Near-Field Dual Polarized(TE-TM) Microwave Imaging System,” *IEEE Trans Microw. Theory Tech.*, vol. 61, no. 3, pp. 1376–1384, 2013.

[74] Q. Fang, P. M. Meaney, and K. D. Paulsen, “Microwave Image Reconstruction of Tissue Property Dispersion Characteristics Utilizing Multiple-Frequency Information,” *IEEE Trans. Microw. Theory Tech.*, vol. 52, no. 8, pp. 1866–1875, 2004.

[75] M. Asefi, M. OstadRahimi, A. Zakaria, and J. LoVetri, “A 3-D Dual-Polarized Near-Field Microwave Imaging System,” *IEEE Trans. Microw. Theory Tech.*, vol. 62, no. 8, pp. 1790–1797, 2014.

[76] A. Abubakar, T. M. Habashy, and G. Pan, “Microwave Data Inversions Using the Source-Receiver Compression Scheme,” *IEEE Trans. Antennas Propag.*, vol. 60, no. 6, pp. 2853–2864, 2012.

[77] A. Fhager, P. Hashemzadeh, and M. Persson, “Reconstruction Quality and Spectral

Content of an Electromagnetic Time-Domain Inversion Algorithm," *IEEE Trans. Biomed. Eng.*, vol. 53, no. 8, pp. 1594–1604, 2006.

[78] R. Owen Mays, N. Behdad, and S. C. Hagness, "A TSVD Analysis of the Impact of Polarization on Microwave Breast Imaging Using an Enclosed Array of Miniaturized Patch Antennas," *IEEE Antennas Wirel. Propag. Lett.*, vol. 14, pp. 418–421, 2015.

[79] M. J. Burfeindt, N. Behdad, B. D. Van Veen, and S. C. Hagness, "Quantitative microwave imaging of realistic numerical breast phantoms using an enclosed array of multiband, miniaturized patch antennas," *IEEE Antennas Wirel. Propag. Lett.*, vol. 11, pp. 1626–1629, 2012.

[80] T. M. Grzegorczyk, P. M. Meaney, P. A. Kaufman, R. M. di Florio-Alexander, and K. D. Paulsen, "Fast 3-D Tomographic Microwave Imaging for Breast Cancer Detection," *IEEE Trans Med Imaging*, vol. 31, no. 8, pp. 1584–1592, 2012.

[81] J. D. Shea, B. D. Van Veen, and S. C. Hagness, "A TSVD analysis of microwave inverse scattering for breast imaging," *IEEE Trans. Biomed. Eng.*, vol. 59, no. 4, pp. 936–945, 2012.

[82] N. Ozawa, "マイクロ波トモグラフィによる 乳房内組織イメージング(M2)," Shizuoka University, 2016.

[83] L. Mohamed and Y. Kuwahara, "Microwave Tomography Using DBIM with Double Mesh Scheme," in *ISAP*, 2015.

[84] H. A. van der Vorst, "BI-CGSTAB: A FAST AND SMOOTHLY CONVERGING VARIANT OF BI-CG FOR THE SOLUTION OF NONSYMMETRIC LINEAR SYSTEMS*," *SIAM J. Sci. Stat. Comput.*, vol. 13, no. 2, pp. 631–644, 1992.

[85] M. O'Halloran, R. Conceicao, D. Byrne, M. Glavin, and E. Jones, "FDTD MODELING OF THE BREAST: A REVIEW," *Prog. Electromagn. Res. B*, vol. 18, pp. 1–24, 2009.

[86] T. J. Colgan, S. C. Hagness, and B. D. Van Veen, “A 3-D level set method for microwave breast imaging,” *IEEE Trans. Biomed. Eng.*, vol. 62, no. 10, pp. 2526–2534, 2015.

[87] “Least-Squares Fitting - MATLAB & Simulink - MathWorks 日本.” [Online]. Available: http://jp.mathworks.com/help/curvefit/least-squares-fitting.html. [Accessed: 12-Aug-2016].

[88] E.-K. Ikram, S. Khatun, J. R. Khondker, M. M. Rahman, and M. M. Fakir, “Improved debye model for experimental approximation of human breast tissue properties at 6 GHz ultra-wideband centre frequency,” *Int. J. Eng. Technol.*, vol. 5, no. 6, pp. 4708–4717, 2013.

LIST OF PUBLICATION & AWARDS

Journal

[1] L. Mohamed, N. Ozawa, Y.Ono, T. Kamiya, Y. Kuwahara, “Study of Correlation Coefficient for Breast Tumor Detection in Microwave Tomography”, Open Journal of Antennas and Propagation (OJAPr), Scientific Research, Vol.3 No.4, Dec 2015.

[2] ラティファモハメド, 小野佑樹, 神谷俊宏, 小澤尚之, 桑原義彦, “乳癌検出のためのマイクロ波トモグラフィにおける多偏波の使用について”, IEICE Transactions on Electronics (Vol. J99-C, No.8, 2016).

Proceedings/Technical Report

[1] Latifah Mohamed, Yoshihiko Kuwahara, "Consideration of a Modified Gradient Method in Microwave Tomography”, IEICE Technical Report (AP), 6 Feb 2014, Toyota, Japan.

[2] Latifah Mohamed, Yoshihiko Kuwahara, "Polarization Diversity in Microwave Tomography", International Workshop on Antenna Technology (iWAT 2014), 4 - 6 Mac 2014, Sydney Australia.

[3] 小澤尚之・モハメド ラティファ・桑原義彦, “多偏波を使用するマイクロ波トモグラフィ”, Proceedings of the 2014 IEICE General Conference, C-2-107, ISSN 1349-1377, 18 – 21 March 2014, Niigata University, Niigata.

[4] Latifah Mohamed, Yoshihiko Kuwahara, “Distortion Born Iterative Method in Microwave Tomography – A Numerical Study of 3D Non-Debye and Debye Model –” 2014 Thailand- Japan MicroWave (TJMW2014), 26-28 November 2014, KMITL Bangkok, Thailand.

[5] Latifah Mohamed, Yoshihiko Kuwahara, "A Numerical Study on Different Polarizations in Microwave Tomography ", Proceedings of the 2015 IEICE General Conference C-2-104, ISSN 1349-1377, 10 – 13 March 2015, Ritsumeikan University (Biwako Kusatsu Campus), Japan.

[6] Latifah Mohamed, Yoshihiko Kuwahara, "Microwave Tomography Using DBIM with Double Mesh Scheme", International Symposium on Antennas and Propagation (ISAP2015), 9 – 12 Nov 2015, Wrest Point Hobart Tasmania Australia.

[7] Y. Ono, T. Kamiya, L. Mohamed, and Y. Kuwahara, "Study of Correlation Coefficients of the Receiver Pair in Microwave Tomography", International Symposium on Antennas and Propagation (ISAP2016), Okinawa Convention Center, Ginowan, Okinawa, Japan (accepted, in progress).

[8] Yuuki Ono, Latifah Mohamed, Yoshihiko Kuwahara, "マイクロ波トモグラフィ用のイメージングセンサの構成の最適化 -Optimization of Configuration on Imaging Sensor for Microwave Tomography-", Proceedings of the 2016 IEICE Society Conference, 20 – 23 September 2016, Hokkaido University, Hokkaido, Japan (accepted, in progress).

Award

"Young Researcher Encouragement Award" in 2014 Thailand- Japan MicroWave (TJMW2014), 26-28 November 2014, KMITL Bangkok, Thailand.